Fachartikel 2005

Prof. Dr. Dr. h.c.* Herbert Eichele (Hrsg.)
* Staatsuniversität Tomsk Russland (TUSUR)

Georg-Simon-Ohm-Fachhochschule Nürnberg
Keßlerplatz 12
90489 Nürnberg

Inhaltsverzeichnis   Seite

Hochoktan Ottokraftstoffe für Hochleistungsmotoren

Prof.Dr.-Ing. M. Weclas

Prof.Dr.-Ing. H-J. Tretow

Dipl.-Ing. (FH) J. Bernstein

Dipl.-Ing. (FH) J. Wellmann

Institut für Fahrzeugtechnik der Georg-Simon-Ohm Fachhochschule Nürnberg

Keßlerplatz 12
90489 Nürnberg

Abstract

Seit mehreren Monaten gibt es an Tankstellen in Deutschland neue Sorten Ottokraftstoffe zu kaufen, Shell (V-Power) und Aral (Ultimate 100), jeweils 100 Oktan. Laut Herstellerangabe verhilft dieser Kraftstoff zu mehr Leistung bei gleichzeitig geringerem Verbrauch und verbessertem Beschleunigungsvermögen.

Ziel des hier beschriebenen Projekts war es, durch vergleichende Messungen belastbare Aussagen über Leistung, Beschleunigung und Verbrauch der neuen Kraftstoffe machen zu können.

Es wurde festgestellt, dass keiner der beiden Hochoktankraftstoffe relevante Mehrleistung, Drehmomentzuwachs, Verbrauchsersparnis oder Performancegewinn bringt. Die festgestellten Differenzen liegen unter 2%, d.h. an der Messgenauigkeitsgrenze. Hinsichtlich der Leistung war der Referenzkraftstoff (herkömmliches Super Plus von Esso, 98 Oktan) dem Kraftstoff V-Power mit 100 Oktan sogar leicht überlegen. Im unteren Teillastbereich lässt sich bei den Hochoktankraftstoffen eine minimale Verbrauchsersparnis feststellen.

1. Einleitung

Ottokraftstoffe müssen vielfältige Anforderungen erfüllen, um für einen Einsatz in Motoren mit Fremdzündung geeignet zu sein. Sie bestehen aus einer Vielzahl von Kohlenwasserstoffen, deren Siedeverlauf wichtig für den einwandfreien Betrieb der Fahrzeuge ist. Die hochsiedenden Bestandteile enthalten viel Energie und wirken sich günstig auf den Verbrauch aus. Der Dampfdruck beschreibt die Verdampfungsneigung eines Kraftstoffs. Witterungsbedingt müssen Ottokraftstoffe im Winter für einen sicheren Kaltstart einen höheren Dampfdruck besitzen als im Sommer.

Ottokraftstoffe müssen klopffest, d. h. gegen Selbstentzündung widerstandsfähig, sein. Das Maß für die Klopffestigkeit ist die Oktanzahl, die im Allgemeinen nach der so genannten Research-Methode (ROZ) bestimmt wird. Die an Tankstellen angebotenen Benzinsorten unterscheiden sich in ihrer Klopffestigkeit: Normalbenzin mit 91 ROZ, Euro-Super 95 ROZ, Super Plus 98 ROZ und aktuell auch mit 100 ROZ. Die besonders klopffesten Kraftstoffe Super Plus und 100 ROZ wurden für Hochleistungsmotoren mit hoher Verdichtung entwickelt. Höhere Klopffestigkeit lässt eine bessere Ausnutzung des Energiegehaltes eines Kraftstoffs zu.

Die Verwendung eines hochoktanigen Kraftstoffs ermöglicht es, die Zündzeiten zu optimieren und hierdurch eine deutliche Wirkungsgradsteigerung zu erreichen. Die Abhängigkeit zwischen Oktanzahl und Lage der Klopfgrenze ist im Bereich handelsüblicher Ottokraftstoffe annähernd linear [1].

Die Motorleistung ist von mehreren Faktoren abhängig:

$$(1) \qquad P_e = \eta_e \cdot \frac{p_L}{R_L \cdot T_L} \cdot V_H \cdot \frac{n}{2} \cdot \frac{H_u}{L_{st}} \cdot \frac{1}{\lambda}$$

η_e ist der effektive Wirkungsgrad des realen Motors, p_L, R_L, T_L sind Luftdruck, Gaskonstante und Lufttemperatur an der Ansaugseite des Motors, V_H ist der Hubraum des Motors, n ist die Drehzahl, H_u ist der Heizwert des Kraftstoffs, L_{st} ist das stöchiometrische Luftverhältnis, und λ ist die Luftzahl des Gemisches in den Zylindern. Die Kraftstoffqualität kann durch mehrere Parameter die Motorleistung beeinflussen, insbesondere durch die Optimierung von indiziertem und mechanischem Wirkungsgrad (z.B. reduzierte Reibung), und durch den Heizwert des Kraftstoffs (z.B. Normalbenzin H_u=42.7MJ/kg$_K$, Superbenzin H_u=43.5MJ/kg$_K$, bzw. ist H_u/L_{st} für Normalbenzin 2.88MJ/kg$_L$ und für Superbenzin H_u/L_{st}=2.95MJ/kg$_L$).

Seit mehreren Monaten gibt es an den Tankstellen in Deutschland neue Sorten Ottokraftstoff zu kaufen. Die Kraftstoffe, angeboten von Shell (V-Power) und Aral (Ultimate100), haben jeweils 100 Oktan. Herstellerangaben versprechen mit diesen Kraftstoffen mehr Leistung bei gleichzeitig weniger Verbrauch und verbessertem Beschleunigungsvermögen.

In der Presse wird das Thema intensiv diskutiert. Der ADAC oder die Zeitschrift „Autobild" haben Versuchsreihen durchgeführt, aus deren Ergebnissen sich jedoch nicht erkennen lässt, inwieweit die Testbedingungen die Ergebnisse beeinflusst haben. Am Institut für Fahrzeugtechnik der Fachhochschule Nürnberg wurde wegen dieser ungenauen Aussagen Versuchsreihen gefahren, um unter genau definierten Testbedingungen vergleichbare Ergebnisse zu erhalten und daraus Aussagen über Leistung, Beschleunigung und Verbrauch der neuen Kraftstoffe zu gewinnen. Die Ergebnisse der ersten Phase des Projektes sind in diesem Aufsatz zusammengefasst.

Zum Vergleich verschiedener Kraftstoffe wurden die beiden populärsten Premium-Otto-Kraftstoffe auf dem Markt herangezogen: „**Shell V-Power**" und „**Aral Ultimate 100**", beides Ottokraftstoffe mit 100 Oktan, die ca. 8 Eurocent teurer als vergleichbarer Super-Plus Kraftstoff sind. Als Referenzkraftstoff diente ein herkömmlicher Super Plus Kraftstoff mit 98 Oktan. Es handelte sich durchgängig um Winterkraftstoff, da der gesamte verwendete Kraftstoff im Januar/Februar bezogen wurde.

In Kapitel 2 sind der Rollenprüfstand und das Testfahrzeug beschrieben, Kapitel 3 erläutert die Methodologie und die Testbedingungen. Insbesondere werden hier die Reproduzierbarkeit der Messergebnisse auf dem Rollenprüfstand diskutiert sowie der Kraftstoffwechsel und die Problematik der Kraftstoffvermischung beschrieben. Die Messergebnisse werden in Kapitel 4 dargestellt und diskutiert.

2. Rollenprüfstand und Testfahrzeug

2.1. Rollenprüfstand

Der Funktions- und Leistungsprüfstand LPS (FH Nürnberg) der Firma MAHA Maschinenbau, Haldenwang besteht aus einer Steuerungseinheit und zwei Rollensätzen. Zur Einstellung auf unterschiedliche Achsabstände dient eine Rollensatzverstellung. Umfangreiche Kühlluftgebläse simulieren den Fahrtwind. Der Rollensatz ist mit einer Hebeschwelle, einer elektrischen Wirbelstrombremse und Abdeckplatten ausgestattet.

Der Antriebsstrang besteht aus einer geregelten Gleichstrommaschine und zwei luftgekühlten Wirbelstrombremsen. Zusätzliche Schwungmassen am

vorderen Rollensatz ermöglichen es, unterschiedliche rotierende Fahrzeugmassen zu simulieren (siehe Abb.1).

Abb.1. Rollenprüfstand

Mit dem Funktions- und Leistungsprüfstand LPS ist es möglich, Fahrzeuge mit Otto- und Dieselmotor mit einer Prüfgeschwindigkeit von bis zu 200 km/h (variabel) und einer Gesamtradleistung von 400 kW zu prüfen. Eine Leistungsmessung bei konstanter Drehzahl, Geschwindigkeit oder Zugkraft wird durch automatische Drehzahl-, Geschwindigkeits- oder Zugkraftregelung ermöglicht. Neben der Motorleistungsmessung können weitere Funktionsprüfungen durchgeführt werden. In Verbindung mit einem Benzin-Verbrauchsmessgerät kann der Verbrauch des Fahrzeugs ermittelt werden. Ein Stoppuhrprogramm dient zur Beschleunigungsmessung zwischen zwei frei wählbaren Geschwindigkeiten. Zur Korrektur von Leistungsdaten nach DIN oder ECE sind ein Barometer und ein Thermometer in der Schnittstellenbox eingebaut. Der Leistungsprüfstand erlaubt die Überprüfung des Tachometers bzw. Kilometerzählers. Alle Messergebnisse werden graphisch dargestellt und ausgedruckt. Technische Daten des Rollenprüfstandes sind in der Tabelle 1 zusammengefasst.

Das Kraftstoffverbrauchsmesssystem setzt sich zusammen aus der Rechnungseinheit 206 mit Printer (Microprozessor mit 8 Programmen und automatisch gesteuertem Drucker), dem Messgeber 206 (4-Kolben Volumenzähler mit Hallgeber und Drehsinnerkennung, hohe Messgenauigkeit) und der Messeinheit 4705. Die Messeinheit und der Messgeber sind zusammengebaut und im Fahrzeug auf dem Beifahrersitz platziert.

Das Flowjet-Ventil 4703 besitzt eine eigene Kraftstoffpumpe sowie einen Wärmetauscher. Der Messgeber hat einen maximalen Abweichungsbereich von ± 0,5 % bezogen auf den momentanen

Messwert. Der fahrzeugeigene Benzinkreislauf ist in zwei Kreisläufe aufgeteilt.

Tab. 1. Technische Daten des Rollenprüfstandes

Rollensatzmechanik	
Achslast	2.5 t
Rollenbreite pro Rolle	650 mm
Spur min.	520 mm
Spur max.	2120 mm
Rollendurchmesser	502 mm
möglicher Radstand	2000 mm - 3000 mm
Hebeschwelle	min. 5 bar
Elektrische Daten	
Wirbelstrombremse	2 x 200 kW
Messsystem	elektronisches DMS - Messsystem
Netzanschluss	400 V / 50 Hz
Absicherung	32 A
Anzeigebereiche	
Prüfgeschwindigkeit	200 km/h
Radleistung	max. 200 kW pro Achse
Messgenauigkeit	Radleistungsendwert ± 2% vom Messwert

Der primäre Kreislauf verbindet den Kraftstofftank mit dem Flowjet-Ventil, der sekundäre Kreislauf verbindet das Ventil mit dem Motor. Die Labor- und Prüfstandsbelüftung wird durch verschiedene Gebläse gewährleistet und verbessert. Diese sind im Detail in Abb.2 dargestellt.

2.2. Versuchsfahrzeug

Als Testfahrzeug wurde ein Audi S4 Avant 4.2 quattro mit Hochleistungs-Benzin-V8-MPI Saugmotor mit serienmäßiger Motorsteuerung und Ventiltrieb gewählt (Abb. 3).

Abb.3. V8-4.2 Liter Benzinmotor des Testfahrzeugs (Audi S4)

Walzenlüfter zur Simulation des Fahrtwindes
Stufenlos regelbar Die maximale Stufe entspricht
dem Fahrtwind bei v = 120 km/h

Abgasabsaugung mit 3900 m³/h
Absaugung der Warmluft vom Unterboden

Absaugung der Warmluft der Wirbelstrombremsen

Zusätzliches Kühlluftgebläse zur
Anströmung des Ölkühlers

Zusätzliches Gebläse zur verbesserten
Wärmeabführung
des Abgasstrangs im Unterbodenbereich

Abb.2. Verschiedene Komponente des Belüftungs- und Kühlungssystems

Die wichtigsten technischen Daten des Testfahrzeugs gemäß Angaben der Fa. Audi sind in der Tabelle 2 zusammengefasst. Alle Fahrzeugkomponenten sind Originalserienteile, an Motor, Abgasanlage und Triebstrang wurden keine Änderungen vorgenommen (Abb.4).

Audi S4 Avant 4.2 (Auslieferung des Versuchsfahrzeugs: 07/1993)	206 kW (280 PS) mit Abgasreinigung nach 91/441/EWG
Motor und Getriebe	
Motor-Bauart	8-Zylinder-V-Ottomotor, längs eingebaut
Bohrung x Hub, mm	84,5 x 93
Hubraum, Liter/cm³	4,2/4172
Max. Leistung, kW bei 1/min nach 80/1269/EWG	206/5800
Max. Drehmoment, Nm bei 1/min nach 80/1269/EWG	400/4000
Verdichtung	10,6
Gemischaufbereitung	Vollelektronische Motorsteuerung (Motronic) mit selektiver Klopfregelung
Abgasreinigung	2 Katalysatoren und Lambda-Regelung
Getriebe	6-Gang-Schaltgetriebe
Batterie	12 V, 88 Ah
Abmessungen	
Länge/Breite/Höhe (bei Leergewicht), mm	4790/1777/1472
Stirnfläche, mm²	2,14
Luftwiderstandsbeiwert	0,35
Radstand bei Leergewicht, mm	2692
Spurweite vorn/hinten, mm	1569/1534
Kraftstoffbehälter, Liter	80
Rädergröße/Reifen/Reifengröße	8J x 17/Dunlop SP Sport 8000/ 245/40 ZR 17
Gewichte (Werksangabe)	
Leergewicht, kg	1730
Gewichte (eigene Messung)	
Leergewicht (bei vollem Tank), kg	1762
Gewicht mit Fahrer, kg	1846
Fahrleistungen	
Höchstgeschwindigkeit, km/h	247
Beschleunigung 0-100 km/h, s	6,6
Kraftstoffverbrauch nach 80/1269/EWG Liter/100 km	Super Plus, bleifrei mind. 98 ROZ
bei 90 km/h	9,3
bei 120 km/h	11,3
im Stadtzyklus	18,9
Kraftübertragung	permanenter Allradantrieb mit zentralem Torsendifferential
Übersetzung	I. 3,500, II. 1,889, III. 1,231, IV. 0,967, V. 0,806, VI. 0,685, R. 3,455
Achsantrieb	4,111:1

Tab.2. Technische Daten des Testfahrzeugs

Das Fahrzeug wurde für die Messung auf dem Prüfstand mit einem Kraftstoffverbrauchsmessgerät

ausgerüstet. Aufgrund der hohen thermischen Belastung bei Messungen im Volllastbereich wurden zusätzliche Maßnahmen getroffen, um die Kraftstofftemperatur konstant zu halten.

Abb.4. Serienabgasanlage

Zum einen wurde das Fahrzeug mit einem Kraftstoffkühlsystem ausgestattet. In den Rücklauf des Kraftstoffsystems wurde ein Plattenkühler eingebaut. Dieser kühlte den Kraftstoff mit Leitungswasser, so dass die Temperatur des Kraftstoffes während der Messungen nahezu konstant blieb (Abb.5).

Abb.5. Plattenwärmetauscher des Kraftstoffkühlers

Zum anderen wurde zur verbesserten Wärmeabfuhr die Motorhaube des Fahrzeuges entfernt. Die im Testfahrzeug eingebauten Messeinrichtungen sind in Abb. 6 dargestellt.

2.3. Kraftstoffe

Für dieses Projekt wurden drei Kraftstoffe zum Test ausgewählt. Es sind handelsübliche Ottokraftstoffe, die alle an deutschen Tankstellen verfügbar sind.

Die an Tankstellen angebotenen Benzinsorten unterscheiden sich in ihrer Klopffestigkeit. Normalbenzin hat 91 ROZ, Euro-Super 95 ROZ, Super Plus 98 ROZ und aktuell auch 100 ROZ. Die besonders klopffeste Kraftstoffsorte Super Plus und 100 ROZ wurde für Motoren mit hoher Verdichtung entwickelt, die ursprünglich auf hochoktaniges Benzin angewiesen waren. Höhere Klopffestigkeit lässt eine bessere Ausnutzung des Energiegehaltes eines Kraftstoffs zu.
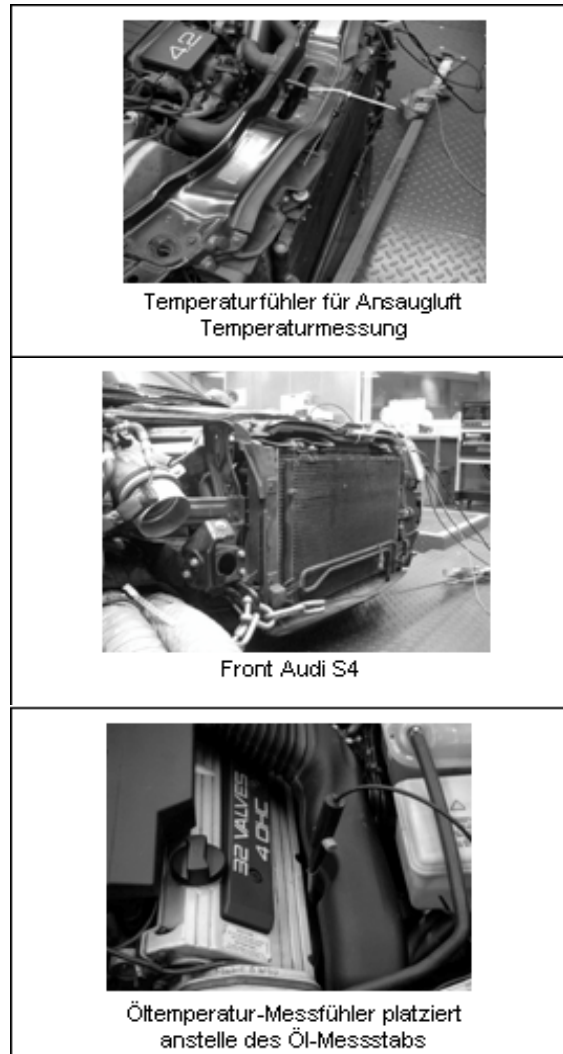
Temperaturfühler für Ansaugluft Temperaturmessung

Front Audi S4

Öltemperatur-Messfühler platziert anstelle des Öl-Messstabs

Abb.6. Messstellen am Motor

Additive für Ottokraftstoffe: Ablagerungen auf Ventilen, Einspritzdüsen und im Ansaugsystem wirken bei Kaltstart wie ein Schwamm und verändern so das Kraftstoff-Luft-Gemisch. Stark verschmutzte Ventile führen außerdem zu Leistungsminderung und erhöhtem Verbrauch. Für die Kraftstoffqualität ist daher neben der ausgewogenen Mischung der verschiedenen Komponenten die Verwendung hochwertiger Kraftstoffzusätze von zunehmender Bedeutung.

Folgende Kraftstoffe wurden für die Durchführung der verschiedenen Messreihen verwendet:

- BP für die Reproduzierbarkeit der Messungen (98 ROZ)
- Aral Ultimate 100 (100 ROZ)
- Shell V-Power (100 ROZ)
- Esso Super Plus als Referenzkraftstoff (98 ROZ).

3. Methodologie und Versuchsbedingungen

Die Messungen wurden in fünf Phasen durchgeführt:

1. Prüfung der Reproduzierbarkeit der Messungen
2. Leistung-Drehmoment bei Volllast für alle drei getesteten Kraftstoffe
3. Elastizitätsmessungen für alle drei getesteten Kraftstoffe
4. Kraftstoffverbrauchmessungen bei unterschiedlichen Lasten für alle drei getesteten Kraftstoffe.
5. Wiederholung der Reproduzierbarkeit der Messungen

3.1. Reproduzierbarkeit der Messungen

Dieser Teil des Messprogramms beinhaltet neben der Leistungsmessung auch Elastizitäts- und Verbrauchsmessungen mit BP 98 ROZ Kraftstoff. Ziel dieser Messungen war es, die Toleranzgrenzen des Prüfstandes zu ermitteln. Die Ergebnisse zeigten, dass die Reproduzierbarkeit der Messungen sehr hoch ist, sie liegt bei 98%. Zur Leistungsmessung steht die Möglichkeit der kontinuierlichen und der diskreten Leistungsmessung zur Verfügung. Die kontinuierliche Leistungsmessung hat keine abgelegten Einzelwerte und bietet zur Nachvollziehbarkeit lediglich einen Prüfausdruck, der nicht elektronisch speicherbar ist.

Daher bietet sich die diskrete Leistungsmessung an. Durch feine Abstufungen der Einzelwerte war hier hohe Genauigkeit zu gewährleisten. Der Vergleich zwischen den zwei Messverfahren zeigt eine sehr gute Übereinstimmung hinsichtlich der ausgegebenen Maximalwerte (Abb.7).
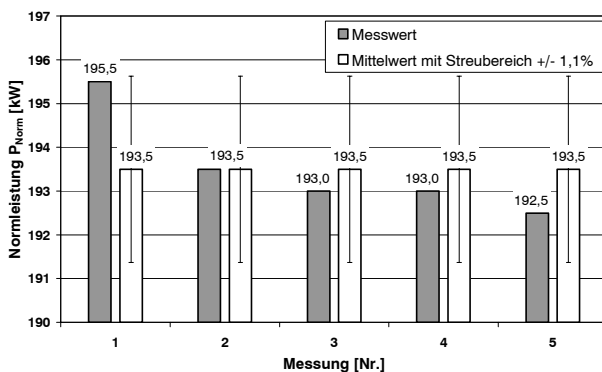
Abb.7. Leistung: Reproduzierbarkeit der Messungen (Kraftstoff: BP 98 ROZ)

Die Ergebnisse für Reproduzierbarkeit der Elastizitätsmessungen sind in Abb. 8 zusammengefasst. Durch eine arithmetische Mittelung von 10 Messwerten ist die Abweichung sehr gering und liegt unter 2.5%.
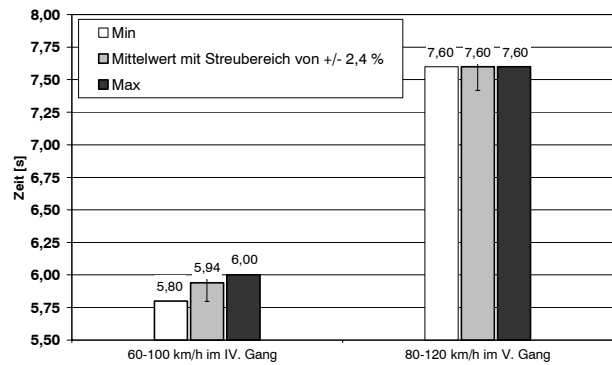
Abb.8. Elastizität: Reproduzierbarkeit der Messungen (Kraftstoff: BP 98 ROZ)

Diese sehr hohe Reproduzierbarkeit der Messungen ist auch bei Verbrauchsmessungen bestätigt worden (Abb. 9 bis12). Hier liegt die relative Abweichung liegt zwischen 0.6% und maximal 1.6%.

Testbedingungen für die Einzelleistungspunkte waren:

- 15% Leistung: 1500N Zugkraft bei 2200 U/min
- 30% Leistung: 2000N Zugkraft bei 3250 U/min
- 60% Leistung: 2750N Zugkraft bei 4500 U/min
- 100% Leistung: 3250 N Zugkraft max. erreichte Drehzahl.
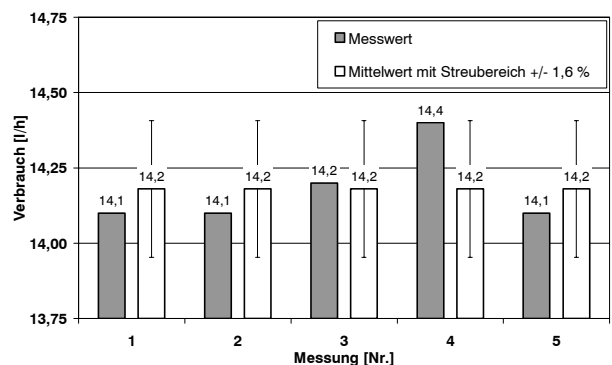
Abb.9. Kraftstoffverbrauch bei 15% Last: Reproduzierbarkeit der Messungen (Kraftstoff: BP 98 ROZ)
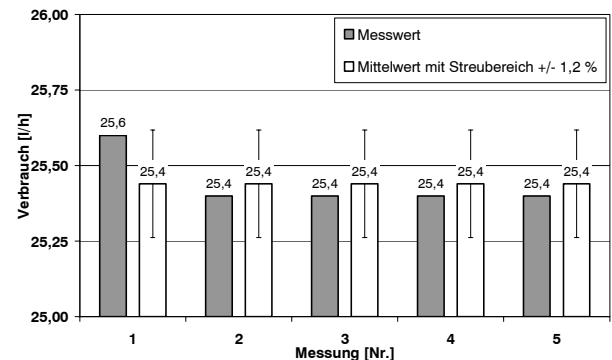
Abb.10. Kraftstoffverbrauch bei 30% Last: Reproduzierbarkeit der Messungen (Kraftstoff: BP 98 ROZ)
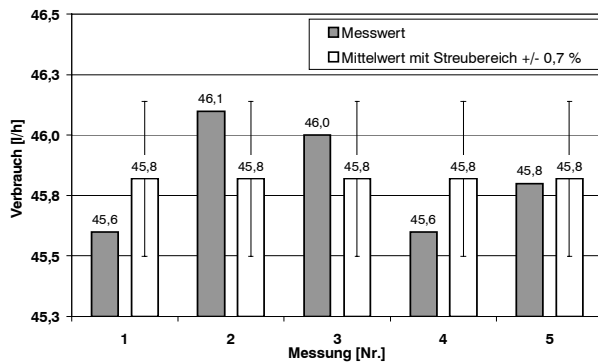
Abb.11. Kraftstoffverbrauch bei 60% Last: Reproduzierbarkeit der Messungen (Kraftstoff: BP 98 ROZ)
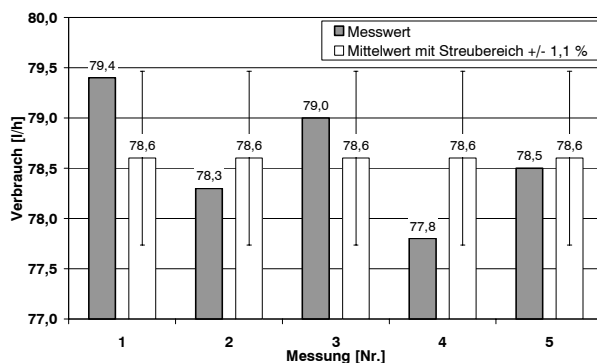
Abb.12. Kraftstoffverbrauch bei 100% Last: Reproduzierbarkeit der Messungen (Kraftstoff: BP 98 ROZ)

3.2. Kraftstoffwechsel und die Problematik Kraftstoffvermischung

Die drei ausgewählten Ottokraftstoffe (Esso Super Plus 98 ROZ; Shell V-Power 100 ROZ; Aral Ultimate 100 ROZ) sind von unabhängigen Tankstellen gekauft worden. Es wurden beschriftete Kraftstoffkanister aus dem Fachhandel (geprüft nach UN-Norm) verwendet, welche vorgereinigt waren. Als Tankgefäß wurde der bordeigene Fahrzeugtank in Originalzustand und Originalunterbringung genutzt. Auf einen externen Tank wurde aus Gründen der Authentizität im realen Fahrbetrieb verzichtet, obwohl die Kraftstoffwechsel mit weniger Aufwand hätten durchgeführt werden können. Um dem Problem der Vermischung verschiedener Kraftstoffe im Kraftstoffkreislauf des Fahrzeuges entgegenzutreten wurde eine Prozedur zur Spülung festgelegt. Die Spülung wird jeweils bei der Umstellung auf einen anderen Kraftstoff angewendet. Diese stellt sich in 8 Schritten dar:

1. Tankbehälter unter zu Hilfenahme der fahrzeugeigenen Kraftstoffpumpe entleeren

2. Eine definierte Menge von 10 Litern Referenzkraftstoff (Esso Super Plus) in den Tank einfüllen

3. 8 Liter (nach Benzin-Verbrauchsanzeige) im Betriebspunkt mit 30 % der maximalen Leistung (2000 N Last bei 3250 U/min) verfahren

4. Tankbehälter unter zu Hilfenahme der fahrzeugeigenen Kraftstoffpumpe entleeren

5. Einfüllen von 10 l des zu messenden Kraftstoffes

6. 8 Liter (nach Benzin-Verbrauchsanzeige) im Betriebspunkt mit 30 % der maximalen Leistung (2000 N Last bei 3250 U/min) verfahren

7. Tankbehälter unter zu Hilfenahme der fahrzeugeigenen Kraftstoffpumpe entleeren

8. Tank mit 60 Litern des zu messenden Kraftstoffes befüllen

3.3. Messparameter und charakteristische Größen

Verglichen werden sollten vorrangig die Leistungssteigerung, die Elastizität und der Kraftstoffverbrauch. Entscheidend war außerdem, dass alle Einflüsse vergleichbar berücksichtigt und kontrolliert werden. Darunter fallen Luftdruck der Reifen, Kraftstofftemperatur, Kühlluftstrom, Kühlmitteltemperatur, Motoröltemperatur, Abgastemperatur, Luftdruck und Lufttemperatur der Umgebung. Weitere Größen waren während aller Messungen gleich. Hierzu zählen die elektrische Verbrauchsleistungen, die über alle Messungen konstant blieben, Art und Füllstand des Motoröls, Art und Füllstand des Kühlmittels, Belüftungssituation der Zuluft, der Abluft und der Abgasabsaugung. Die Wartung des Fahrzeuges lag rund 2500 km zurück und umfasste neben dem ordnungsgemäßem Ölfilterwechsel den Einbau neuer Zündkerzen und neuer Luftfilter.

Kraftstoffdichte

Vor Beginn der Versuchsreihen wurde die Kraftstoffdichte der jeweiligen Ottokraftstoffe in Abhängigkeit von der Umgebungstemperatur mit einem Aärometer bestimmt. Die Umrechnung der Kraftstoffdichte auf die Normtemperatur (15 °C) erfolgte mit der Gleichung

(2) $$\rho_{15°C} = \rho_{\vartheta} + a \cdot (\vartheta - 15°C)$$

(Faktor a nach DIN 51759).
Die normierten Kraftstoffdichten sind in der Tabelle 4 dargestellt.

Kraftstoff	Kraftstoffdichte		
	ρ [kg/m^3]	t [^{0}C]	ρ_{Norm} [kg/m^3]
BP 98	0,766	14	0,765
Esso Super Plus 98	0,744	12,5	0,742
Shell V-Power 100	0,755	9,5	0,751
Aral Ultimate 100	0,748	11	0,745

Tab. 4. Gemessene und normierte Kraftstoffdichte

Normierte Leistung

Die Motorleistung hängt unter anderem von der Lufttemperatur und dem Luftdruck ab (siehe Gl.1). Um Messungen unter verschiedenen Bedingungen (an unterschiedlichen Tagen oder Tageszeiten) vergleichen zu können, wird die gemessene Motorleistung auf die reduzierte Leistung nach DIN 70200 umgerechnet. Die reduzierte Leistung bezieht sich auf eine Normtemperatur von 20 °C und einen Normluftdruck von 1013 hPa. Die Berechnung erfolgt nach Gleichung:

$$(3) \qquad P_{red} = Ka \cdot P_{mot}$$

Ka ist ein Korrekturfaktor nach DIN 70200; p ist der atmosphärische Luftdruck am Prüfstand in mbar und T ist die Lufttemperatur am Prüfstand in Kelvin. Ka ist wie folgend definiert:

$$(4) \qquad Ka = \frac{1013}{p[mbar]} \cdot \sqrt{\frac{T[K]}{293K}}$$

Testbedingungen

Randbedingungen für alle geplanten Messungen waren gleich und folgendermaßen festgelegt:

- Warmer Motor nach Öltemperatur und Kühlwasseranzeige.
- Fahrzeug warmgefahren (Getriebe, Reifen, etc) nach AUDI-Vorgabe für dieses Fahrzeug am Rollenprüfstand
- Gebläse und Abgasabsaugung immer gleich eingestellt
- Motorölstand und Ölsorte
- Getriebeölstand und Ölsorte
- Kühlwasserstand
- Beladungszustand des Fahrzeugs ist immer gleich (Fahrer +Tankfüllung nach Festlegung, sonst leer)
- Reifendruck immer gleich mit 3 bar auf allen Rädern (kontrolliert)

- Kraftstofftemperatur nahezu konstant mit T_K=18-25 Grad Celsius
- Luftdruck, Lufttemperatur, Luftfeuchte (gemessen)
- Alle Ergebnisse werden normiert und rückgerechnet auf Normbedingungen.

Um ein besonders aussagekräftiges Ergebnis zu erhalten, wurden immer fünf gleiche Messungen durchgeführt und dann gemittelt. So werden lokale Abweichungen wirkungsvoll eliminiert. Des weiteren wurde an drei aufeinander folgenden Tagen mit ähnlicher Witterung (Temperatur/ Luftfeuchte/ Luftdruck), der gleichen abgestimmten Sequenz und nahezu gleichen Tageszeiten gemessen, um vergleichbare Bedingungen zu gewährleisten. Diese Daten wurden direkt am Ansaugtrakt vor dem Fahrzeug aufgenommen.

4. Messergebnisse

4.1. Leistung - Drehmoment Charakteristik

In der ersten Messreihe wurde Shell V-Power geprüft. Die diskrete Leistungsmessung erfolgte in Stufen von 100 U/min und der Drehmomentverlauf wurde vom Prüfstand berechnet. Es wurden 5 Messungen hintereinander durchgeführt und die Einzelwerte zu einer Gesamtkurve gemittelt. Als Zweites wurde nach der erwähnten Spülphase der Kraftstoff Esso SP 98 gemessen. Die dritte Messreihe bezog sich dann auf Aral Ultimate100 – siehe Abb.13.
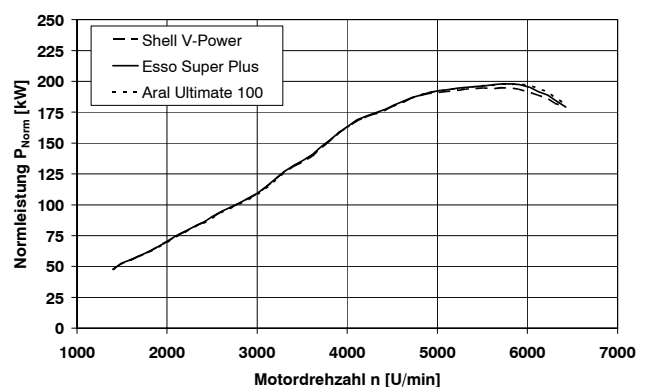
Abb.13. Normierte Leistung als Funktion von Drehzahl für drei getestete Kraftstoffe

Der maximale Unterschied zwischen Esso Super Plus und Shell V-Power beträgt 3.8 kW in einem Drehzahlbereich von 5900 bis 6000 U/min. Das entspricht einem Unterschied von gemittelt 2.0 %. Der maximale Unterschied zwischen Aral Ultimate und Shell V-Power beträgt 5.6 kW bei einer Drehzahl von 6200 U/min. Das entspricht einem Unterschied von 3.0 % - siehe Abb. 14.
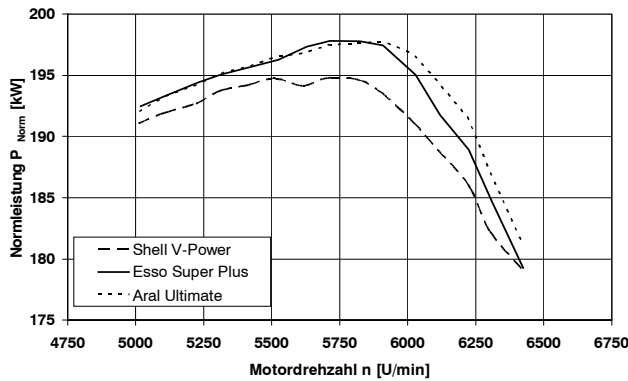
Abb. 14. Normierte Leistung als Funktion von Drehzahl für drei
getestete Kraftstoffe (nur ausgewählter Drehzahlbereich)

Abb.16. Drehmoment als Funktion von Drehzahl für drei getestete
Kraftstoffe (nur ausgewählter Drehzahlbereich)

Die Nennleistung beträgt:

- Shell V-Power: 195 kW bei 5640 U/min
- Esso Super Plus: 198 kW bei 5768 U/min
- Aral Ultimate: 198 kW bei 5820 U/min

Der Unterschied beträgt hier 1.5 %. Somit liegt die Differenz im Rahmen der vom Hersteller des Prüfstandes angegebenen Messgenauigkeit von ± 2 %.

Die Drehmomentverläufe für die drei getesteten Kraftstoffe sind in Abb.15 dargestellt. Erneut ist festzustellen, dass die Unterschiede sehr gering sind, was die detaillierte Darstellung in Abb. 16 zeigt.

Das Nenndrehmoment beträgt:

- Shell V-Power: 390 Nm bei 4075 U/min
- Esso Super Plus: 391 Nm bei 4073 U/min
- Aral Ultimate: 390 Nm bei 4070 U/min

Der Unterschied beträgt hier 0.2 %. Somit liegt die Differenz im Rahmen der vom Hersteller des Prüfstandes angegebenen Messgenauigkeit von ± 1 %.

4.2. Elastizität

Die Erwartungen an diesen Test waren hoch, versprechen die Hersteller doch vor allem ein deutlich verbessertes Beschleunigungsvermögen. Die Ergebnisse beider Tests ergeben sich entsprechend Abb. 17.

Abb.15. Drehmoment als Funktion von Drehzahl für drei getestete
Kraftstoffe
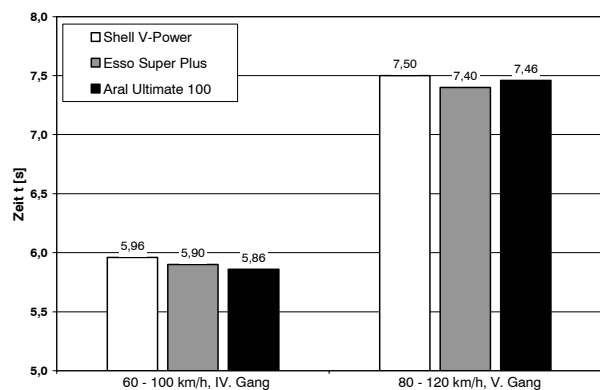
Abb.17. Elastizität (Gang 4 und 5) für drei getestete Kraftstoffe

Der maximale Unterschied zwischen Esso Super Plus und Shell V-Power beträgt 5.8 Nm bei einer Drehzahl von 6000 U/min. Das entspricht einem Unterschied von gemittelt 1.9 %. Der maximale Unterschied zwischen Aral Ultimate und Shell V-Power beträgt 8.4 Nm bei einer Drehzahl von 6000 U/min. Das entspricht einem Unterschied von 2.7 %.

Auch hier zeigen sich nur sehr geringe Abweichungen. Die Abweichungen beim Test von 60 auf 100 km/h im 4. Gang betragen nur etwa 0.1 s im Mittel, was einem Unterschied von 1.7 % entspricht. Ebenfalls eine Abweichung von 0.1 s ergibt die Messung von 80 auf 120 km/h, was einem Unterschied von 1.3 % entspricht.

Die Erwartungen wurden nicht erfüllt. Gerade Shell V-Power verspricht ein verbessertes Beschleunigungsvermögen, erreichte im Test jedoch das schlechteste Testergebnis.

4.3. Kraftstoffverbrauch

Bei allen Leistungspunkten war kein nennenswerter Verbrauchsunterschied feststellbar. Lediglich beim Punkt schwächster Last war mit den Hochleistungskraftstoffen beim spezifischen Verbrauch eine minimale Reduktion feststellbar.
Der volumetrische Kraftstoffverbrauch der getesteten Kraftstoffe ist in Abb. 18 und der spezifische Kraftstoffverbrauch in Abb. 19 dargestellt.
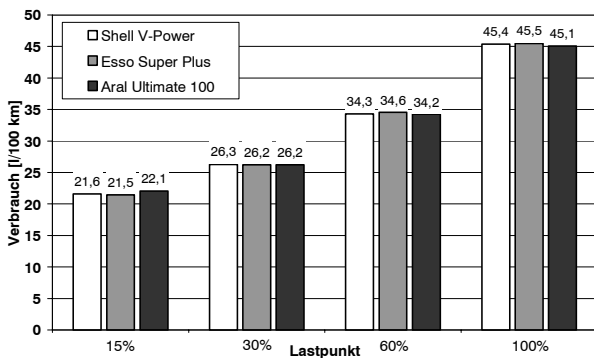
Abb.18. Volumetrischer Kraftstoffverbrauch für vier Lastpunkte
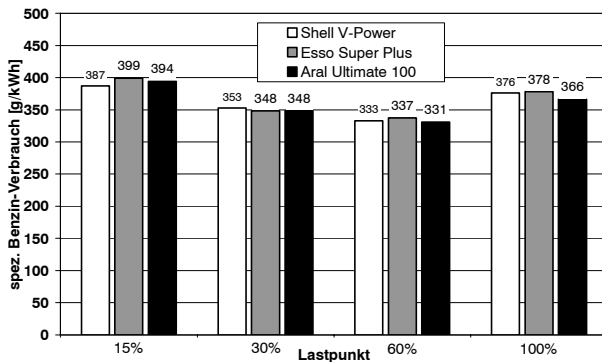
Abb.19. Spezifischer Kraftstoffverbrauch für vier Lastpunkte

5. Fazit

Es wurde festgestellt, dass keiner der beiden Hochoktankraftstoffe relevante Mehrleistung, Drehmomentzuwachs, Verbrauchsersparnis oder Performancegewinn bringt. Die festgestellten Differenzen liegen unter etwa 2% d.h. an der Messgenauigkeitsgrenze. Leistungsmäßig war der Referenzkraftstoff (herkömmliches Super Plus von Esso 98 ROZ) dem Kraftstoff V-Power (100 ROZ) von Shell sogar messbar knapp überlegen. Im unteren Teillastbereich lässt sich bei den Hochoktankraftstoffen eine minimale, jedoch kaum wahrnehmbare Verbrauchsersparnis feststellen, die aber in keinem Verhältnis zum Mehrpreis und den Angaben der Kraftstoffhersteller steht. In konventionellen, weniger auf Leistung ausgelegten Ottomotoren ist eine noch geringere Auswirkung zu erwarten.

Literatur

[1] Abschlußbericht Sonder-Forschungsbereich 224 „Motorische Verbrennung", Aachen 2001.

Development of a finite volume model for the compressible gap flow inside a screw pump

Dipl.-Ing. (FH) Klaus Räbiger
Prof. Dr. T.M.A. Maksoud
Prof. Dr. John Ward

University of Glamorgan
School of Technology
Wales, UK

Prof. Dr. G. Hausmann

Georg-Simon-Ohm Fachhochschule Nürnberg
Fachbereich Maschinenbau und
Versorgungstechnik

Abstract

Screw pumps are widely used in conditions of operation, where a constant flow rate and low pulsation are desirable. The type of screw pump, whose gaps are theoretically investigated in this paper, is a twin screw pump, which is used for multiphase operations. Due to the lack of knowledge concerning the pumping behaviour at very high gas volume fractions up to 100 %, the compressible gap flow inside a screw pump has to be investigated with techniques such as computational fluid dynamics more accurately. The development of a finite volume model for the compressible flow in each gap allows a prediction of the thermodynamic behaviour and of the inner leakage flow rate and thus, the effective flow rate of the pump. The resulting pressure and temperature distributions will enhance the understanding of the pump operation.

Key words : screw pump - finite volume -
gas volume fraction

1. Introduction and literature survey

A screw pump is a special type of rotary displacement pumps, in which a number of screws rotates inside a cylindrical housing. The geometry and rotation of the screws generate a series of closed chambers, which transport the fluid from the low pressure inlet to the high pressure outlet, see figure 1.1.
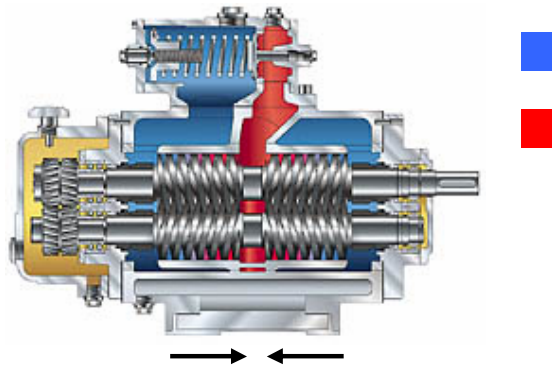
Figure 1.1 : Multiphase screw pump

The pressure distribution through the pump and hence the flow characteristics and system performance is heavily influenced by leakage of the fluid from the discharge side back to the suction side. This leakage flow occurs through three different gaps inside the screw pump, namely the perimeter gap between the screws and the housing, and the radial and flank gaps between the mating surfaces of the screws, see figure 1.2.
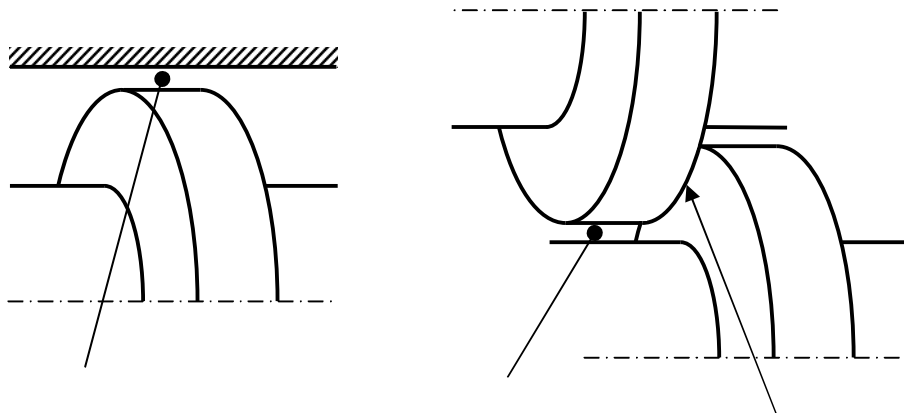
Figure 1.2 : Three different kind of gaps inside the screw pump

Previous investigations of multiphase screw pumps have largely been concerned with the general pumping behaviour of these systems, [1]. Moreover these studies have been restricted to relatively medium sized pumps, in which the maximum power consumption and gas concentrations are relatively modest. In these situations the heat capacity and density of the gas-liquid mixture is dominated by the liquid phase so that the pumping process is mainly isothermal and thermodynamic effects can be neglected, [2] and [3]. However, this assumption cannot be justified for larger, more powerful screw pumps, which are capable of conveying two-phase fluids with very high concentrations of the gaseous phase up to 100 %. On the other hand, past investigations used a more simple theory for the flow through the gaps and often neglect the compressibility of the gaseous phase. Another area of research is the application of screw pumps in blood conveyance. With the focus on low hemolysis, a channel flow model was introduced to investigate the velocity field, the flow rate and the shear stress distribution, [4]. The model was solved by a finite analytical method, with the assumptions, that the fluid is incompressible and the flow is fully developed in channel direction.

Due to the above-mentioned lack of accurate models, it was necessary to create models for the gap flow, using computational fluid dynamic, to predict the leakage flow more accurately. Because of validation reasons and the fact that this first modelling stage refers only to single-phase fluids, the CFD model for the compressible gap flow was analysed for air as an ideal gas.

2. Conservation equations for the gap flow

The governing equations for the flow field inside the three identified gaps can be represented by the compressible Navier-Stokes equation in a vector form as

$$\frac{\partial}{\partial t} I + \frac{\partial}{\partial x} J + \frac{\partial}{\partial y} K + \frac{\partial}{\partial z} L = 0 \tag{2.1}$$

The components of each vector represent sequentially the conservation equations of mass, momentum in three space directions, and finally energy.

Vector, which represents the unsteady term of equation 2.1

$$I = \begin{bmatrix} r \\ r \cdot u \\ r \cdot v \\ r \cdot w \\ r \cdot \left(\frac{p \cdot c_V}{r \cdot R} + \frac{\left(u^2 + v^2 + w^2 \right)}{2} \right) \end{bmatrix} \tag{2.2}$$

Vector, which represents the steady component of equation 2.1 in the x - coordinate direction

$$J = \begin{bmatrix} r \cdot u \\ r \cdot u \cdot u + p - t_{xx} \\ r \cdot u \cdot v - t_{xy} \\ r \cdot w \cdot u - t_{xz} \\ r \cdot u \cdot \left(\frac{p \cdot c_V}{r \cdot R} + \frac{\left(u^2 + v^2 + w^2 \right)}{2} \right) + u \cdot p - u \cdot t_{xx} - v \cdot t_{xy} - w \cdot t_{xz} - k \cdot \frac{\partial T}{\partial x} \end{bmatrix} \tag{2.3}$$

Vector, which represents the steady component of equation 2.1 in the y - coordinate direction

$$K = \begin{bmatrix} r \cdot v \\ r \cdot u \cdot v - t_{xy} \\ r \cdot v \cdot v + p - t_{yy} \\ r \cdot w \cdot v - t_{zy} \\ r \cdot v \cdot \left(\frac{p \cdot c_V}{r \cdot R} + \frac{\left(u^2 + v^2 + w^2 \right)}{2} \right) + v \cdot p - u \cdot t_{yx} - v \cdot t_{yy} - w \cdot t_{yz} - k \cdot \frac{\partial T}{\partial y} \end{bmatrix} \tag{2.4}$$

Vector, which represents the steady component of equation 2.1 in the z - coordinate direction

$$
L = \begin{bmatrix}
\rho \cdot w \\
\rho \cdot u \cdot w - t_{xz} \\
\rho \cdot v \cdot w - t_{yz} \\
\rho \cdot w \cdot w + p - t_{zz} \\
\rho \cdot w \cdot \left(\dfrac{p \cdot c_V}{\rho \cdot R} + \dfrac{\left(u^2 + v^2 + w^2 \right)}{2} \right) + w \cdot p - u \cdot t_{zx} - v \cdot t_{zy} - w \cdot t_{zz} - k \cdot \dfrac{\partial T}{\partial z}
\end{bmatrix}
\tag{2.5}
$$

3. Finite volume approach

The finite volume method is similar to finite differences method (FDM) in that it is a very efficient calculation method in the field of computational fluid dynamics and is characterised as having a high accuracy compared to finite element method (FEM) and by a higher flexibility compared to the FDM.

The finite volume approach, [5] and [6], is to integrate the derivative terms in the Navier-Stokes equations with respect to the three space coordinates over the whole flow domain and then transform the results with the divergence theorem by Gauss.

Integration of the Navier-Stokes equation

$$
\iiint_V \left(\frac{\partial}{\partial t} I \right) dV + \iiint_V \left(\frac{\partial}{\partial x} J \right) dV + \iiint_V \left(\frac{\partial}{\partial y} K \right) dV + \iiint_V \left(\frac{\partial}{\partial z} L \right) dV = 0
\tag{3.1}
$$

Divergence theorem by Gauss

$$
\iiint_V \mathrm{div} F \; dV = \oiint_A F \; dA = \oiint_A \left(F \cdot n \right) dA
\tag{3.2}
$$

$$
A_l = n_l \cdot A_l
\tag{3.3}
$$

Resulting equation (formulation for each cell of the whole flow domain)

$$
\frac{d}{dt} I_{i,j,k} \cdot V_{i,j,k} + \sum_{m=1}^{3} \sum_{l=1}^{6} \left(F_{ml} \cdot A_{ml} \right)_{ijk} = 0
\tag{3.4}
$$

with $m = 1 \dots 3$ for each derivative in the three coordinate directions
            $l = 1 \dots 6$ for each face of the cell, here with a cuboid's shape

The resulting equation 3.4 is already formulated for a 3-dimensional finite volume cell, which will be generated by a structured discretisation of the whole flow domain. As an example, a single cell with all notations can be seen below in figure 3.1.
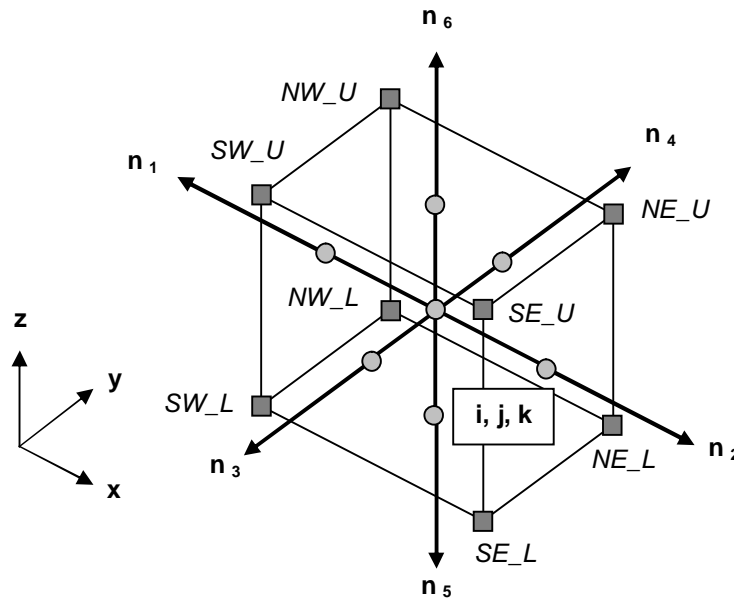
Figure 3.1 : 3-dimensional finite volume cell

The following form of equation 3.4 allows their direct use for the numerical calculation.

$$
\frac{d}{dt}\boldsymbol{I}_{i,j,k} = -\frac{1}{V_{i,j,k}} \cdot
\begin{bmatrix}
(\boldsymbol{J}_1 \cdot A_{11}) + (\boldsymbol{J}_2 \cdot A_{12}) + (\boldsymbol{J}_3 \cdot A_{13}) + \\
(\boldsymbol{J}_4 \cdot A_{14}) + (\boldsymbol{J}_5 \cdot A_{15}) + (\boldsymbol{J}_6 \cdot A_{16}) + \\
(\boldsymbol{K}_1 \cdot A_{21}) + (\boldsymbol{K}_2 \cdot A_{22}) + (\boldsymbol{K}_3 \cdot A_{23}) + \\
(\boldsymbol{K}_4 \cdot A_{24}) + (\boldsymbol{K}_5 \cdot A_{25}) + (\boldsymbol{K}_6 \cdot A_{26}) + \\
(\boldsymbol{L}_1 \cdot A_{31}) + (\boldsymbol{L}_2 \cdot A_{32}) + (\boldsymbol{L}_3 \cdot A_{33}) + \\
(\boldsymbol{L}_4 \cdot A_{34}) + (\boldsymbol{L}_5 \cdot A_{35}) + (\boldsymbol{L}_6 \cdot A_{36})
\end{bmatrix}
\tag{3.5}
$$

In the above expression 3.5, the vector $\boldsymbol{I}$ is defined by the flow condition in the centre of the cell (cell-centred formulation). The vectors $\boldsymbol{J}$, $\boldsymbol{K}$ and $\boldsymbol{L}$ are calculated against it in the middle of the six cell faces A_1 to A_6 by averaged state values of two neighbouring cells.

4. Flux-difference splitting scheme

The flux vector $\boldsymbol{J}$ (see equation 2.3) can be splitted - as well as the flux vectors $\boldsymbol{K}$ and $\boldsymbol{L}$ - into two vectors $\boldsymbol{J_c}$ and $\boldsymbol{J_d}$, which contain on the one side all the convective and on the other side all the diffusive parts.

$$
\boldsymbol{J}_c =
\begin{bmatrix}
\mathsf{r} \cdot u \\
\mathsf{r} \cdot u \cdot u + p \\
\mathsf{r} \cdot u \cdot v \\
\mathsf{r} \cdot w \cdot u \\
\mathsf{r} \cdot u \cdot \left(\dfrac{p \cdot c_V}{\mathsf{r} \cdot R} + \dfrac{\left(u^2 + v^2 + w^2 \right)}{2} \right) + u \cdot p
\end{bmatrix}
\tag{4.1}
$$

$$J_d = \begin{bmatrix} 0 \\ -t_{xx} \\ -t_{xy} \\ -t_{xz} \\ -u \cdot t_{xx} - v \cdot t_{xy} - w \cdot t_{xz} - k \cdot \dfrac{\partial T}{\partial x} \end{bmatrix} \tag{4.2}$$

In contrast to the diffusive fluxes at the cell faces, which can be determined by a central difference scheme, the convective fluxes have to be calculated in a special manner, which supplies, especially the Runge-Kutta scheme, with enough dissipation to prevent possibly arising instabilities. An often used algorithm to calculate the convective flux, is Roe's approximate Riemann solver, [7], which belongs to the flux-difference splitting schemes.

The convective flux through an arbitrary western cell face, see figure 4.1, follows to

$$J_{c,W} = \frac{1}{2} \cdot \left[J_c(I_R) + J_c(I_L) \right] - \frac{1}{2} \cdot \left| A_{Roe} \right|_W \cdot (I_R - I_L) \tag{4.3}$$
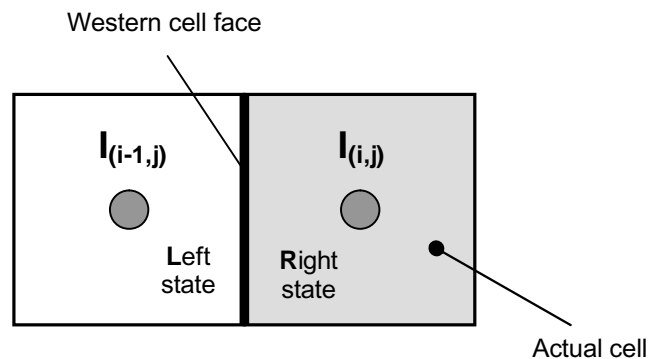
Figure 4.1 : Western cell face and their neighbouring cells

The expression 4.3 is similar to a normal central difference scheme, which includes a dissipation term. The Roe-Matrix A_{Roe} at the current cell face will correspond to the gradient of the convective flux vector with respect to the vector of the conservative variables, if the Roe-averaged variables are used.

The Roe-averaging is a special interpolation scheme of the cell-centre variables of the two neighbouring cells. For the conservative variables follows

$$\tilde{r} = \sqrt{r_L \cdot r_R} \tag{4.4}$$

$$\tilde{u} = \frac{u_L \cdot \sqrt{r_L} + u_R \cdot \sqrt{r_R}}{\sqrt{r_L} + \sqrt{r_R}} \tag{4.5}$$

$$\tilde{v} = \frac{v_L \cdot \sqrt{r_L} + v_R \cdot \sqrt{r_R}}{\sqrt{r_L} + \sqrt{r_R}} \tag{4.6}$$

$$\tilde{w} = \frac{w_L \cdot \sqrt{r_L} + w_R \cdot \sqrt{r_R}}{\sqrt{r_L} + \sqrt{r_R}} \tag{4.7}$$

$$\tilde{H} = \frac{H_L \cdot \sqrt{r_L} + H_R \cdot \sqrt{r_R}}{\sqrt{r_L} + \sqrt{r_R}}$$ (4.8)

with $\quad H = E + \frac{p}{r} = c_v \cdot T + \frac{\left(u^2 + v^2 + w^2\right)}{2} + \frac{p}{r}$ (4.9)

5. Preconditioning

For compressible flows at low Mach numbers, the fluid is almost incompressible. In this case, the system of time-dependent, density-based Navier-Stokes equations will become very stiff. The rate of stiffness can be explained as the ratio of the largest to smallest eigenvalue. The eigenvalues of such a system are

$$\boldsymbol{v} - a \qquad \text{with} \qquad \boldsymbol{v} : \text{total flow speed}$$
$$\boldsymbol{v} \qquad\qquad\qquad\qquad a : \text{speed of sound}$$
$$\boldsymbol{v} + a$$

The central idea of preconditioning, [8], is a creation of a premultiplication matrix for the unsteady terms in the Navier-Stokes equations, which changes the eigenvalues in such a manner, that they get closer together. Due to the fact, that the eigenvalues will have a similar magnitude, the transient vector will be transformed from conservative to primitive variables and premultiplied by the preconditioning matrix.

The transformation process includes the following steps:

The origin is equal to the vector *I*, which contains all transient terms, represented by conservative variables - see term 2.2.

The Jacobian matrix of this vector with respect to the primitive variables

$$\frac{\partial \boldsymbol{I}}{\partial \boldsymbol{P}} = \begin{bmatrix} r_p & 0 & 0 & 0 & r_T \\ r_p \cdot u & r & 0 & 0 & r_T \cdot u \\ r_p \cdot v & 0 & r & 0 & r_T \cdot v \\ r_p \cdot w & 0 & 0 & r & r_T \cdot w \\ r_p \cdot H - 1 & r \cdot u & r \cdot v & r \cdot w & r_T \cdot H + r \cdot c_p \end{bmatrix}$$ (5.1)

with $\quad r_p = \left.\dfrac{\partial r}{\partial p}\right|_T$ (5.2)   and $\quad r_T = \left.\dfrac{\partial r}{\partial T}\right|_p$ (5.3)

and the vector with all unsteady terms, represented by primitive variables

$$\boldsymbol{P} = \begin{bmatrix} p \\ u \\ v \\ w \\ T \end{bmatrix}$$ (5.4)   , will be embedded in the following expression

$$\frac{\partial \boldsymbol{I}}{\partial \boldsymbol{P}} \cdot \frac{\partial}{\partial t} \oiiint_V \boldsymbol{P}\, dV + \oiiint_V \left(\frac{\partial}{\partial x} \boldsymbol{J} \right) dV + \oiiint_V \left(\frac{\partial}{\partial y} \boldsymbol{K} \right) dV + \oiiint_V \left(\frac{\partial}{\partial z} \boldsymbol{L} \right) dV = 0 \qquad (5.5)$$

After some additional mathematical operations, for further details see references [7] and [8], the preconditioning matrix and it's implementation are:

$$\boldsymbol{Q} = \begin{bmatrix} \Theta & 0 & 0 & 0 & \mathsf{r}_T \\ \Theta \cdot u & \mathsf{r} & 0 & 0 & \mathsf{r}_T \cdot u \\ \Theta \cdot v & 0 & \mathsf{r} & 0 & \mathsf{r}_T \cdot v \\ \Theta \cdot w & 0 & 0 & \mathsf{r} & \mathsf{r}_T \cdot w \\ \Theta \cdot H - 1 & \mathsf{r} \cdot u & \mathsf{r} \cdot v & \mathsf{r} \cdot w & \mathsf{r}_T \cdot H + \mathsf{r} \cdot c_p \end{bmatrix} \qquad (5.6)$$

$$\text{with} \qquad \Theta = \left(\frac{1}{v_{ref}^2} - \frac{\mathsf{r}_T}{\mathsf{r} \cdot c_p} \right) \qquad (5.7)$$

$$\boldsymbol{Q} \cdot \frac{\partial}{\partial t} \oiiint_V \boldsymbol{P}\, dV + \oiiint_V \left(\frac{\partial}{\partial x} \boldsymbol{J} \right) dV + \oiiint_V \left(\frac{\partial}{\partial y} \boldsymbol{K} \right) dV + \oiiint_V \left(\frac{\partial}{\partial z} \boldsymbol{L} \right) dV = 0 \qquad (5.8)$$

6. Time stepping method for the gap flow

The time stepping method, which was chosen for this implementation is a fourth-order Runge-Kutta scheme, [6], (fourth-order accuracy in time).

$$\boldsymbol{P}_{i,j,k}^{(0)} = \boldsymbol{P}_{i,j,k}^{(n)} \qquad (6.1)$$

$$\boldsymbol{P}_{i,j,k}^{(1)} = \boldsymbol{P}_{i,j,k}^{(0)} - \mathsf{a}_1 \cdot \frac{\Delta t}{V_{i,j,k}} \cdot \boldsymbol{R}^{(0)} \qquad (6.2)$$

$$\boldsymbol{P}_{i,j,k}^{(2)} = \boldsymbol{P}_{i,j,k}^{(0)} - \mathsf{a}_2 \cdot \frac{\Delta t}{V_{i,j,k}} \cdot \boldsymbol{R}^{(1)} \qquad (6.3)$$

$$\boldsymbol{P}_{i,j,k}^{(3)} = \boldsymbol{P}_{i,j,k}^{(0)} - \mathsf{a}_3 \cdot \frac{\Delta t}{V_{i,j,k}} \cdot \boldsymbol{R}^{(2)} \qquad (6.4)$$

$$\boldsymbol{P}_{i,j,k}^{(4)} = \boldsymbol{P}_{i,j,k}^{(0)} - \mathsf{a}_4 \cdot \frac{\Delta t}{V_{i,j,k}} \cdot \left(\frac{\boldsymbol{R}^{(0)} + 2 \cdot \boldsymbol{R}^{(1)} + 2 \cdot \boldsymbol{R}^{(2)} + \boldsymbol{R}^{(3)}}{6} \right) \qquad (6.5)$$

$$\boldsymbol{P}_{i,j,k}^{(n+1)} = \boldsymbol{P}_{i,j,k}^{(4)} \qquad (6.6)$$

$$\text{with} \qquad \mathsf{a}_1 = 1/2 \,,\; \mathsf{a}_2 = 1/2 \,,\; \mathsf{a}_3 = 1 \text{ and } \mathsf{a}_4 = 1$$

The vector $\boldsymbol{R}$ of the RHS contains all the convective and diffusive fluxes and is expressed by the conservative variables. Because of the preconditioning, the transient vector $\boldsymbol{P}$ includes the primitive variables, so that a re-transformation of variables is necessary at the end of each cell calculation.

7. Discussion of results

7.1 The perimeter gap

The figures 7.1 and 7.2 show the distributions of the velocities in x- and y-direction as a function of the gap height and length inside the perimeter gap, which has a total height of 100 micrometers. In the case of a parabolic velocity profile in x-direction, the viscous force, which is defined by the gradient of the velocity component u in y-direction multiplied with the dynamic viscosity and the wetted area, must be equal to the sum of the pressure forces normal to the channel inlet and outlet.

The figures 7.3 to 7.5 represent the normal behaviour of a compressible gap flow. The density decreases as well as the pressure. The negative pressure gradient in flow direction is the driving force for the fluid motion. The difference between the inlet and the outlet pressure will lead to the above mentioned second force.

The temperature should normally also decreases, but the viscous forces which act on the fluid can heat up the flow through the gap. An indicator for this presumption can be seen in figure 7.5, where the region close to the wall (highest shear stresses) has higher temperature values in contrast to the middle of the gap, where the shear stress is becoming zero.

The figures 7.6 and 7.7 show the time history of the flow variables density, velocities in x- and y-direction, and pressure and also their residuals. All the time-dependent variables should reach a steady-state at the end. For a better verification also the residuals were determined. The residuals are the differences of the flow variables of two consecutive iteration steps and should become smaller with each time step. In the ideal case, they become zero.
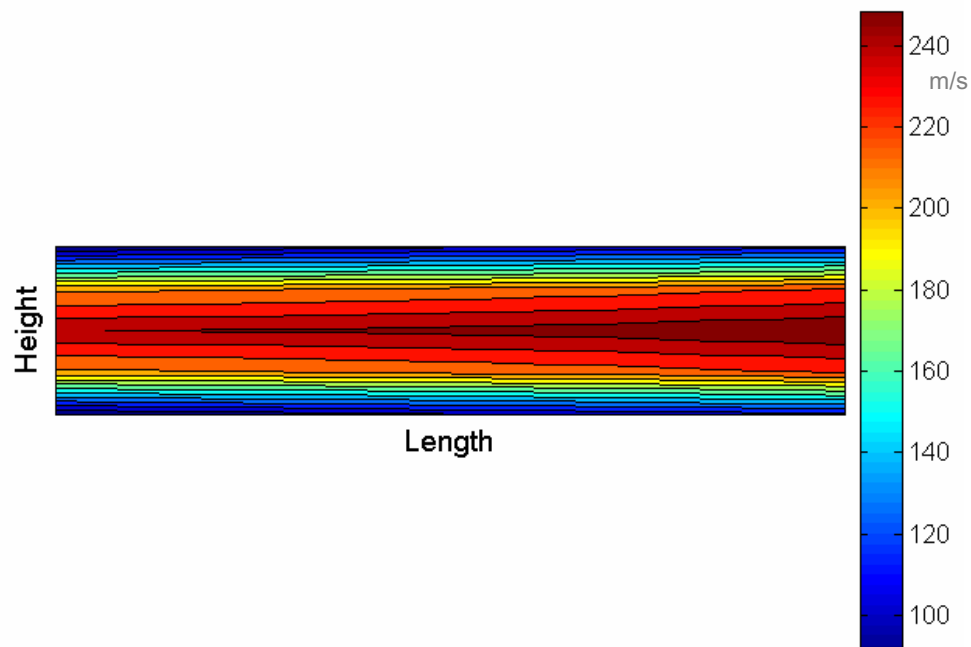
Figure 7.1 : Contour plot of the velocity component u
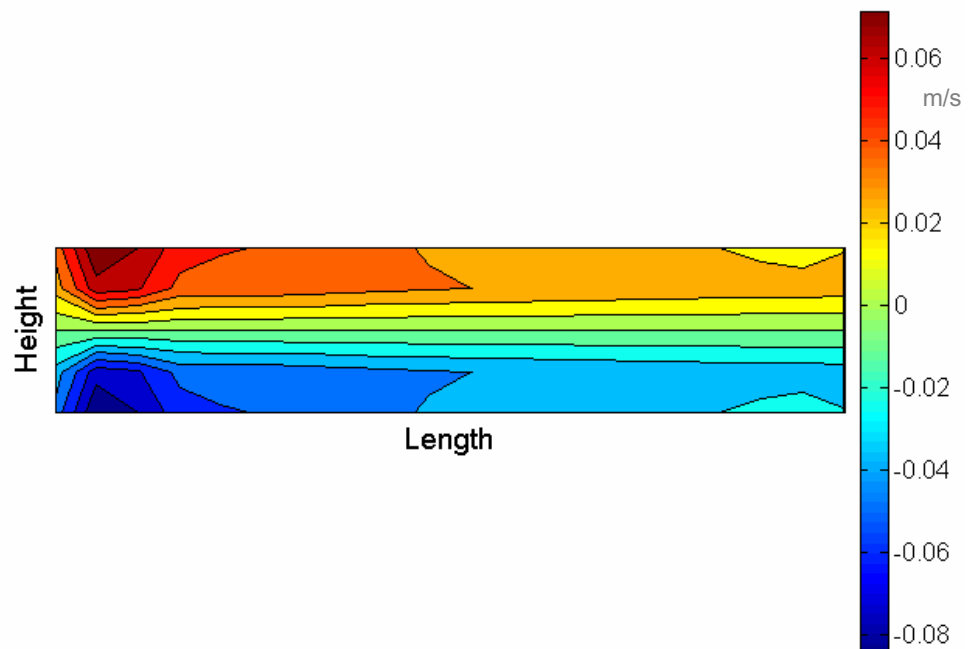
Figure 7.2 : Contour plot of the velocity component v
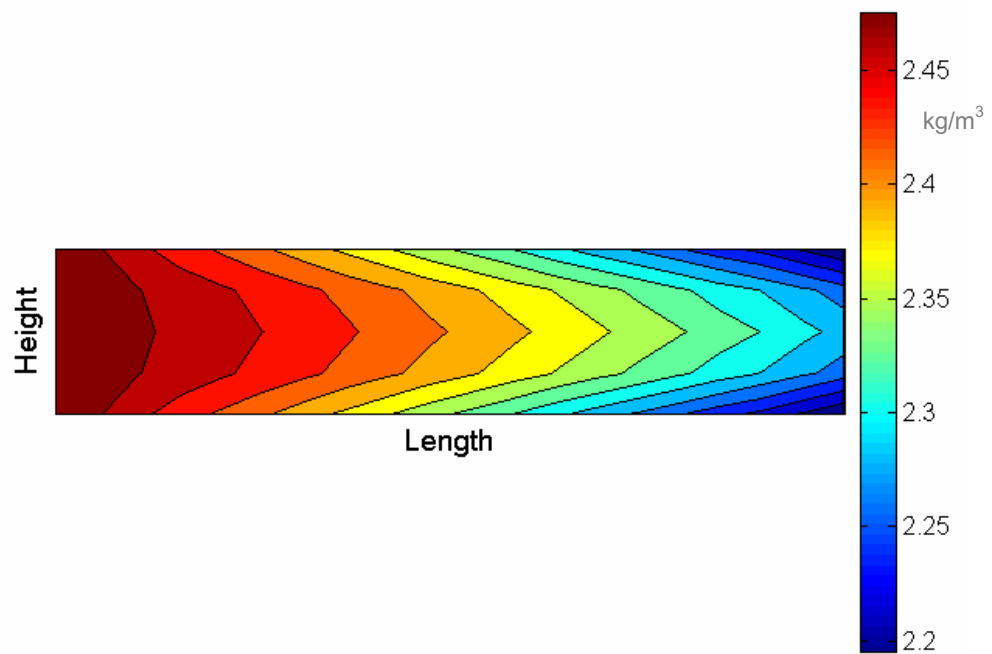
Figure 7.3 : Contour plot of the density
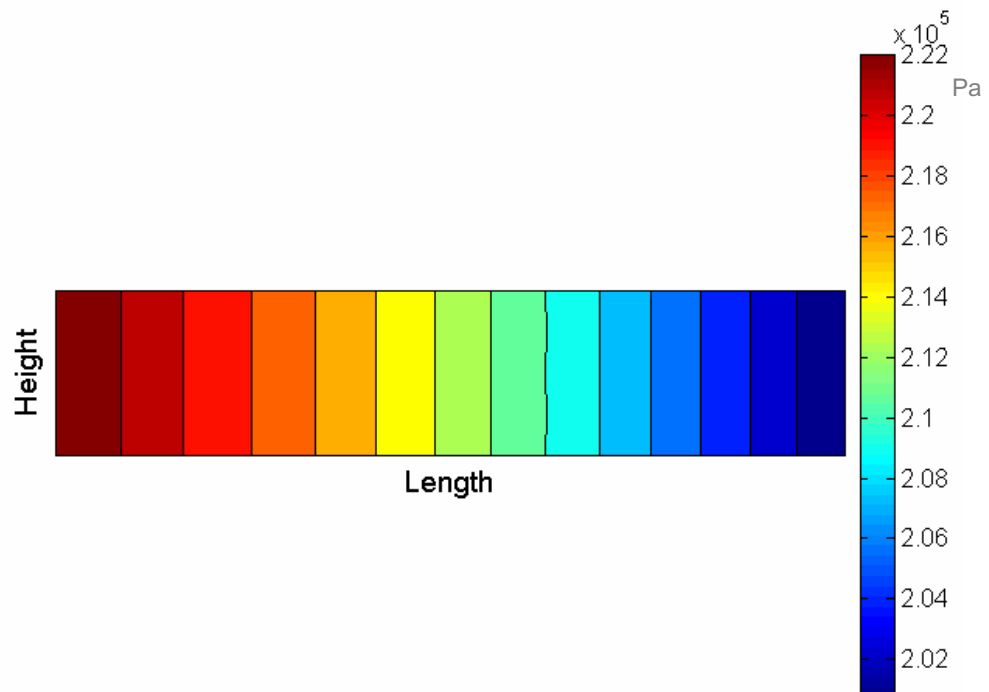
Figure 7.4 : Contour plot of the pressure
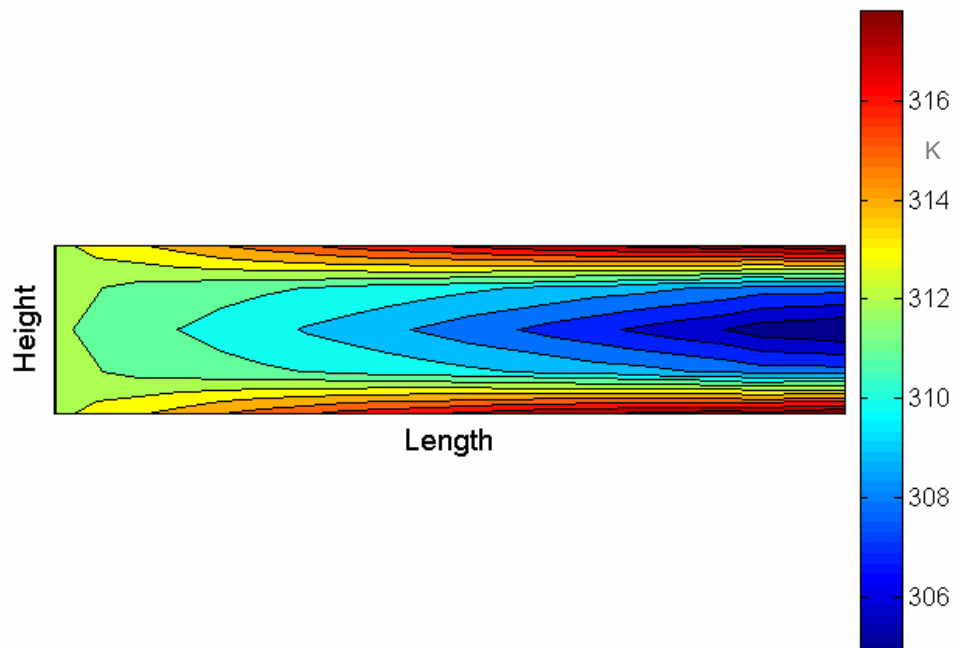
Figure 7.5 : Contour plot of the temperature
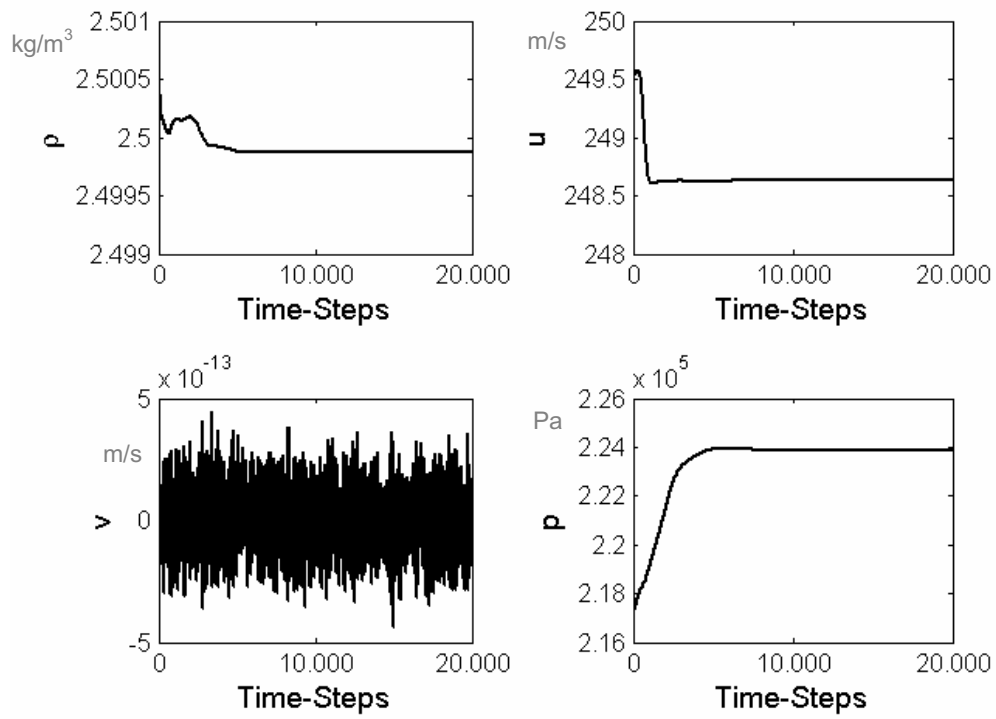
Figure 7.6 : Flow variables as a function of time-steps
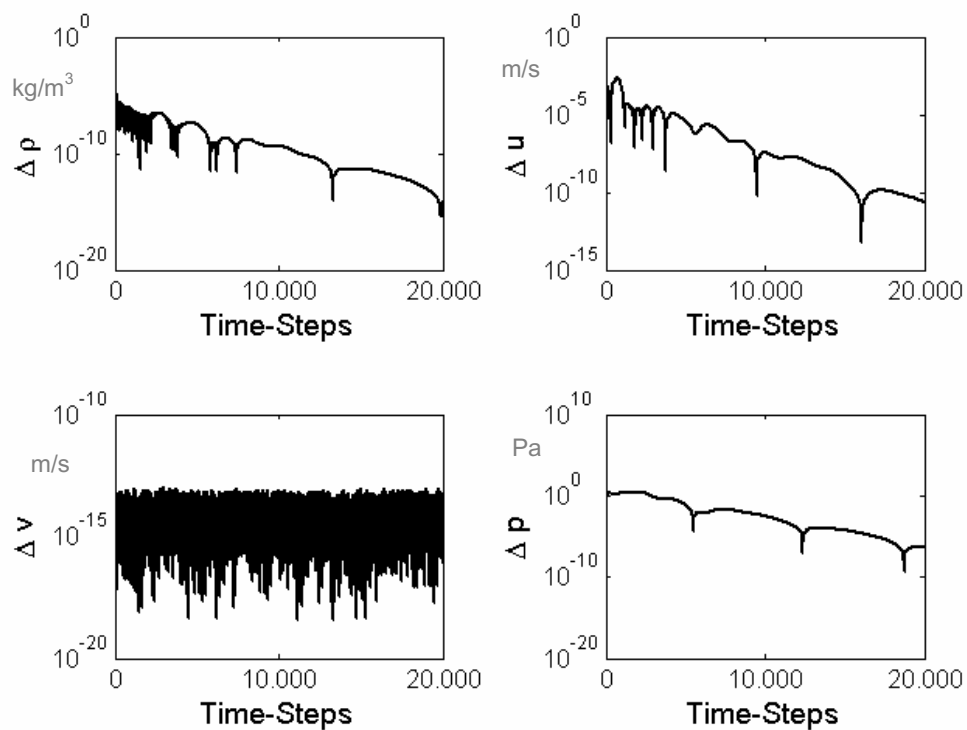
Figure 7.7 : Residuals (logarithmic) as a function of time-steps

7.2 The radial gap

The radial gap - see the white cells in figure 7.8 - is defined by two counter-rotating wheels and has a minimum height of 25 micrometers in this case. The driving forces in this gap, as well as in the general case of the perimeter gap, are the rotating or moving walls and the pressure gradient along the gap axis, where the pressure difference plays the major role.

Figure 7.9 shows the pressure distribution inside the radial gap. The reasons for this distribution are the firstly convergent gap shape and therefore the resulting fluid acceleration and the frictional pressure drop. Due to the large frictional pressure drop, the acceleration pressure drop below the outlet pressure can be seen only to a little extent in the last third of the radial gap.

The time history and the logarithmic residuals of the conservative flow variables as a function of time-steps can be seen finally in the figures 7.10 and 7.11.

Figure 7.8 : Gap geometry in the nip region with surrounding dummy cells
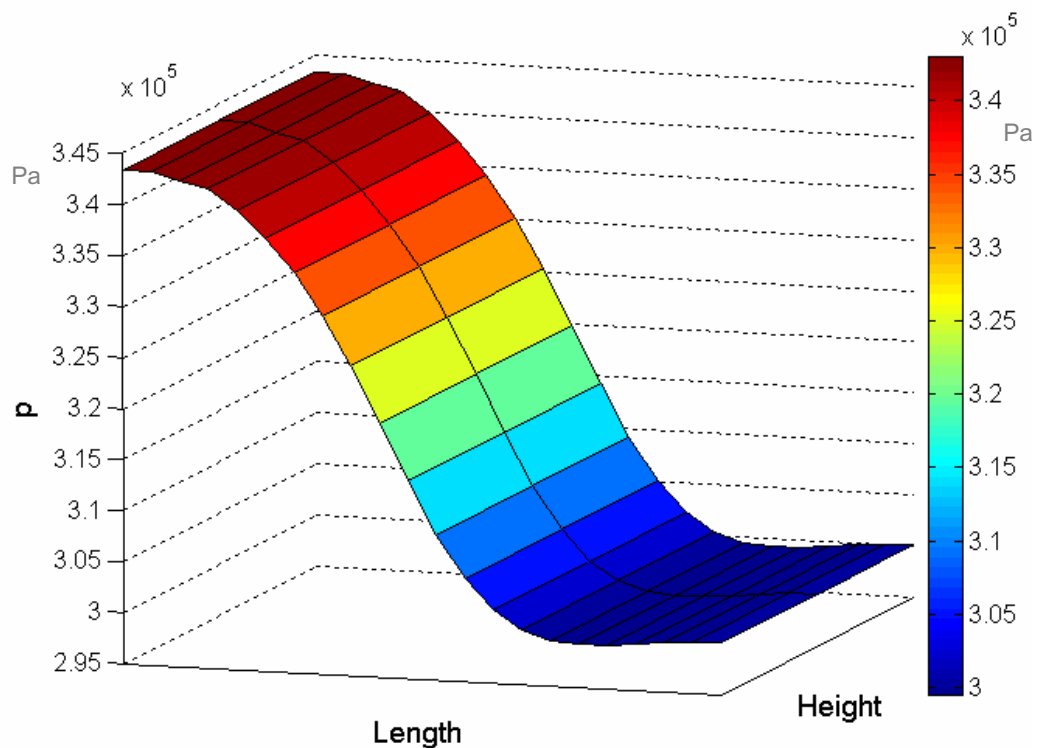
Figure 7.9 : Pressure distribution in the nip region
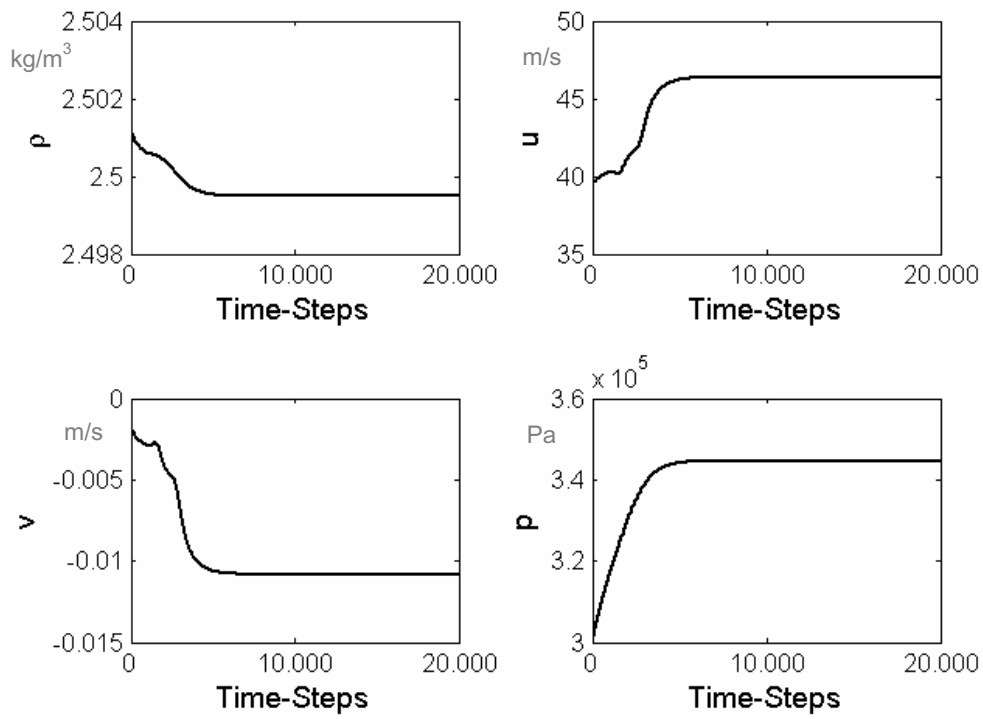
Figure 7.10 : Flow variables as a function of time-steps
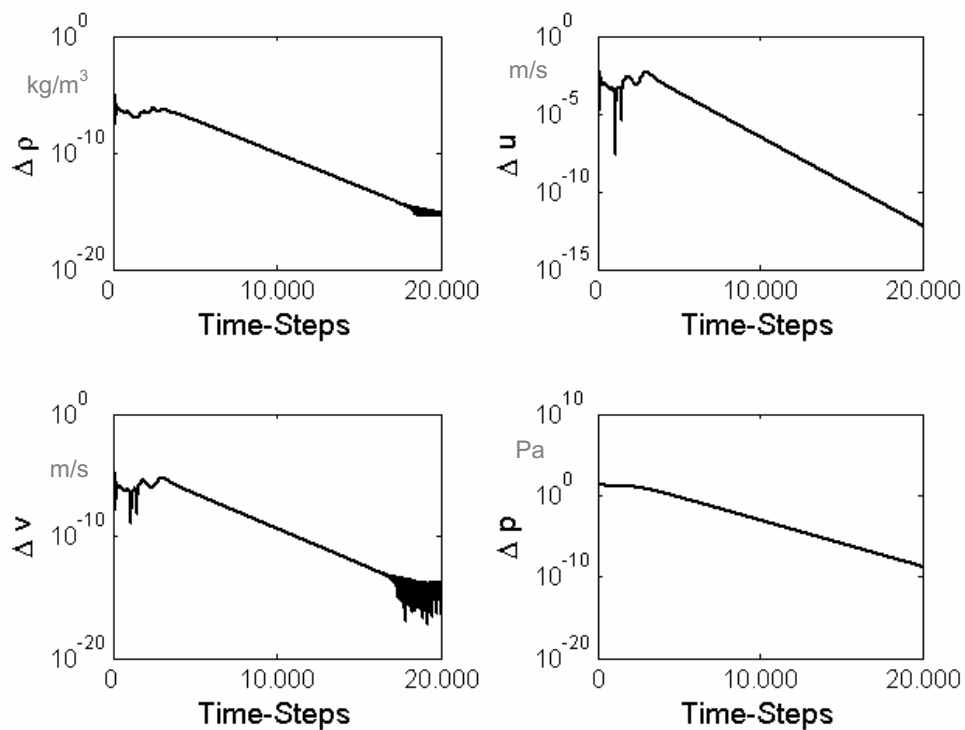
Figure 7.11 : Residuals (logarithmic) as a function of time-steps

7.3 The flank gap

The influence of the rotating flanks, which define the flank gap and also present two velocity boundary conditions as moving walls can be seen in figure 7.12 as a velocity vector plot. The reason for the high concentration of velocity vectors at both ends lies in high number of cells, which are becoming smaller and smaller.

Figure 7.13 shows, the velocity vector plot of the fluid, which flows between the rotating flanks and is also driven by a negative pressure gradient. The contour plot of the total velocity in the middle of the flank gap (y=0), is shown in figure 7.14. The positions of both velocity maximums are self-evident from the velocity boundary conditions of figure 7.12 or the fact that large distances from the centre of rotation will lead to high wall velocities. The positions correlate with the positions of a large radius of the rotating flanks and therefore high velocities.
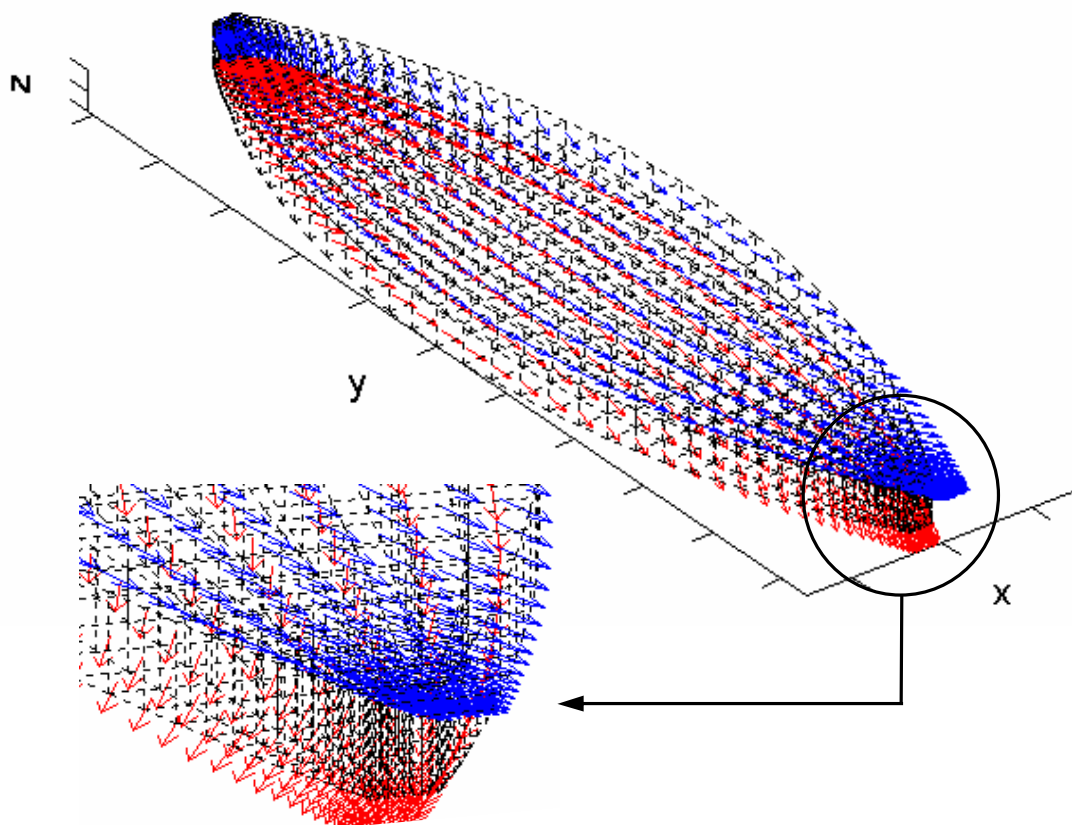
Figure 7.12 : Velocity boundary conditions
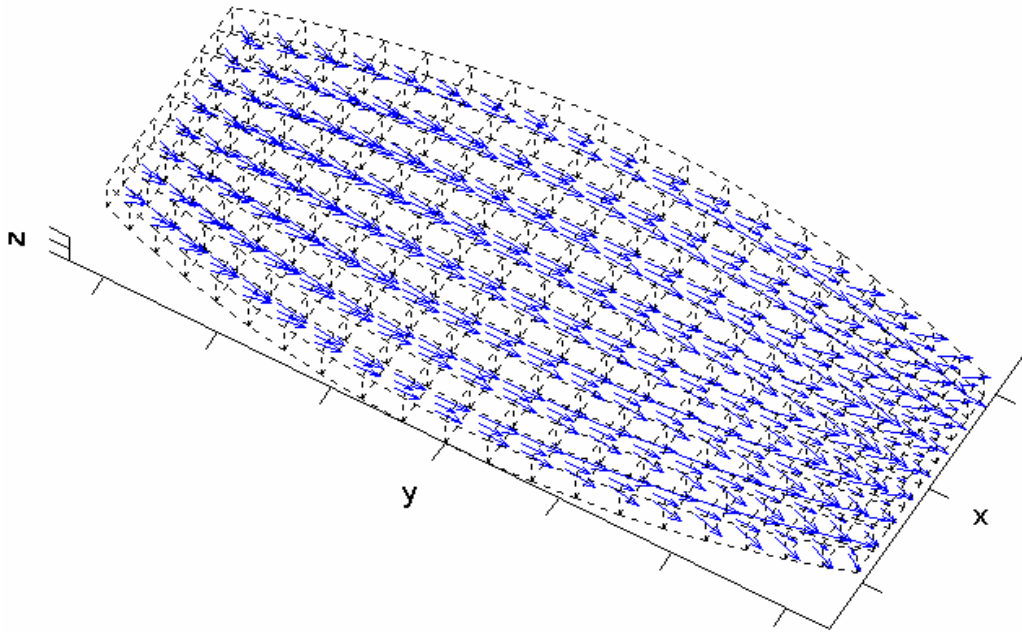
Figure 7.13 : Velocity vector plot (middle section)
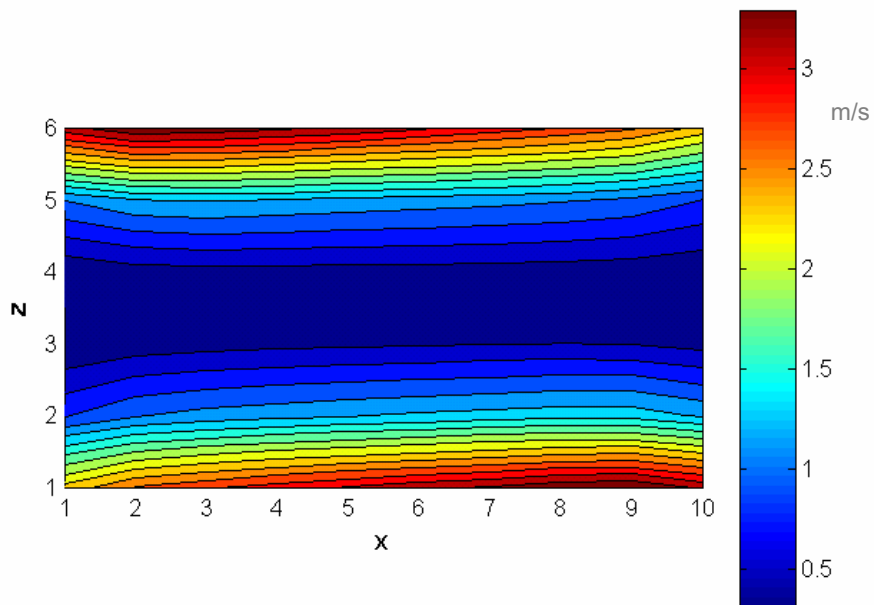
Figure 7.14 : Contour plot of the total velocity

8. Conclusion

The compressible flow through the perimeter gap, radial gap and the flank gap is responsible for the leakage of the whole screw pump. The exact calculation of the leakage flow rate and thus the net flow rate of the pump could be carried out by computational fluid dynamics. A finite volume model, which is programmed and solved in MATLAB, will be able to determine the one-, two- and three-dimensional distributions of the fluid variables density, velocities in all domain directions, pressure and temperature inside the gaps. The program has a very flexible structure and parametric studies concerning the boundary conditions are possible. The boundary conditions are easily defined by the density and velocities at the inlet, the pressure at the outlet, the moving walls and the geometry of the corresponding type of gap. Due to the compressibility of the fluid, which was taken into consideration with this finite volume model, the thermodynamic behaviour could be estimated. This fact will be particularly important in the field of multiphase operations with very high gas-volume-fractions, where the poor liquid phase is not able to absorb the compression heat of the gaseous phase.

Nomenclature

General Symbols

a	speed of sound
A	area of a cell face
c	specific heat capacity
e	specific internal energy
E	total internal energy
H	total enthalpy
k	thermal conductivity
p	static pressure
R	gas constant
t	time
T	temperature
u, v, w	velocity component in x, y and z - direction
v	total flow speed
V	cell volume
x, y, z	coordinates

Vectors / Matrices

A	normal vector multiplied by the cell face area ; Roe Matrix
I	parts of the Navier-Stokes equation, which are differentiated with respect to t
J, K, L	parts of the Navier-Stokes equation, which are differentiated with respect to x, y and z
n	normal vector
P	vector of primitive flow variables
Q	preconditioning matrix

Greek Letters

α	Runge-Kutta factor
μ	dynamic viscosity
ρ	density
τ	shear stress
Θ	auxiliary term in the preconditioning matrix

Subscripts

c	convective
d	diffusive
E, N, S, W	cardinal points : east, north, south and west
i, j, k	cell indicators

l	cell face area index
L	lower ; left
m	coordinate direction index
p	constant pressure ; derivation with respect to pressure at constant temperature
R	right
T	derivation with respect to temperature at constant pressure
U	upper
v	constant volume
V	volume
x, y, z	coordinates

Superscripts

n	current time step
n+1	following time step

References

[1]   WINCEK, M.:
Zur Berechnung des Förderverhaltens von Schraubenspindelpumpen bei der Förderung von
Flüssigkeits / Gas-Gemischen, Dissertation,
Universität Erlangen-Nürnberg, 1992
(The calculation of the conveyance behaviour of screw pumps at the conveyance of liquid/gas-
mixtures, Ph.D. thesis, University of Erlangen-Nuremberg, 1992)

[2]   KÖRNER, H.:
Zum Förderverhalten von Schraubenspindelpumpen für Zweiphasengemische
hohen Gasgehalts, Dissertation,
Universität Erlangen-Nürnberg, 1998
(The conveyance behaviour of screw pumps for two-phase mixtures with high
gas-volume-fractions, Ph.D. thesis, University of Erlangen-Nuremberg, 1998)

[3]   ETZOLD, S.:
Verlustanalyse von Schraubenspindelpumpen bei Mehrphasenförderung,
Dissertation, Universität Hannover, 1993
(Leakage analysis of screw pumps during multiphase conveyance,
Ph.D. thesis, University of Hanover, 1993)

[4]   KILANI, M.I. / JAW, S.Y. / HAIK, Y. / CHEN, C.J.:
Numerical simulation of flow in a screw pump,
Fourteenth Engineering Mechanics Conference, EM 2000
American Society of Civil Engineers, May 21-24, 2000

[5]   OERTEL JR., H. / LAURIEN, E.:
Numerische Strömungsmechanik (Numerical fluid mechanics), Springer-Verlag, Berlin Heidelberg,
1995

[6]   WENDT, J.F.:
Computational Fluid Dynamics, Springer-Verlag,
Berlin Heidelberg, 1996

[7]   BLAZEK, J.:
Computational Fluid Dynamics: Principles and Applications, Elsevier,
Oxford, 2001

[8]   WEISS, J.M. / SMITH, W.A.:
Preconditioning applied to variable and constant density flows,
AIAA Journal, Volume 33, Number 11, Pages 2050-2057

Local Radio in the 26 MHz Band using DRM - Results of the Nuremberg Field Trial and General Considerations

Prof. Dr. Thomas Lauterbach

Georg-Simon-Ohm-Fachhochschule Nürnberg
Fachbereich Allgemeinwissenschaften

Kesslerplatz 12, 90489 Nürnberg

Abstract

Using DRM in the 26 MHz band is an interesting option for local braodcasting. A field trial was set up with two low power DRM transmitters in the area of Nuremberg.

Mobile reception was found to be possible at distances of up to 20 km to the transmitter. However, audio dropouts due to flat fading in the multipath channel were frequently observed at low vehicle speed.

Fixed reception with outdoor antennas was found to be possible at distances of more than 40 km. An overall availability of the audio signal of 99.2 % was achieved at seven different locations during ten days. Long term recordings of several hundreds of hours at one location showed that audio availability was better than 97% in many cases but was reduced at times by local sources of noise and interfering signals from distant stations when ionospheric scattering was possible due to high solar activity and sporadic E layers.

Based on these findings it is concluded that for service planning the same procedures as for VHF transmitter networks can be applied. However to avoid interference by ionosperic scattering, co-channel transmitter must be seperated by at least 2500 km. Therefore, only one channel will be available in each place.

Introduction

The digitisation of terrestrial audio broadcasting is in progress. DAB, the digital radio system for the VHF broadcasting bands is already established in many countries. DAB is best suited for a situation where a large area, e.g. a whole country is to be covered by typically $5 - 7$ programmes, because it bundles several programme services in what is called an "Ensemble". This programme multiplex is transmitted by an OFDM system using a bandwidth of 1.536 MHz. In VHF (normally Band III, around 225 MHz), large area Single Frequency Networks (SFNs) are possible and have already been implemented in several countries. When using such SFNs, DAB is quite effective in terms of spectrum usage and required transmitter power. In most countries, however, there are also local broadcasting stations which now use VHF- FM or AM in the medium wave band. For the transition to digital broadcasting, in bigger cities, normally several of these stations can be bundled to form a DAB Ensemble. In Germany and Canada, e.g., such local DAB Ensembles are broadcast in the L-Band ($1452 - 1492$ MHz) in many cities. Due to the propagation characteristics in this frequency range, however, high power and antennas on high towers are required and indoor-coverage is particularly difficult to achieve. Especially the coverage of outer suburbs of bigger cities needs the use of gap fillers or coverage extenders [1]. In many situations, however, the capacity provided by a DAB Ensemble will not match the needs of local broadcasting. If for instance in a bigger city there are eight or nine local broadcasters, this would require operating two DAB networks, where the capacity of both networks is used only partially. If in a smaller town or rural area there is only a single local station, a DAB network would be used only to 1/6 of its capacity. This will not be possible in an economically reasonable way and will be a waste of spectrum.

Therefore the question arises if the digital transmission system for the broadcasting bands below 30 MHz, i.e. long wave (LW), medium wave (MW), and short wave (SW) developed by the DRM consortium could be an attractive solution for single local stations in situations where DAB can not offer an ideal solution. This report briefly reviews the properties of the DRM system and the propagation conditions in the above mentioned broadcasting bands. After this the setup and the findings of a field trial which is currently carried out at the Georg-Simon-Ohm-Fachhochschule Nürnberg are reported. From these results a possible scenario for local broadcasting in particular in the 26 MHz broadcasting band using the DRM system is developed and the foreseeable limitations of such a service are lined out.

The DRM system

The DRM consortium has developed a digital broadcasting system for the broadcasting bands below 30 MHz, shortly referred to as the DRM system. Its specification is public [2] and transmissions on the respective bands have started some years ago. The main concern of DRM was to improve the audio quality of broadcasts in the LW, MW, and SW broadcasting bands. Another important target was to improve the user friendliness of receivers by sending station identification and tuning information along with the audio in a separate channel. The main features of the DRM system are described in the DRM consortium's Broadcaster's User Manual [3] and several review articles [4-6].

Concerning the issue of local broadcasting, the DRM system is able to offer high audio quality by using the MPEG AAC coding scheme with Spectral Band Replication (SBR). This coding algorithm allows to achieve an audio quality which subjectively comes close to that of VHF-FM in many cases, even though only a data rate of approximately 20 kbit/s available in a 10 kHz wide DRM transmission is used. In the ground wave propagation situation which will most likely occur in local broadcasts only a small overhead for error correction is needed and hence DRM can provide a high data rate for audio. However, in such a configuration, the required signal-to-noise-ratio (SNR) at the receiver input may be as high as $20 - 30$ dB, which will be difficult to achieve when mobile and in-door-reception is desired and low power transmitters are used by local stations.

The DRM system offers all service information features known from e.g. the Radio Data System (RDS) of VHF-FM or DAB such as service label, programme type, and announcement switching (similar to the TA/TP mechanism of RDS, but with extended functionality). Besides that, text messages can be sent along with the audio, and even the transmission of multimedia data such as electronic newspapers and slide shows is possible and has been demonstrated, although the loading time is significant (several minutes) due to the limited data rate available if high audio quality is to be maintained.

Therefore, a local service broadcast on DRM would not appear much different to the listener than a service broadcast on VHF-FM with RDS or on DAB, except that the audio quality will be slightly reduced

(e.g. no stereo or restricted audio bandwidth to e.g. 11 - 15 kHz) and the data rate available for pro-gramme associated data is considerably lower (e.g. in the order of 1 kbit/s instead of e.g. 16 kbit/s in DAB). When considering the use of portable or "kitchen radios" these differences will not matter, for mo-bile reception some more detailed consideration is necessary because the audio system in high level cars is quite developed and the difference in sound quality between a DRM and DAB broadcast will be per-ceivable – the same will of course be true for home HiFi equipment.

Choice of frequency for DRM local broadcasts

The most important question in the context of using the DRM system for local radio is the availability of channels and the propagation characteristics of the broadcasting bands in the range DRM is designed for, i.e. below 30 MHz.

Medium wave

Many local stations today use MW frequencies (525 – 1605 kHz). The MW band however shows very dif-ferent propagation during day time and night time. During day time, only ground wave propagation occurs with higher attenuation of the frequencies near the upper end of the band than for the frequencies at the low end. Therefore, for local broadcasting, the range around 1500 kHz seems to be most appropriate, be-cause the channels can be re-used in a short distance from a transmitter. This however is different at night. Then, in addition to ground wave propagation, sky wave propagation allows propagation over sev-eral hundreds to thousands of kilometres. The re-use distance of MW channels during night time would therefore have to be several thousands of kilometres – this however can not be accommodated in plan-ning. Therefore, co-channel interference occurs during night time which significantly reduces the day time coverage area. First results from field trials in the Medium Wave band confirm these considerations and show a strong reduction in service area during night time [7].

Other problems encountered with MW are the requirement of high antenna towers and a significant level of man-made-noise especially in urban areas.

Short wave

A number of broadcasting bands are available in the short wave part of the spectrum (2 – 30 MHz). Ground wave propagation is normally not used in these bands due to the high attenuation. The coverage is solely achieved by sky wave propagation. Most of the bands allow for propagation to a specific target area only for some time of the day, and this changes with the daily conditions of solar activity, seasonally and in conjunction with the 11 year sunspot cycle. Therefore, in international broadcasting, several fre-quencies in different bands are used in parallel and not all bands can be used during all times of the day and the year.

For the use of local broadcasting those bands can be used which do not allow for long distance coverage for most of the time. They are hardly used by international broadcasters and for most of the time there is no co-channel interference from distant stations through ionospheric scattering.

This is true in particular for the 11m broadcasting band (25670 – 26100 kHz). Therefore our study aims at this frequency range. In addition to setting up two experimental low power DRM transmitters we per-formed an analysis of the restrictions with regard to channel assignment and planning if this band were widely used for local broadcasting as is suggested by the DRM consortium (Ref. [3], p. 47).

The Nuremberg / Dillberg field trial
Setup of the field trial

Due to the propagation conditions in the 26 MHz band, reasonable results concerning the reliability of coverage can only be obtained in a long term test covering all seasons of the year. Of course issues re-lated to the 11 year sunspot cycle can only be investigated at much longer time periods and can not be expected to show up in the results for only 2 years of operation.

Other important topics that were addressed in our study are:

- to show that DRM local broadcasting stations can be set up with minimal hardware effort,

- to study the interference from sky wave propagation phenomena at different seasons of the year.
- to investigate mobile reception in the 26 MHz band,
- to investigate stationary reception, in particular in-door-reception and the impairments resulting from local noise sources.

We obtained two licenses for experimental transmissions in the 26 MHz band from two transmitter sites. The main features of the two transmitters are listed in Table 1.

Table 1. Characteristics of the transmitters used in the trial

	FH - Nuremberg	Dillberg
Location	49°27'10" N 11°05'40" E	49°19'28" N 11°22'55" E
Height a.s.l.	300 m	600 m
Frequency	26012 kHz	26000 kHz
Antenna	Half wave dipole	Vertical half wave antenna
Height of Antenna above ground	30 m	5 m
E.I.R.P	10 W	100 W
Operation	March 2003 – January 2005	Since February 2004

Both transmitters are usually operated with the following parameters:

Robustness Mode   A
SDC Mode   4 QAM
MSC Mode   16 QAM
Spectrum Occupancy   3 (10 kHz band width)
MSC Cell Interleaving   2 s
Equal Error Protection, code rate 0.62.
Audio: Mono signal   18 kbit/s using AAC-SBR
Programme service: FH Nuernberg Campus Radio.

The details of the transmitter and receiver hard- and software setup have already been published [8] and can also be found in the internet [9].

Results of the field trial
Mobile reception

After setting up the transmitters we investigated their respective coverage areas by mobile reception tests. A short vertical dipole antenna (1m long) was used together with a DRM – modified Yaesu FRG 100 receiver and the DREAM or DRM software radio for decoding the signal on a notebook computer which was operated on its internal battery to avoid noise. Some of the tests were made using a RF systems DX 500 short active antenna and a DRM – modified AOR 5400 receiver. In the area where both set-ups were used there was no significant difference in reception performance.

The main emphasis on this investigation was on audio quality, because field strength is not a sufficient planning parameter due to different noise levels and dropouts due to multipath fading. Therefore we took the percentage of correctly decoded audio frames which is also logged by the DRM software receivers as a measure for the quality of reception. In the maps (Figs. 1 & 2) the results are coded by their colour: green: > 75% of audio frames decoded correctly, yellow: > 50% of audio frames decoded correctly and red: <50% of audio frames decoded correctly.
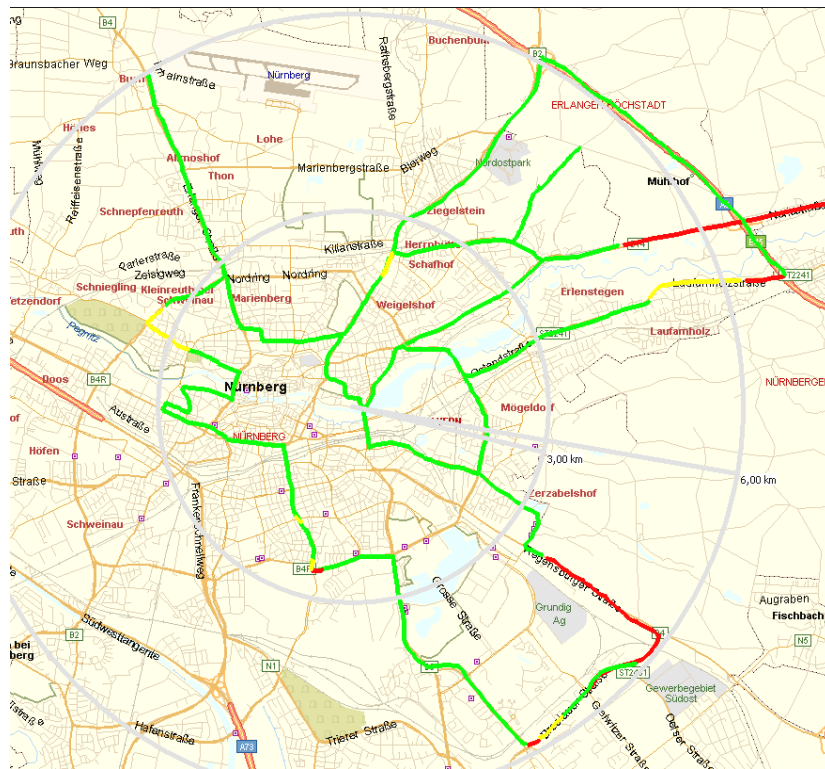
Fig. 1: Service quality within the range of the Nuremberg Transmitter.
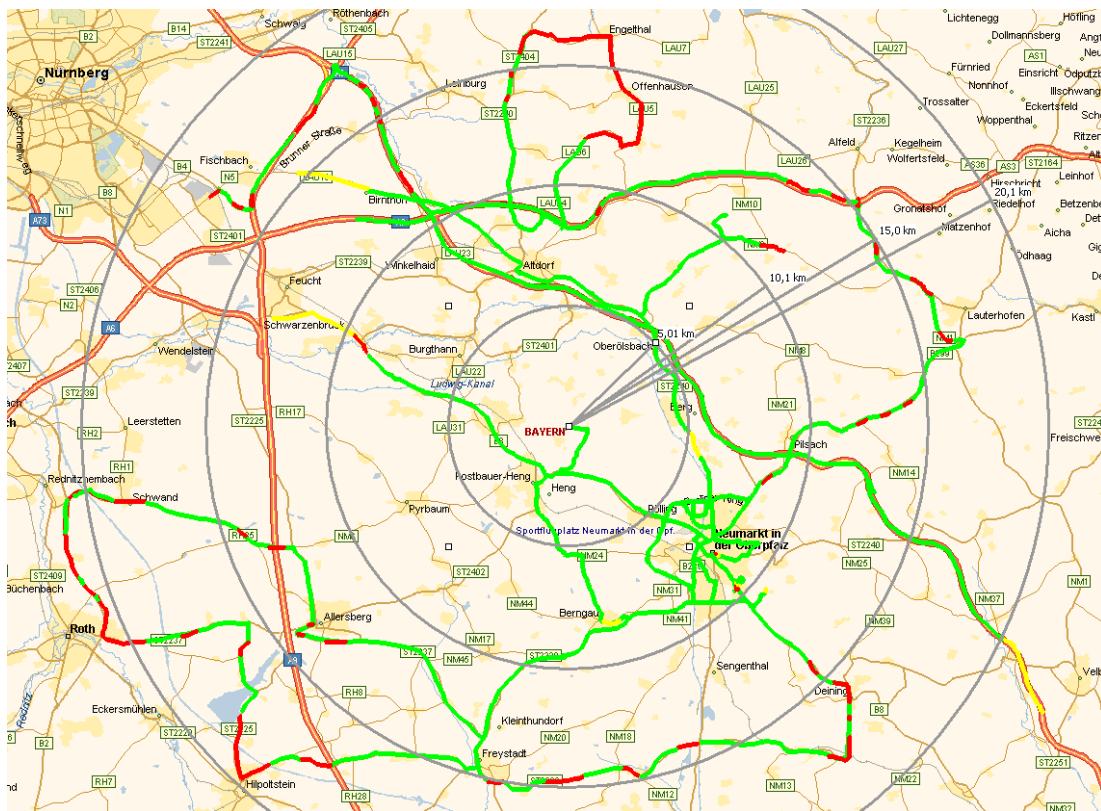
Fig. 2: Service quality within the range of the Dillberg transmitter.

In practice, however, we find sharp transitions from perfect reception (100% correctly decoded frames) and total dropout. The areas where interrupted reception occurs are very small, usually in the order of few hundreds of metres at the fringe of the coverage area.

The results shown in Figures 1 and 2 show that the transmitters have a range of approximately 3-5 km (Nuremberg) and up to 15 km (Dillberg), depending on the terrain and density of buildings. In particular the landscape is rather flat towards the south and west of Dillberg, while it is rather hilly to the north and east. This corresponds to a wider coverage range towards the south west (extending to almost 25 km for mobile reception) while the range is limited to the line-of-sight slopes of the hills in the north and east. This concerns the areas of Deining, Lauterhofen and Engelthal – Offenhausen, which are rather close to the transmitter but are shaded by hills in the direction of the transmitter site. It was also noticed that reception was generally better in areas without dense woods and that at the same distance to the transmitter shadowing from trees impaired reception (e.g. in the Hilpoltstein and Freystadt area, at the south fringe of the mobile range of the Dillberg transmitter).

Both the results for Nuremberg and the Dillberg area are in good agreement with data gained by Deutsche Welle in the same area [10]. They were also able to measure field strength using a calibrated setup with a Rohde & Schwarz HE010 vertical active antenna and a Rohde & Schwarz EB 200 measurement receiver.

Their results indicate that audio reception (threshold: 60% of the audio frames decoded correctly) is possible when the field strength is above 23 to 26 dBμV/m which is somewhat higher than the value of 17.6 dB(μV/m) which the ITU proposes as a planning parameter for the DRM mode used in our transmission [11]. This may be due to the higher man made noise in the city of Nuremberg and along the motorway where most of the field strength values were actually measured, in addition, due to multipath fading (see below) a higher level is required for reception than for stationary reception.

Generally we find reception problems in villages and in particular in the bigger cities (Nuremberg, Neumarkt). This is apparently due to the higher noise level and possibly also caused by multipath propagation due to reflected signals from buildings. We investigated this issue further by recording receiver input power along several streets at different distances from the Nuremberg transmitter.

Fig. 3 shows the locations of the measurement sites, Fig. 4 shows a typical result. The occurrence of fading can clearly be seen. The statistical analysis shows that the results in most locations can be interpreted as caused by a Rayleigh channel (Fig. 5). This means that the received signal is a superposition of scattered components without a direct ray. This is plausible because of the relatively low height of the transmission antenna above ground. Due to the small bandwidth of the signal this fading is not frequency selective but flat (Fig. 6). This is caused by the fact that due to the low transmitter powers only reflected signals from the vicinity of the receiver contribute to the received signal leading to a delay spread in the order of only few microseconds. Hence the coherence bandwidth of the channel is in the range of several hundred kilohertz. This indicates that at the frequency of 26 MHz we must consider reflections from buildings leading to flat fading as a main cause of reception problems in cities.
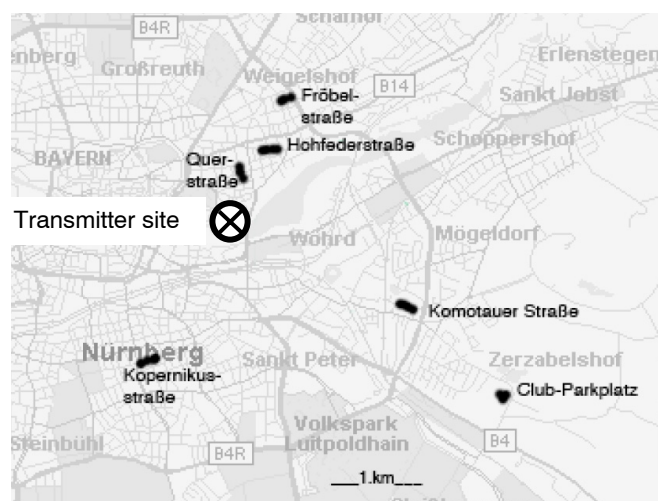
Fig. 3: Sites in Nuremberg where receiver input power along ways of several hundred metres was recorded [12].
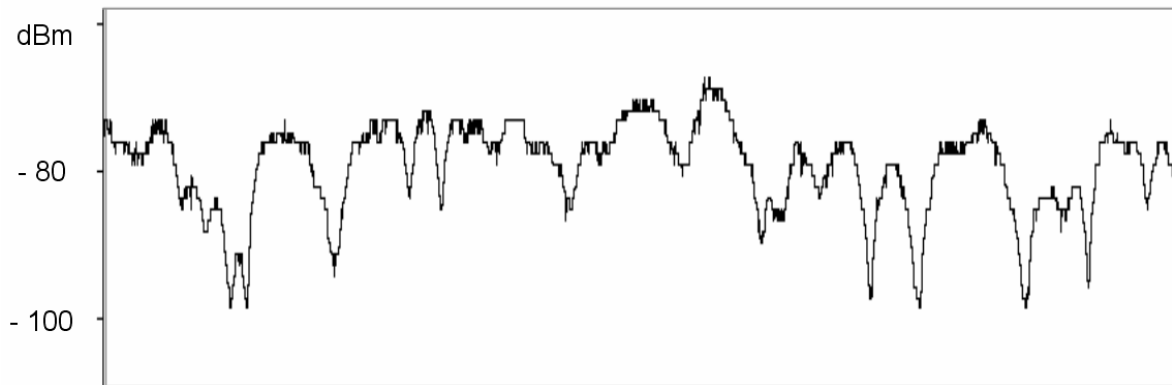
Fig. 4: Receiver input power along a route of 200m at Club-Parkplatz [12].
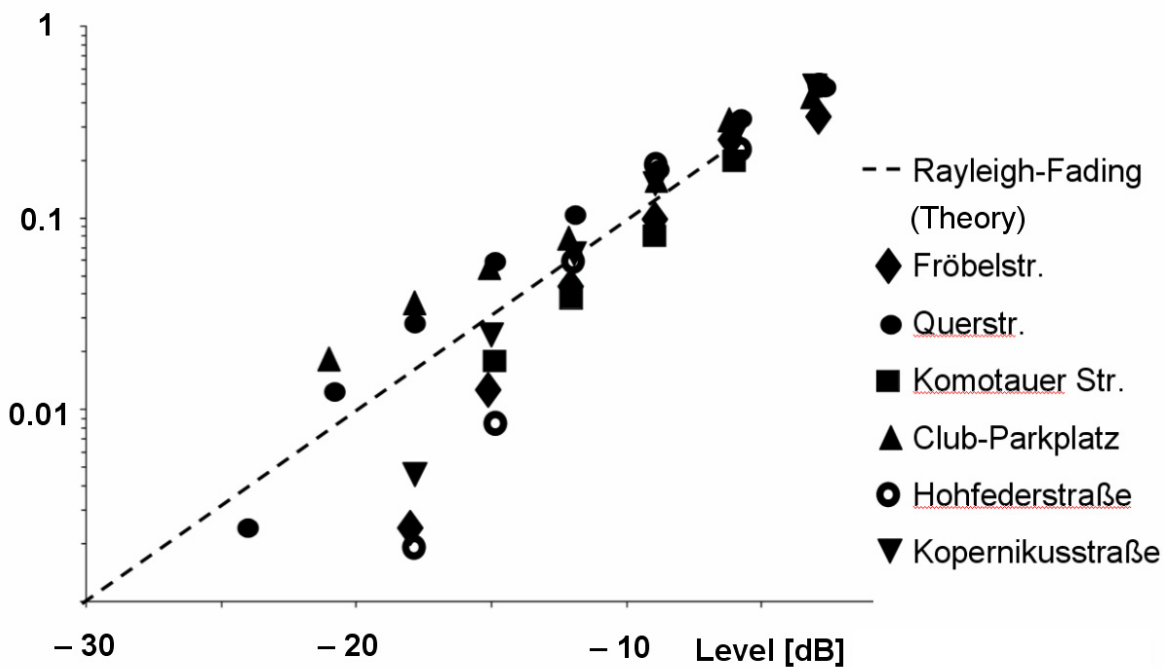
Fig. 5: Result of statistical analysis (Rayleigh-plot) showing that Rayleigh fading can in most cases be assumed to cause the fading observed in measurements of receiver input power [12].

Stationary Reception

The transmissions from both transmitter sites were monitored at the home of the author in a suburb of Nuremberg (Altenfurt, see Fig. 8) at about 8 km distance from Nuremberg transmitter and at about 18 km from Dillberg transmitter for several periods of time during March 2003 – August 2005. A number of voluntary persons, in particular students of our Fachhochschule who were equipped with receivers and radio amateurs joined these monitoring efforts to achieve parallel reception at different sites during several days.
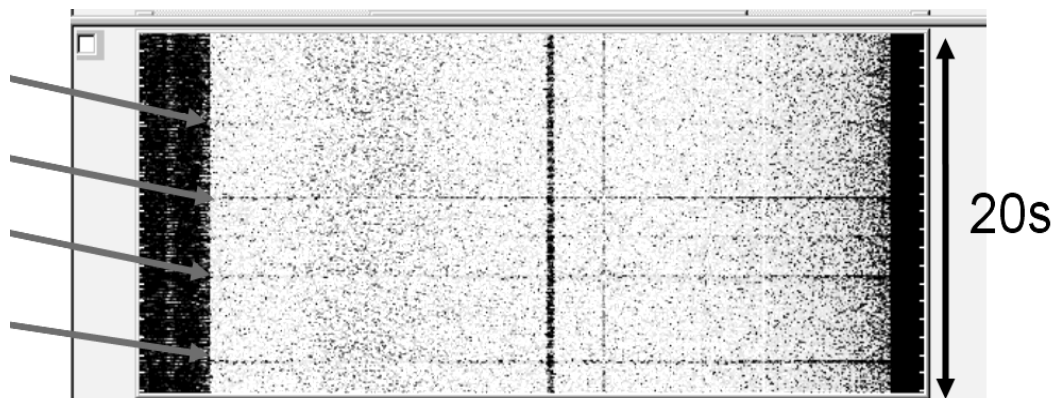
Fig. 6: Waterfall diagram of received signal along a route of 20 s in Fröbelstraße indicating that the fading of the signal is not frequency selective but flat.

A number of observations were made which concern the reliability of reception in the 26 MHz broadcasting band which are summarised here. The main mechanisms that lead to reception impairment are:

- Interference from FM radio from eastern Europe, when long distance propagation is possible
- Local sources of interference, e.g. man − made − noise.

To separate both mechanisms we compared the results (SNR and percentage of correctly decoded audio frames) of simultaneous recordings of reception at different sites.

Fig.7 shows an example of such a set of recordings. During the whole day of January 10th, 2004, the Nuremberg transmitter was received at four different sites at different distances from the transmitter (Wöhrd: 0.5 km, Meistersingerhalle: 1.5 km; Stein: 8 km, Altenfurt: 8 km). While reception close to the transmitter (Wöhrd) was unimpaired all over the time, reception at the other sites suffered from interference from about 9 to 13 UTC. It was found that this interference is caused by signals from remote transmitters, probably from an FM radio network operating in Eastern Europe. The impairment due to the interfering signals is worse when the signal from the DRM transmitter is rather week (Meistersingerhalle, due to shadowing by buildings) and does not occur when the wanted signal is strong (Wöhrd, close to the transmitter) and the interfering signals are much weaker than the wanted signal. At Stein there is apparently also a local source of impairment which caused dropouts between 4 and 5 UTC, which were not observed at the other sites.

We performed such comparative measurements on ten days between January and May, 2004, on eight of which reception from both transmitters was studied at up to seven sites of reception. Basically, the findings for all were similar to those presented in Fig. 7. Depending on the season of the year we occasionally observed simultaneous interference from distant transmitters, however only during daytime, never during the night, but we always found uncorrelated impairments due to local sources of noise both at daytime and nighttime. We recorded reception parameters (SNR and availability of audio) for a total of 1434 hours (all sites summed up). We received unimpaired audio signals (100% availability) for a total of 1004 hours. For the remaining time, i.e. when interference occurred, the average audio availability was still 96.2%. Hence the average audio availability over the whole time and at all sites was 99.2%.

Another measurement campaign was performed in December 2004 and January 2005. The receiving sites for Dillberg transmitter are shown in Fig. 8, and a typical set of results is shown in Fig. 9.
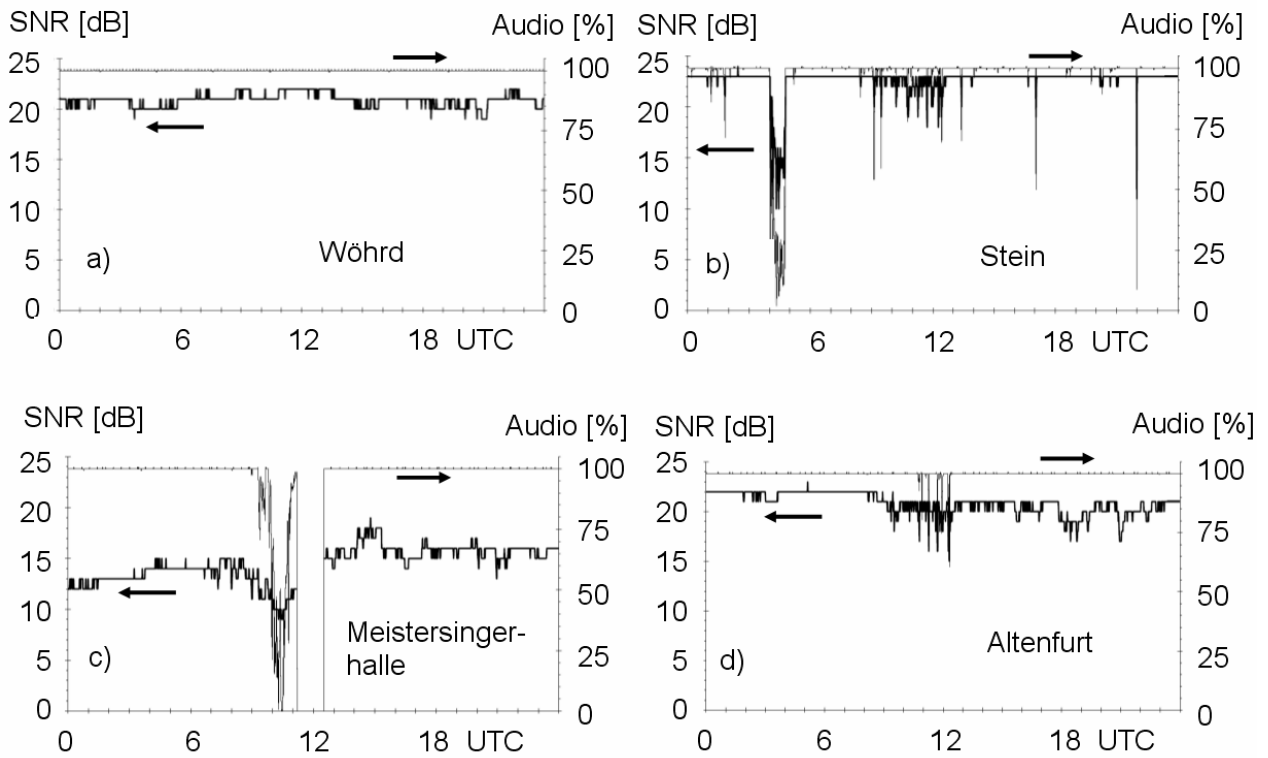
Fig. 7: Results of four recordings of the transmission from Nuremberg transmitter on January 10th, 2004 [12].
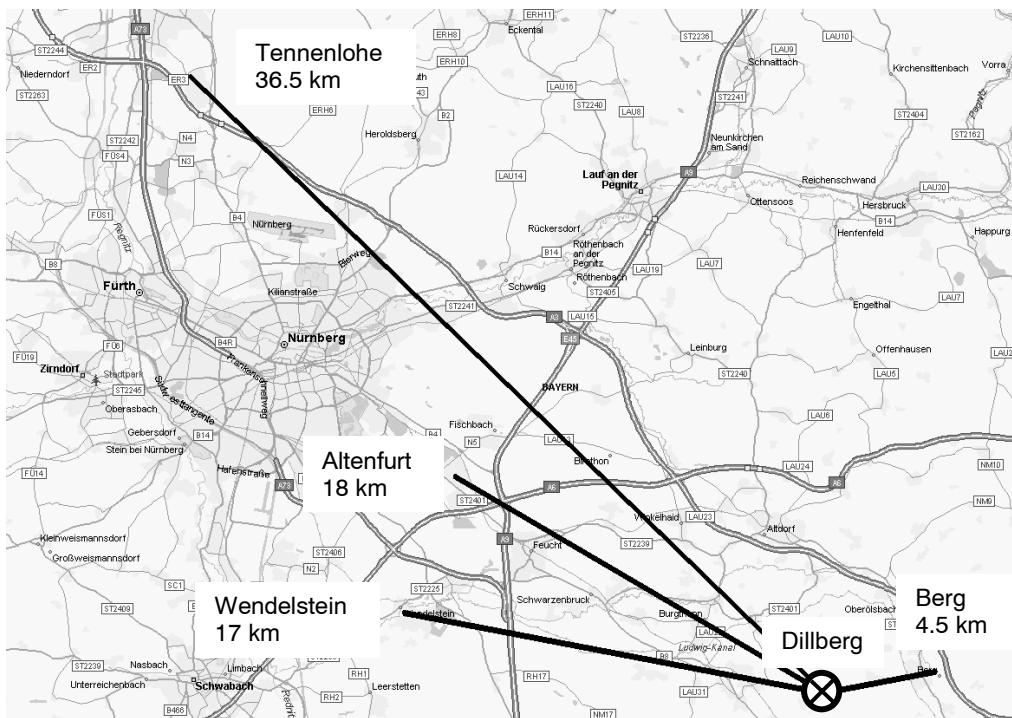
Fig. 8: Location of receivers and their distances from Dillberg transmitter during the measurement campaign in December 2004 – January 2005
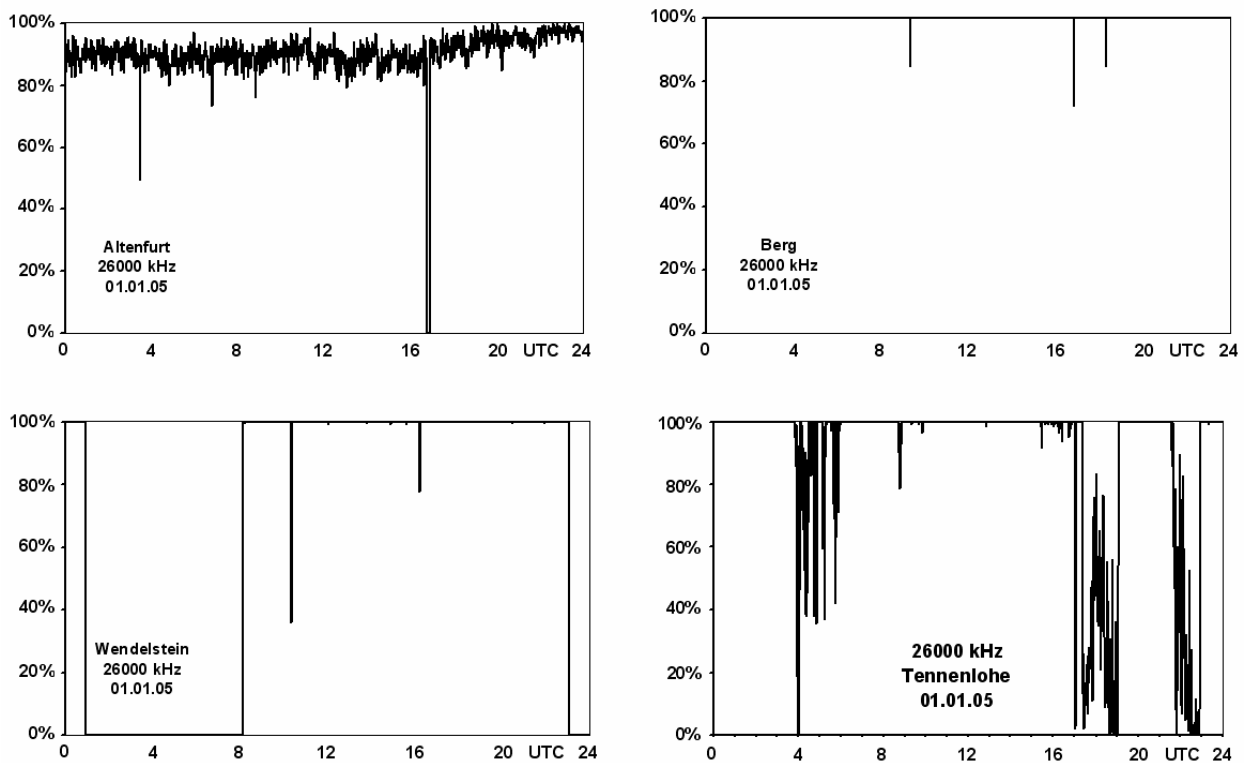
Fig. 9: Typical results of audio availability from Dillberg transmitter during December 2004 – January 2005

Again we notice that most of the reception problems are due to local interference, in particular at Altenfurt and Tennenlohe. At Tennenlohe, where the receiver was placed in an industrial zone, the impairments occurred on all days at the same time and were probably caused by some electrical applicance which is always operated at the same time of the day.

From December 2004 to July 2005 we performed long term recordings of reception from both transmitters, again at Altenfurt. The respective results are presented in Table 2. Concerning the rather low values in January and February 2005 we observed that this was due to a local source of noise at Altenfurt, similar to the pattern shown in the Altenfurt part of Fig. 9, while reception at other sites was unimpaired.

It is interesting to note that the result from June 2005 is quite low although the local source of noise leading to the low values during January to March was usually not present at that time (Fig. 11a). However, sporadic E layers in the ionosphere frequently occur in the northern temperate zones during May to July leading to interference from distant sources. To proof that the impairment was non-local, again receivers at two locations (Altenfurt and Stirn, about 40 km south of Altenfurt) were operated simultaneously for two weeks in May 2005. Fig 10 shows the results from two days – one without presence of sporadic E (Figs. 10 a) and c)), the other where impairments were observed at both locations at the same time attributed to the occurrence of a sporadic E layer (Figs. 10 b and d).

During summer 2004 and 2005 we also received a number of reception reports for the Dillberg transmitter from short wave listeners from several European countries (Fig. 11 a). We ourselves could receive a DRM transmission from Rennes on 25775 kHz several times with SNR good enough for audio decoding (Fig. 11 b). This also shows the relevance of sporadic E layer propagation at this frequency range.

Table 2. Results of long term recording of reception parameters at Altenfurt.

Month	Nuremberg Transmitter		Dillberg Transmitter	
	Total time of recording (hours)	Audio availability	Total time of recording (hours)	Audio availability
December 2004	239	99.9%	315	97.6%
January 2005	315	98.6%	455	91.3%
February 2005	–	–	558	90.6%
March 2005	–	–	354	92.9%
April 2005	–	–	497	99.5%
May 2005	–	–	605	97.3%
June 2005	–	–	427	93.9%
July 2005	206	99.6%	381	97.0%
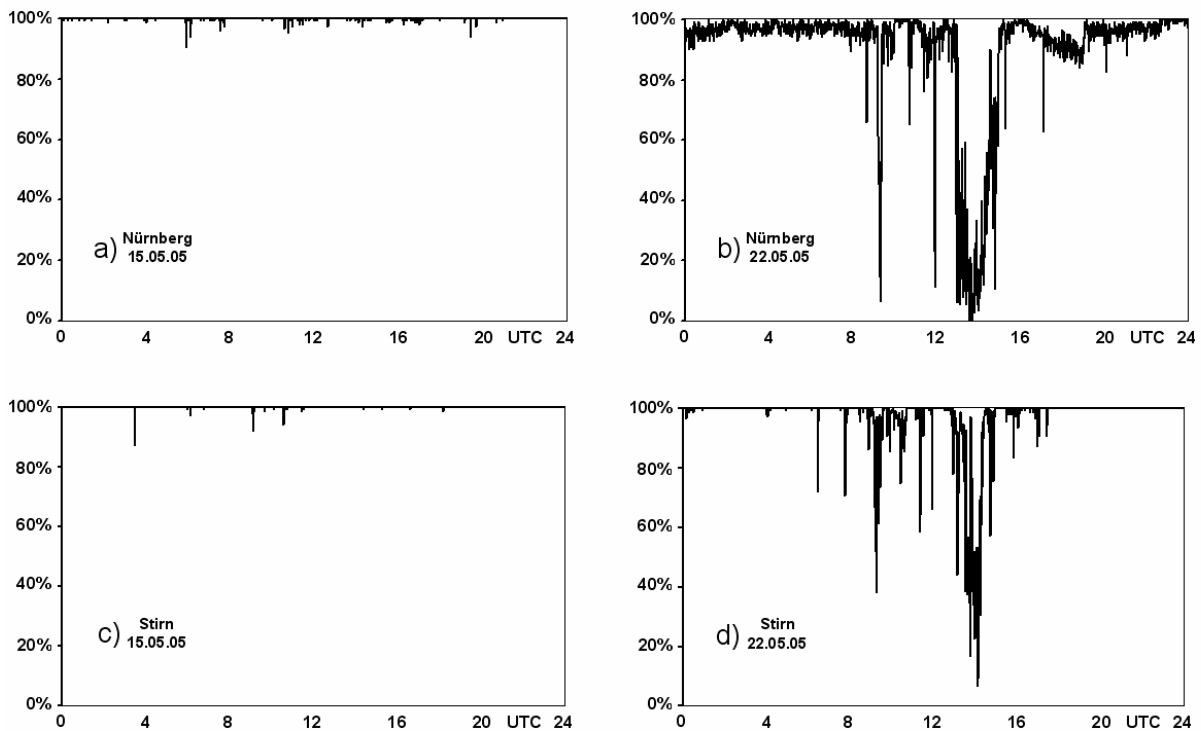
Fig. 10: Audio availability from Dillberg transmitter at two receiving sites on two days during the sporadic E season in May 2005.
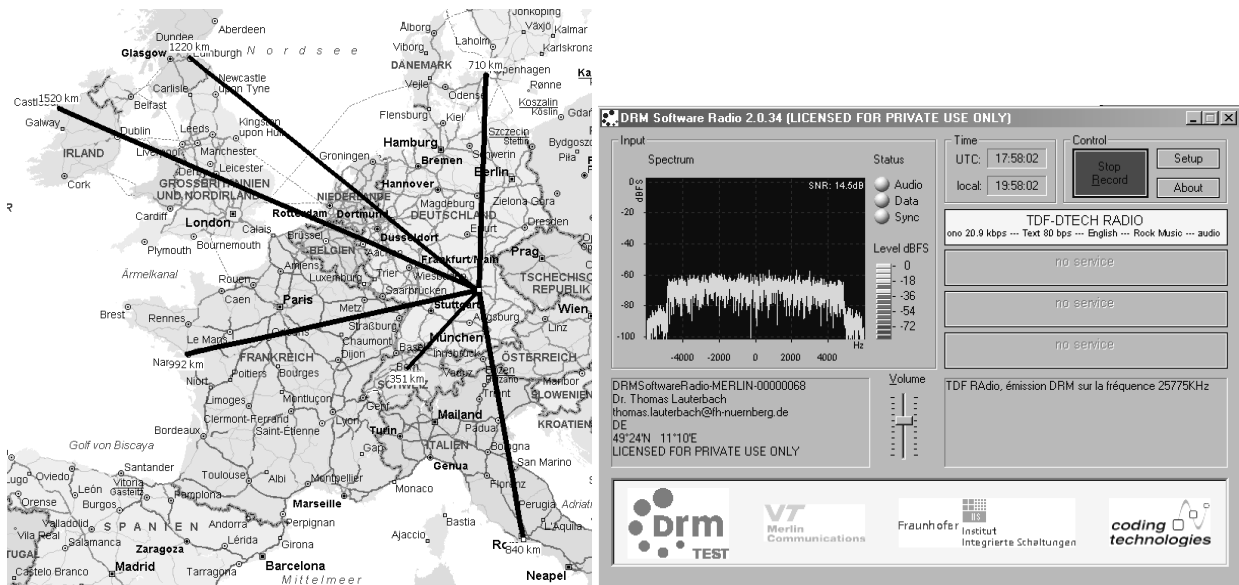
Fig. 11: a) sites from which reception reports for the Dillberg transmitter were received during Summer 2004 and Summer 2005. b) Screenshot of reception of a DRM transmission from Rennes in Nuremberg (distance: 950 km) on June 27th, 2004.

Considerations for planning local services in the 26 MHz band
Planning the service area

The results from our field tests suggest that local sound broadcasting services may well be operated in the 26 MHz shortwave band. For planning the service area of such stations, the same method as for planning VHF networks may be used, because the useful service area will be determined by direct propagation from the transmitter site to the receivers. Propagation conditions do not seem to be very different from the VHF range, in particular with respect to shadowing by terrain and buildings and reflections leading to multipath propagation.

The measurements of field strength that have been carried out in the Nuremberg and Dillberg area by Deutsche Welle [10] support this view. It was found by them that a minimum field strength of 23 dbµV/m was required for appropriate audio decoding. The range for uninterrupted mobile reception of the Dillberg transmitter was found to be 15-20 km (Fig. 2). This is consistent with the VHF prediction curves of ITU-R Rec. 370 [13]: for a 1 kW transmitter with an antenna height of 150 m (this corresponds well to the Dillberg situation because the antenna is at 605 m a.s.l. while the surrounding terrain is at approximately 350 $-$ 400 m a.s.l.) the predicted field strength at 20 km distance for 50% of locations and 50% of time is 63 dBµV/m. Since the transmitter only uses 100 W, this value must be reduced to 53 dBµV/m. Because reception is uninterrupted at this distance from the transmitter, we must consider a location probability of 99%, which means that the predicted value must be reduced by another 18 dB, resulting in 35 dB µV/m. This predicted value however is an aerial 10 m above ground level at the receiving site. At car antenna level, i.e. 1.5 m above ground, the field strength is expected to be lower by approximately 13 dB [13], which leads to 22 dBµV/m, in good agreement with the measured values.

Mobile reception

If a service, however, is to be received by mobile and portable receivers, the flat fading conditions of the 26 MHz multipath channel would lead to audio dropouts at certain spots. This may be relevant in particular for mobile and portable receivers at low speed, e.g. radios in cars in traffic jams or stopping at traffic lights and for portable receivers, i.e. in situations where time interleaving does not improve reception due to the slow time variance of the channel. It is important to remember that the DRM system is not designed to operate in such channels. Therefore these dropouts cannot be avoided by increasing power or other measures. However, reception may improve in single frequency networks when receivers receive uncorrelated signals from at least two transmitters.

Planning to avoid interference

In contrast to VHF, where the same prediction curves may be used for planning the service area and the field strength caused by potential co-channel interferers, long distance propagation issues related to ionospheric F layer and sporadic E layer scattering must also be considered for planning in the 26 MHz band in order to prevent mutual interference of such services.

F layer propagation

The most relevant phenomenon for long distance propagation in the short wave range is scattering from the F layers of the ionosphere. These layers are approximately 300 km above the surface and show critical frequencies f_0 (i.e. the highest frequency which is scattered back from the ionosphere at vertical incidence) of typically several megahertz. The highest frequency which is scattered back from the ionospheric layers at the flattest angle of incidence is referred to as the maximum usable frequency (MUF). The relation between the critical frequency and the MUF is given by

$$f_{MUF} = \frac{f_0}{\sqrt{1 - \left(\dfrac{\cos\varphi}{1 + h/r_E}\right)^2}}$$

In this equation, h is the (virtual) height of the ionosperic layer (300 – 400 km in case of the F layer), r_E is the radius of the earth and φ is the angle at which the wave is radiated from the ground. The highest value of f_{MUF} is obtained for $\varphi = 0$, i.e. for a wave radiated towards the horizon. In this case the MUF will be about 3.4 times as high as the critical frequency. Hence a 26 MHz wave will be scattered back from the ionosphere when the critical frequency of the F layer is above about 8 MHz. The critical frequency of the F layer depends on the time of the day, the season and the solar activity. A median value of 8 MHz is well exceeded during the winter season and during day time in the years of the sunspot maximum, because this value for f_0 correlates to a sunspot number (gliding average) of R ≈ 80. In a particular sunspot cycle, for instance, a value of 80 of the sunspot number was exceeded from January, 1956 to January, 1961, i.e. for five years (Fig. 12). During this period of time, which is periodic every 11 years, long distance propagation in the 11 m shortwave band will occur especially in directions where the whole path is on the day side of the earth. Due to the lower angle of incidence of the solar rays on the ionosphere the critical frequency and hence the MUF is higher in winter. Therefore, excellent long distance propagation will occur along the day paths in winter, for instance from Europe to the U.S. during the afternoon in Europe (morning in the US) and from Europe to the far east during the morning in Europe. During the summer, long distance propagation will be possible on transequatorial paths, e.g. from Europe to South Africa and South America. It should be noted that during the relevant period the sunspot number is not constant nor is f_0F_2. For well established local radio with many stations operating in this band world-wide, however, interference from co-channel stations would be probable in particular on winter days during the years near the sunspot maximum.
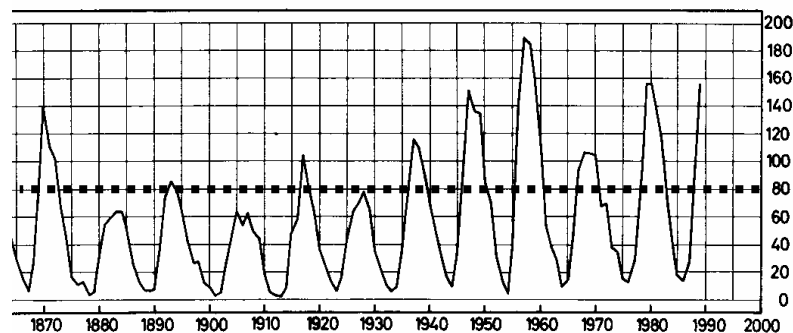
Fig. 12: Sunspot relative numbers R [14]. For R > 80, F layer propagation at 26 MHz is possible.

A propagation prediction was performed to find out under which conditions mutual interference from local radio stations using the same channel in the 26 MHz band would occur. The relevant criterion is that impairment will occur if the field strength of the interferer is higher than around 0 dBμV/m assuming that the minimum field strength of the wanted signal is higher than 20 dBμV/m and a minimum signal to interference ratio of 20 dB is sufficient to suppress any audible impairment.

The simulations were performed using the software "Funk – Prognose Version 3.3.2" by Uwe Runte. This software generates maps of field strength values of a given transmitter which are predicted to be exceeded for 50% of time. The following parameters were used: Transmitter location: Munich, Germany, E.I.R.P. 1 kW, vertical angle of radiation 10°, corresponding to the vertical pattern of a vertical half-wave antenna at 10 m above ground. The simulation were performed for different values of the sunspot relative number (150, 100, 50, 15), different times of the day (0.00, 4.00, 8.00, 12.00, 16.00, 20.00 UTC) and different seasons (January, April, July, October). A single result of such a simulation is shown in Fig. 14.

It can be seen from this example, but also from the results of all simulations that only in the area where the transmitted wave hits the ground after a single ionospheric hop a field strength high enough to generate interference is to be expected.

The results of all simulations are summarised in Table 3 which shows under which conditions mutual interference would occur if transmitters at arbitrary distance are operated on the same channel. It is evident that even when sunspot numbers are rather low interference would occur for some hours of the day. This is in good agreement with our experimental observations regarding interference from eastern European radio communications which occurred even at sunspot numbers as low as 34 and 26 [8].

Therefore, co-channel transmitters should not be located at distances of about 1500 − 2500 kilometres if mutual interference is to be avoided.
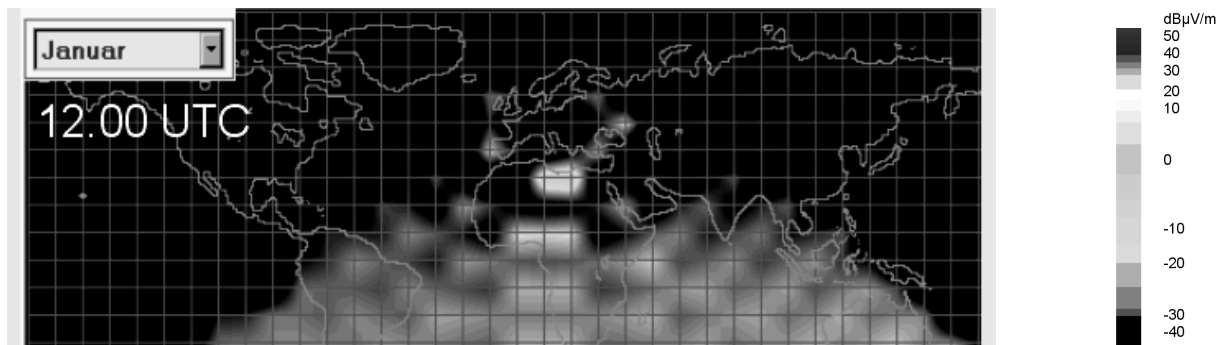
Fig. 13: Example result of a prediction of field strenght of a 1 kW transmitter operated from Munich, Germany. R = 50 (maximum of sunspot cycle).

Table 3: Conditions under which mutual interference of transmitters operating in the 26 MHz range is to be expected (Central Europe).

UTC	January						April						July						October					
	0	4	8	12	16	20	0	4	8	12	16	20	0	4	8	12	16	20	0	4	8	12	16	20
R=150			■	■	■				■	■	■	■			■	■					■	■	■	
R=100				■					■	■	■					■					■	■	■	
R=50										■	■												■	
R=15																								

Sporadic E Layer propagation

The E layer of the ionosphere is normally only relevant for frequencies below about 10 MHz. However, especially during summer, highly ionised spots in the E layer, called sporadic E layers, occur. Their critical frequencies are above 7 MHz for 5% of the time and above 9 MHz for 1 % of the time in northern termperate zones during May to August, 8[h]-23[h] local time [15]. In contrast to F layer propagation, sporadic E layer propagation will also occur during periods of lower solar activity.

Statistical data concerning the frequency of occurrence of sporadic E layers in different zones of the world and a method for calculating the field strength are given in [15]. From the data provided there, we calculated the field strength that a co-channel interferer would generate during the occurrence of sporadic E propagation. The result is shown in Fig. 14. Field strength that would cause interference may be reached at distances from 400 to 2000 km, and at the same distances even reception of the signal should be possible. Again our experimental observations and reception reports for our transmissions support this result (see Figs. 11 and 12). If this type of interference is to be avoided, co-channel transmitters should not be placed at distances between 400 km and 2000 km if interference should not occur for more than 1% of the time during summer (May – August in the northern temperate zones). It should be noted, however, that this prediction is for a single pair of transmitters. If there are several transmitters at the same distance from the wanted one but in different directions, the occurrence of sporadic E layers will not be correlated and hence the probabilities for their occurrence have to be added up. Thus interference will be more frequent.
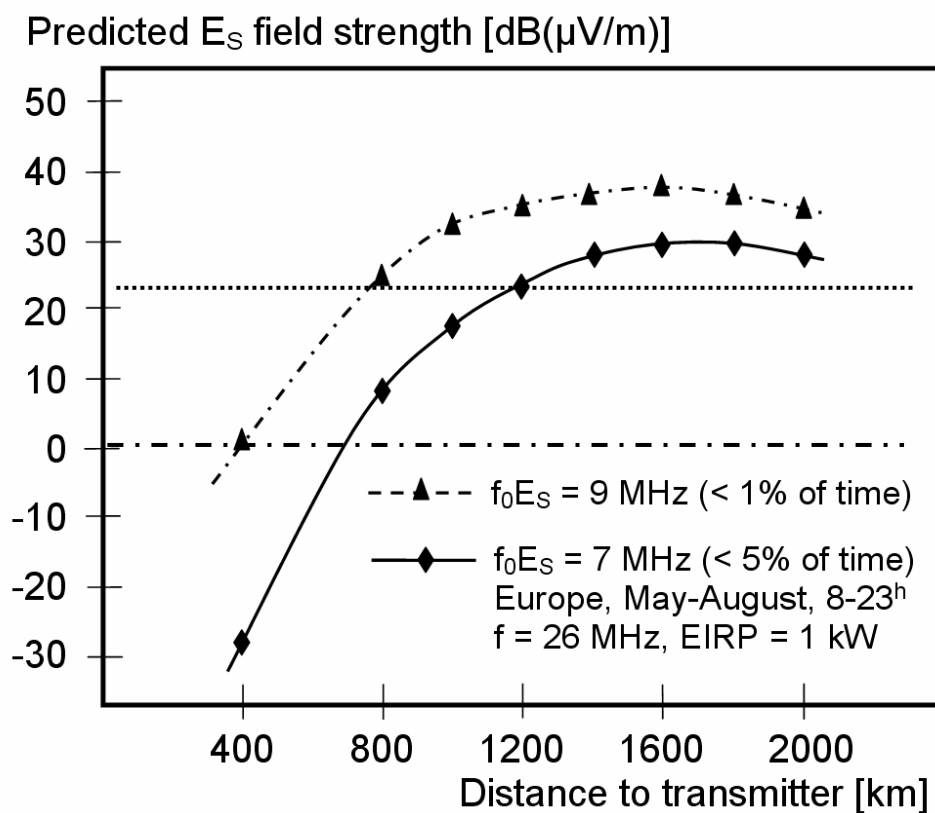
Fig. 14: Predicted field strength according to [15] for propagation via sporadic E layers for 1 kW transmitters operating on 26 MHz. Thresholds for interfernce (0 dBμV/m) and reception (23 dBμV/m) are indicated.

Conclusions from propagation issues and development of a planning scenario

From the properties of ionospheric propagation reviewed above it must be concluded that if the 26 MHz short wave band were widely used for local broadcasting without international channel assignment, a situation would arise where during daytime in the years around the sunspot maximum a number of co-channel stations at distances of up to several thousands of kilometres would generate a significant level of interfering field strength. The coverage area of the wanted transmitter would then shrink dramatically. In summer, due to sporadic E propagation, there will be additional interference from stations nearby (as close as 400 km) even in the years of the sunspot minimum.

Therefore a careful planning method is required. A safe recipe seems to be not to place co-channel stations at distances from 400 km to 2500 km to each other. An example for this is given in Fig. 15. In each

of the dark spots with diameters of approximately 400 km the same channel could be used. However, in a large area around each transmitter the same channel should not be used if mutual interference is to be excluded. Since the 26 MHz band only has a bandwidth of 430 kHz, there are only 43 channels in total. To reasonably fill the diamond-shaped area between four adjacent areas where the same channel can be used, a number of 57 channels would be needed (Fig. 16). Therefore some additional channels would be required e.g. in the 21 MHz band (13 m − Band) for which similar propagation conditions can be envisaged, or the assignment of a wider frequency range in the 26 MHz band would be required. Even if this can be achieved, it would mean that in each area only a single channel would be available for local broadcasting. If more channels are required in one area, they must be taken from the surrounding areas or mutual interference with other services at least during some time must be accepted.

It should be noted however that the problems caused by mutual interference from distant stations are complementary on medium wave and in the 26 MHz band. Therefore a solution for local broadcasting in the bands below 30 MHz could be to switch frequencies twice a day using a 26 MHz frequency during night time and a medium wave frequency during day time. Then many more channels would be available. Future DRM receivers are expected to be able to seamlessly follow such a switch with no interruption of audio output, because it can be signalled in advance and the same DRM parameters could be used (e.g. DRM mode A with 9 kHz bandwidth), because the service on short wave will also rely on ground wave propagation. The proper time to switch can either be derived from propagation predictions or using monitoring receivers at the fringe of the desired coverage area. However the cost of operating such a dual transmitter site will be significantly higher than that of a single station.

Fig. 15: Example of areas with diameters of 400 km each (dark spots) where the same channel in the 26 MHz could be used. The spacing between these areas is 2900 km to guarantee a minimum distance of 2500 km between co-channel transmitters which the predictions suggest is sufficient to avoid mutual interference.
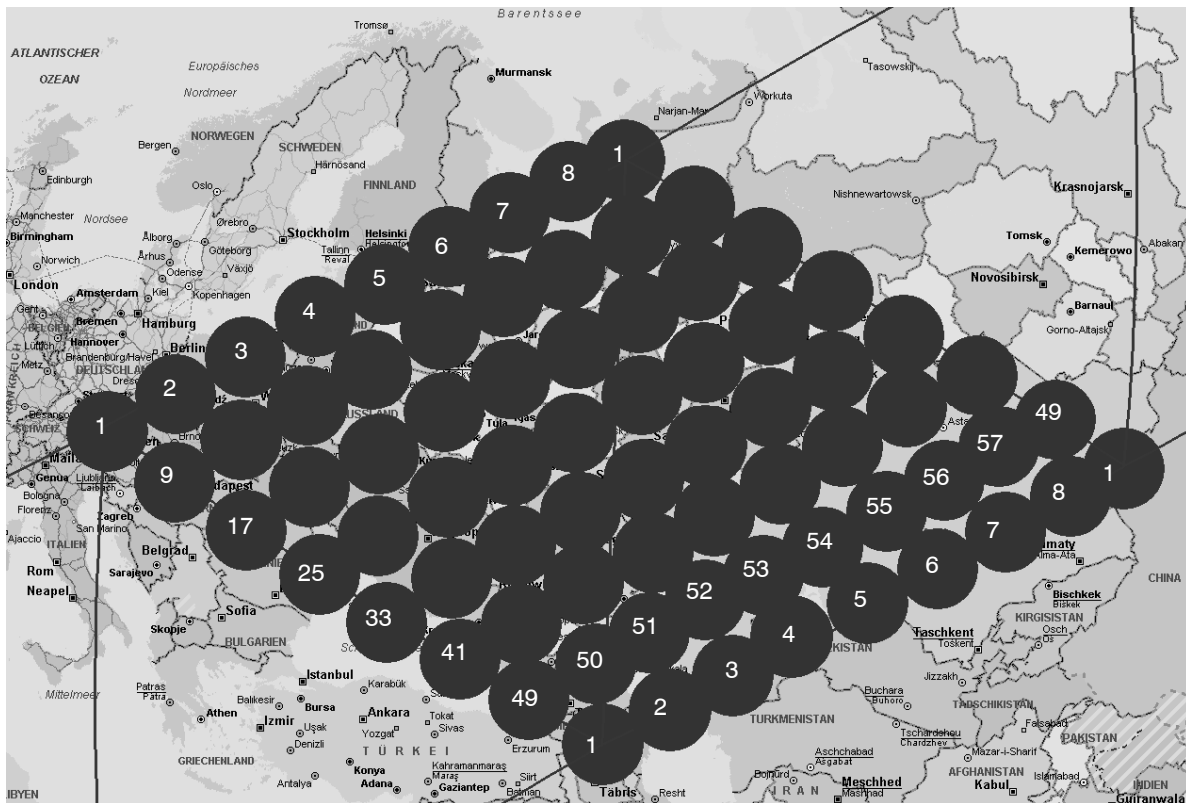
Fig. 16: Example of how the diamond-shaped areas between adjacent spots using the same channel could be filled using other channels. However, the 57 channels which would be needed are not available in the 26 MHz band.

Conclusions

From the results from our field trial and the considerations regarding a planning model, the following conclusions with respect to local broadcasting in the 26 MHz band using DRM can be drawn:

- Low power DRM transmitters including transmission antennas can easily be set up and operated and do not require great financial resources.
- The coverage area of such transmitters (operating at 100 W E.I.R.P. at an appropriate site) will be up to 20 km for mobile reception and up to 50 km for fixed reception using rooftop antennas.
- Portable and mobile reception at the fringe of the service area will suffer from flat fading due to multipath propagation, at least in cities.
- The sound quality that can be achieved will be sufficient for most audio material typically sent by local stations, although only an audio bandwidth of approximately 11 kHz can be expected.
- Indoor reception is frequently limited by man-made-noise which may occur for an unpredictable amount of time depending on the electromagnetic environment of the receiving site.
- Due to the propagation conditions in the 26 MHz frequency range attention must be paid to the fact that even when low transmitter powers are used co-channel interference will be frequent both during the time of the sunspot maximum and in summer when sporadic E layer propagation will frequently occur. Therefore either the reliability of services will be limited or only one channel will be available in each region of about 400 km in diameter. International coordination of channel assignment will be required in this case.
- A possible remedy to the problems caused by long distance propagation could be to use the 26 MHz band only during night time and use a medium wave frequency during day time.

Based on these findings we believe that widespread use of the 26 MHz band for local broadcasting can only be recommended for services which are well aware of and can tolerate the severe limitations to the reliability of reception quality which cannot be avoided when operating in this frequency range. For other

services the use of the envisaged DRM plus system in the VHF broadcasting bands will be better suited to their demands of quality of service.

Acknowledgements

References

[1]   Titze, Wolfram, Gerald Chouinard, Stephen Baily, The Broadcast Side. In: Wolfgang Hoeg, Thomas Lauterbach (Eds.), Digital Audio Broadcasting – principles and applications of digital radio. 2nd. edition, J. Wiley and Sons, Chichester 2003

[2]   ETSI, ETS 201 980, Digital Radio Mondiale (DRM); System Specification.

[3]   DRM Broadcasters' User Manual, DRM Consortium, 2004 (available as pdf at http://www.drm.org)

[4]   Stott, J., Digital Radio Mondiale: key technical features, Electronics & Communication Engineering Journal. February 2002, p.4;

[5]   Dietz, M. and S. Meltzer, CT–aacPlus — a state–of–the–art Audio coding scheme, EBU Technical Review July 2002, p. 7

[6]   Hofmann, F., Ch. Hansen, and W. Schäfer, Digital Radio Mondiale (DRM) Digital Sound Broadcasting in the AM Bands, IEEE Transactions on Broadcasting, Vol. 49, No. 3, September 2003, p. 319

[7]   Richter, Michael, Michael Thiele, Digitale Mittelwelle 531 digital, Schriftenreihe der Medienanstalt Sachsen– Anhalt, Band 5, Vistas–Verlag, Berlin 2004

[8]   Lauterbach, Thomas, Benjamin Kreuzer, Reinhard Zitzmann, Konrad Blomeier, Is DRM on 26 MHz an Option for Local Digital Broadcasting? Results from a Field Trial in Nuremberg, Germany. Fraunhofer IIS 5th Workshop Digitaler Rundfunk, Erlangen, 23./24.9.04

[9]   http://www.ai.fh-nuernberg.de/professors/lauterbach/lauterb.html

[10] Widdau, Stefan, Frank Held, Deutsche Welle, private communication, June 2004

[11] Rec. ITU–R BS.1615

[12] Blomeier, Konrad, Untersuchung zur digitalen Lokalrundfunkversorgung mit Sendern kleiner Leistung im Kurz- wellenbereich, Diploma thesis, Georg–Simon–Ohm–Fachhochschule Nürnberg, June 2004

[13] Vogelsang, Erich, Wellenausbreitung in der Funktechnik, R. Oldenburg Verlag München 1979

[14] Lexikon der Astronomie, Spektrum akademischer Verlag Heidelberg 1995, Bd. 2, S. 248

[15] Rec. ITU–R P.534–4, Method for calculating sporadic – E field strength.

Potential of porous medium combustion technology as applied to internal combustion engines

Prof.Dr.-Ing. Miroslaw Weclas

Institut für Fahrzeugtechnik
Georg-Simon-Ohm-Fachhochschule Nürnberg
Keßlerplatz 12
D-90489 Nürnberg

Abstract

The paper describes application of a highly porous open cell structures to internal combustion engines for supporting mixture formation and combustion processes. Porous structures, materials and their properties for engine application are discussed in this paper. Especially application to a high temperature combustion processes are considered.

Novel concepts for internal combustion engines based on the application of porous medium technology are presented and discussed. The main attention is focused on the engine concepts having potential for homogeneous (nerly emissions free) combustion process under variable engine operational conditions. It is shown that porous media can be used for a great variety of improvements in the combustion process. The key role for NOx reduction and soot emission ellimination is a homogeneous combustion in engine. This can be realised by homogeneous mixture formation, and a 3D ignition preventing from formation of a flame front having a temperature gradient a in the entire combustion volume. All these processes: gas flow, fuel injection and its spatial distribution, vaporization, mixture homogenization, ignition and combustion can be controlled or positively influenced with the help of porous media/ceramic reactors.

1. Actual problems of mixture formation and combustion in internal combustion engines

Future internal combustion (IC) engine will be characterized by a (nearly-) zero emissions level (for both gaseous and particulate matter components) under possible lowest fuel consumption permitted at all operational conditions. This may be achieved by realization of homogeneous combustion process in engine.

An internal combustion engine (especially for road vehicle application) has to operate in a wide range of loads and speeds. From the point of view of reduction of combustion emissions and fuel consumption, especially attractive would be application of lean homogeneous charges for operation at engine part loads.

There are different technologies available for reduction of engine emissions (e.g. electronically controlled high pressure injection systems, variable valve controlling, EGR, etc), however, a simple combination of them **does not** automatically solve the problem of engine emissions under all operational conditions. In author opinion, however, these technologies may be utilized in new concepts for mixture formation and combustion that are necessary to be created in the nearest future for "clean reciprocating engine".

While future IC engines require low specific fuel consumption under (near-) zero combustion emissions level, it will be necessary to significantly change a primary combustion process in conventional engines, e.g. *by application of porous medium technology*. New approaches using porous medium (PM) technology are described in this paper.

2. Porous medium technology

2.1. Introduction to porous medium technology

In this paper a highly porous structures having open cells are considered, with porosity higher than 80%, and typically higher than 90%. This makes the porous media transparent for gas flow, spray and flame (Fig.1).

Porous medium (PM) technology is here defined as an utilization of specific and unique features of highly porous medium for supporting of individual processes (mixture formation, ignition and combustion) realized in engine (see Fig.2) [1, 2]. Most of these processes perform in PM-volume

drastically different manner from this observed in a free volume.
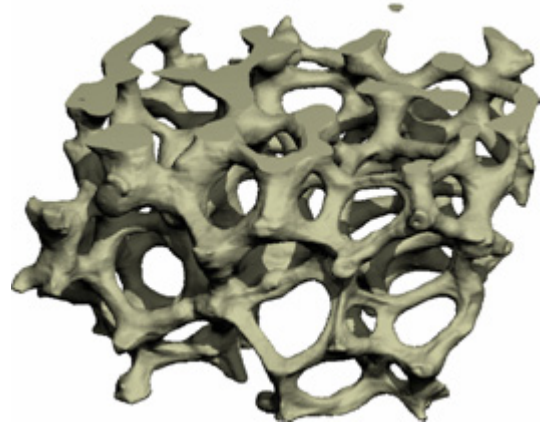
Figure 1: Reconstructed 3D-structure of SiC foam on the basis of computer tomography (10mm x 10mm x 10mm probe)

Selected features of the porous medium permit its attractive application to the following engine processes:

- Energy recirculation in engine cycle in the form of hot burned gases recirculation or combustion energy: this may significantly influence thermodynamic properties of the charge in the cylinder and may control the ignitability (activity) of the charge. This energy recirculation may be performed under different pressure and temperature conditions during the engine cycle. Additionally, this heat recuperation may be used for controlling the combustion temperature level.
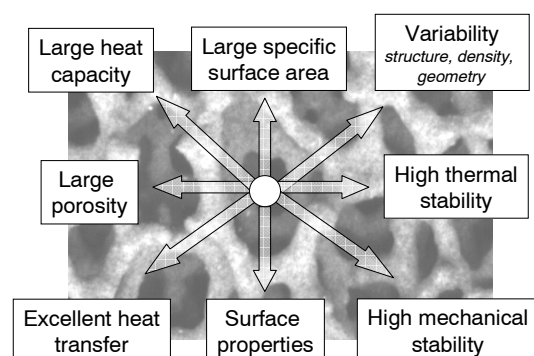
Figure 2: Main features of porous structures to be utilized to support engine processes

- Fuel injection in PM-volume: especially unique features of liquid jet distribution and homogenization throughout the PM-volume (effect of multi-jet splitting) [3] is very attractive for fast mixture formation in the PM-volume.

- Fuel vaporization in PM-volume: combination of large heat capacity of the PM-material, large specific surface area with excellent heat transfer in PM-volume make the liquid fuel vaporization very fast and complete. Here two different conditions of the process have to be considered: vaporization with presence and with lack of oxygen.

- Mixing and homogenization in PM-volume: unique features of the flow properties inside 3D-structures allow very effective mixing and homogenization in PM-volume.

- 3D-thermal-PM-ignition (if PM temperature is at least equal to ignition temperature under certain thermodynamic properties and mixture composition): there is a new kind of ignition, especially effective if the PM-volume creates automatically the combustion chamber volume [4, 5].

- Heat release in PM-volume under controlled combustion temperature (properties of homogeneous combustion): there is only one known kind of combustion, that permits homogeneous combustion conditions almost independently of the engine load with possibility of controlling of the combustion temperature level [4, 5].

Depending on the application of a porous medium, a combination of thermal and mechanical properties of the materials as well as their inner structure and pores size have to separately be chosen and optimized for supporting of particular engine process. If the porous medium is used directly for controlling the combustion process under high pressure conditions, above requirements become especially critical. The probe presented in figure 1 is characterized by the following parameters: porosity=91,88%, connection density =0.0311 per mm^3 (represents a number of connections or junctions per cubic millimetre) - see Fig. 3. For applications considered in this paper typical pore size is higher than 1mm, and usually is of order of 3mm large. This pore size is often expressed by the pore density "ppi" − pore per linear inch. Typical pore density useful for applications reported in this paper is from 8 to 30ppi. The pore shape and pore density depends on the basic foam used for manufacturing of final foams (e.g. PU-foam for ceramic foams).
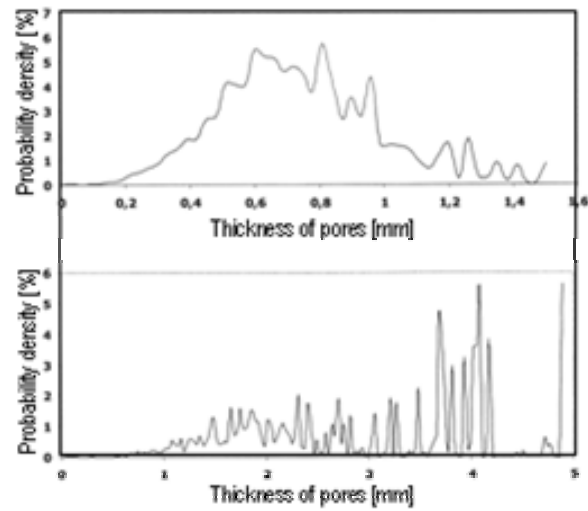
Figure 3: Thickness distribution of pore walls (top) and of pore size (bottom) of the SiC foam of figure 1.

The volume of a highly porous structure may be divided in to pore volume (free volume for gas), material volume, hollow tube junctions, and micro-porosity (Fig. 4).
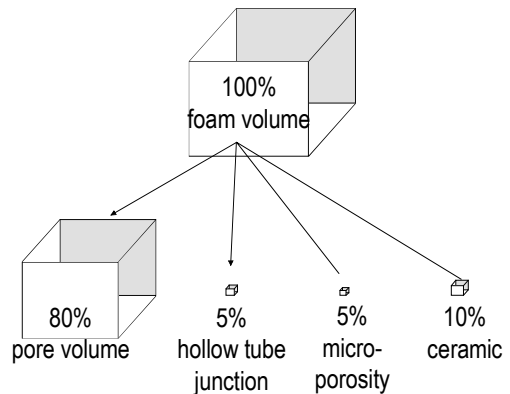
Figure 4: Volume share of highly porous structure

Typical foam structure of 10ppi pore density as compared to 1 Euro cent coin is shown in Figure 5.

Figure 5: 10ppi metal foam as compared to a one Euro cent coin

This high porosity of the porous material significantly influences the density of the structure.
In Figure 6 are compared densities of steel, SiC-ceramic and SiC-foam. Additionally, this figure shows the effect of pore density on the specific surface area.
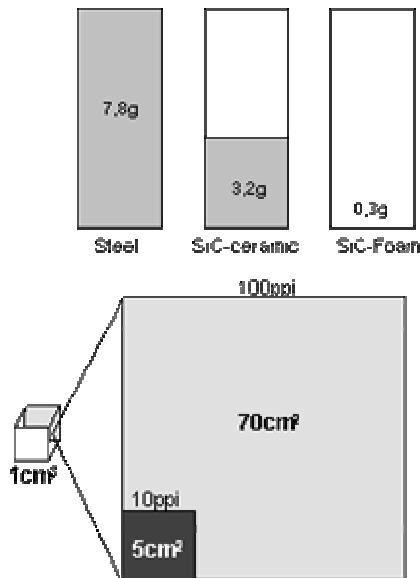
Figure 6: Density (top) and specific surface area (bottom) of highly porous 3D-structure

More imagination on the pore density and corresponding pore size for ceramic foam (SiC) is given in Figure 7.
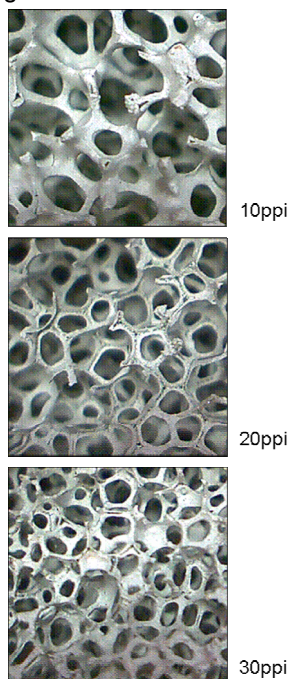
Figure 7: Examples of different pore densities for SiC foam

The variability of structures, materials and pores size is shown in figure 8, where ceramic foam structure, static mixer as well as wire packing are presented.
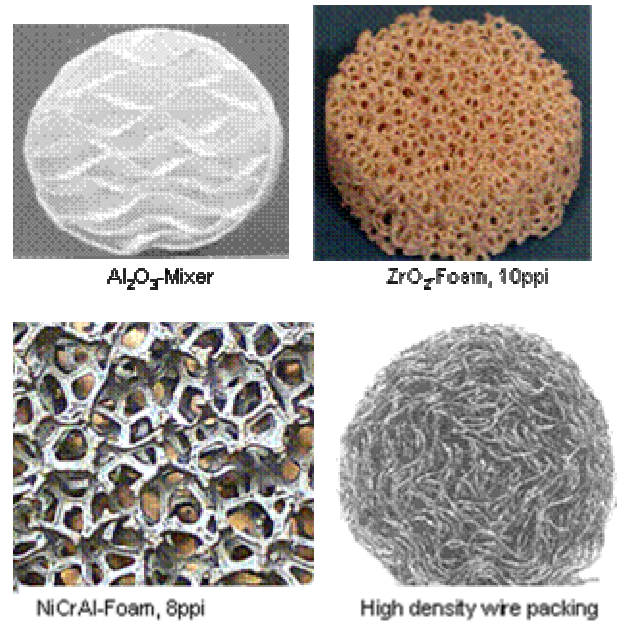
Figure 8: Examples of different porous structures

2.2. Selection of available PM materials and their features in application to engine processes

As already indicated in this section, there are number of important parameters that have to be considered in selection of PM materials for application to combustion processes realized in porous media. On one hand side, features of PM that are directly related to the heat transfer and combustion process are very important, e.g. specific surface area, heat transport properties, heat capacity and transparency for fluid flow and flame propagation. On the other hand, the thermal resistance and the mechanical properties of PM structure under high pressures are important for particular applications (see Table 1). Another parameter which must also be considered is the pores structure. Generally, the most important parameters of PM for application to combustion technology in can be selected as follows:

- specific surface area
- heat transport properties
- heat capacity
- transparency for fluid flow and flame
- pores size, pores density and pores structure
- thermal resistance

- mechanical resistance and mechanical properties under heating-cooling conditions
- PM material surface properties.
- Electrical properties

Table 1: Basic features and requirements of porous materials in application to engines

Parameters	Range of values
	(required/expected)
Specific surface area	Large:
	must be adopted to particular application to support individual processes
Heat transport properties	Excellent:
	especially important for PM-engine concept and homogeneity of the combustion zone
Heat capacity	Large:
	Must be adopted to particular application. In case of PM-engine defines the engine dynamic properties and influences the cycle thermodynamics. Also influences cold-start conditions
Permeability to flow and flame propagation	High porosity:
	For gas or liquid flow more than 80% porosity; preferably more than 90% porosity with open pores (cells). Pore size influences different processes in PM volume.
Pore size and size distribution	Typical pore density from 8ppi to 30ppi:
	For flame propagation under pressure see Pecklet number criterion. Directly influence pressure losses, multi-jet splitting by injection, homogenization in the volume
Pore shape	Principally all available shapes are suitable
	Cells must be open
Thermal shock resistance	High:
	Especially for PM-engine concept. Depending on the reactor location and art of montage in engine components
Corrosion resistance	High:
	especially in the atmosphere of burned gases
Electrical properties	For direct heating:
	high electrical resistance and homogeneous energy distribution (preferably voltage 12V and current 10 to 80A). Reachable temperatures are of 1500K. Could be important for cold-start conditions.
Available maximum temperature	Depends on the application:
	PM-engine concept T_{max} < 2000K; MDI concept T_{max} <1500K; Two-stage combustion concept T_{max} < 1800K
Porous medium mechanical stability	Important under high temperature and pressure conditions:
	Very critical factor in the case of ceramic material mounted in the piston top.

	Accelerations up to 500 of earth acceleration are typical and large temperature gradients are usual
Porous medium montage in engine components	Very critical:
	especially in the case of ceramic materials. Possible gluing using a high temperature ceramic glues. Important is also that the porous reactor ones is cold and once may be very hot. Metal foams could be more useful if their application temperature would be high enough
Variable geometry	Important:
	for all engine applications (adopting to available space and shape)
Long time stability	Should be very high:
	This is still almost unknown area for engine applications.

Large inner surface area

Owing to large inner surface area, the porous material permits the enlargement of the reaction zone owing to very effective heat transport between the gas phase and the porous medium. Additionally, this large specific surface area (of the order of 10^2 - 10^4 m^{-1}) prefers the medium to be applied as a vaporizer and heat exchanger. This inner surface area depends on the pore density, its geometry and the basic structure used for manufacturing of PM (see Fig. 9).
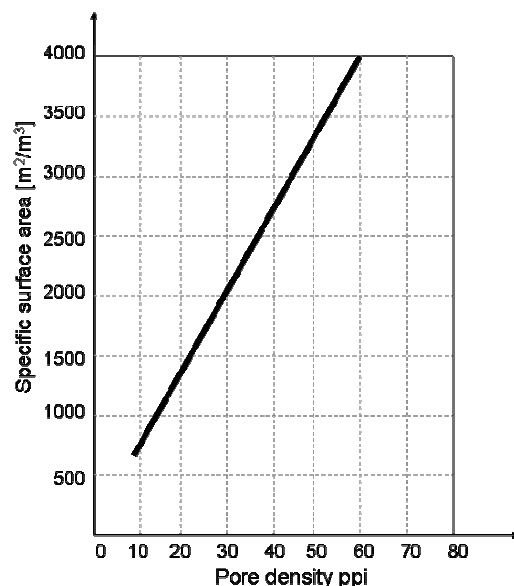
Figure 9: Specific surface area versus pore density for metal foam structures (acc. to Porvair Advanced Materials, USA)

For example, for metal foam made of Ni-Cr-Al the specific surface area (according to the mean pore diameter d_{mean}) for d_{mean}=0.9mm is 1700 m^{-1}, for

d_{mean}=1.4mm, the specific surface area is 1000 m^{-1}, and for d_{mean}=2.3mm is 500 m^{-1}.

Very effective heat transport properties

Heat transport properties of PM are characterized by efficient heat conductivity and very effective heat radiation inside PM (see Fig.10).

These excellent heat transport properties permit for combustion in porous medium much higher combustion rates than for a free flame (approximately 10 to 20 times higher).

Additionally, there is strong cooling of the reaction zone and in consequence the thermal NO$_x$ formation is significantly reduced (low-temperature combustion).
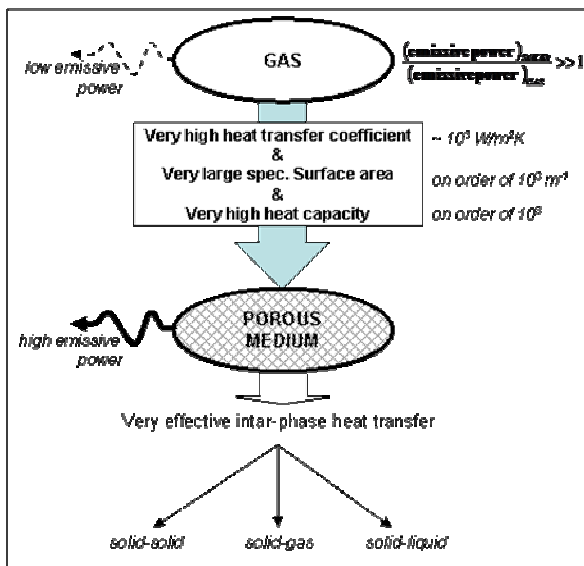
Figure 10: Comparison of emissivity for gas and for 3D-PM structure

Basic mechanisms for heat transfer in porous medium are selected in Table.2.

Table 2: Basic mechanisms for heat transfer in PM

Art of heat transfer in PM	Description and characterization
conduction	Heat transfer by conduction takes place using atomic and molecular interactions in the material and is based on Fourier's law: $$q = -\lambda \frac{\partial T_{f,s}}{\partial x}$$ $\lambda_{f,s}$ = heat conductivity (fluid "f" and solid "s")
convection	The convective heat transfer depends on the flow field, temperature field, heat capacity and the enthalpy of mixture. For description of convective heat transfer, a Newton's law may be applied: $$q = \alpha (T_f - T_w)$$ q = heat flow flux perpendicular to the wall,

	T_f = fluid temperature, T_w = wall temperature, α = heat transmission coefficient
Radiation	The surface-related heat flow, which is radiated by body into the half space, is given by $$q = E \cdot \sigma \cdot T_s^{4}$$ E = emissivity coefficient, σ = Stefan-Boltzmann, T_s = solid body temperature

Part of the heat released during the combustion process is „accumulated inside" the porous material resulting in a high temperature of the solid phase surface (see Fig.11).
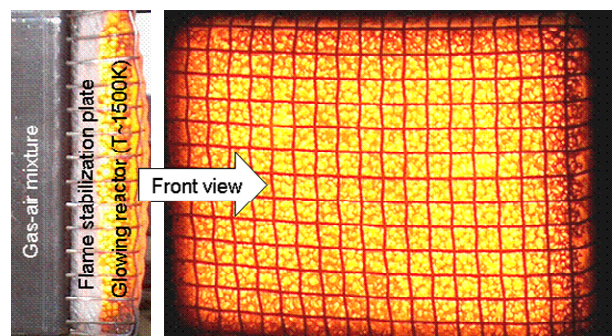
Figure 11: Example of flat PM-burner indicating strong heat radiation of the solid phase (SiC foam, T~1500K)

Large porosity and low pressure losses

As already indicated, highly porous materials mean structures of porosity over approx. 80%. Owing to this large porosity, the PM materials are transparent for gas and liquid flows as well as for flames. This transparency permits low pressure losses in fluid (gas) flow through the PM volume.

Pressure drop over the wire packing versus bulk velocity for three different PM lengths (50,100 and 150mm for constant packing density is shown in Figure 12.
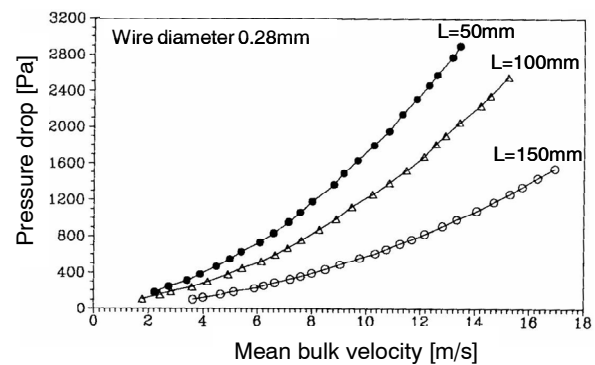
Figure 12: Pressure drop over the wire packing versus bulk velocity for three different PM lengths

Example of pressure losses measured for ceramic foam and different pore densities is given in Figure 13.
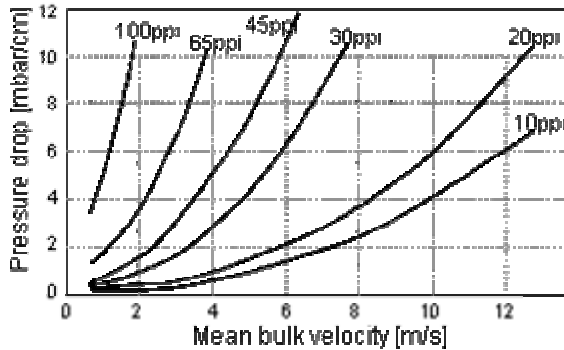
Figure 13: Pressure drop over the ceramic foams of different pore densities (ppi)

PM materials

Typical ceramic materials being of interest in application to PM-combustion technology are (see Fig.8): oxides (e.g. Al_2O_3, ZrO_2), and non-oxides (e.g. SiC). The cells of ceramic foam can be idealized as a pentagonal dodecahedron (Fig.14).

The edges of the dodecahedron are the struts of the ceramic foam. In the case of flowing gas through the foams, the flow is forced to separate and reattach at the struts, resulting in a good mixing and strong interaction between flowing gas and the PM material.
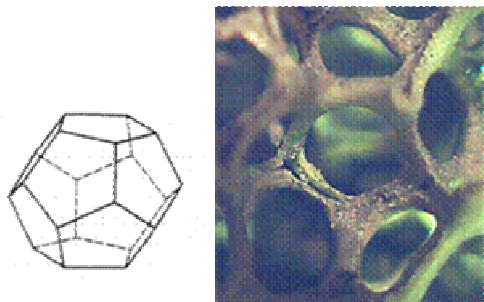
Figure 14: Structure of PU-Structure (left), SiC foam structure (right)

Thermal properties of PM materials

One of the most important features of PM materials used in combustion technology is their high thermal resistance, and especially important parameters are: maximum temperature, thermo-shock resistance and heat capacity. Example of glowing foam structures being under thermal test is shown in figure 15.
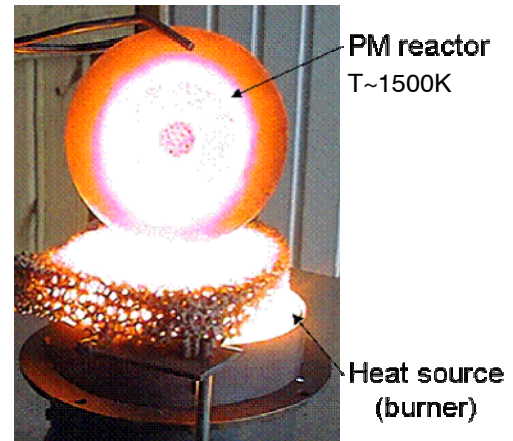
Figure 15: Thermal test of PM reactors for application to engine

Thermal properties of mostly used PM materials are selected in Table 3.

Electrically heated foams

A porous structure may also directly be electrically heated, resulting in a homogeneous temperature field throughout the PM-volume as shown in figure 16.
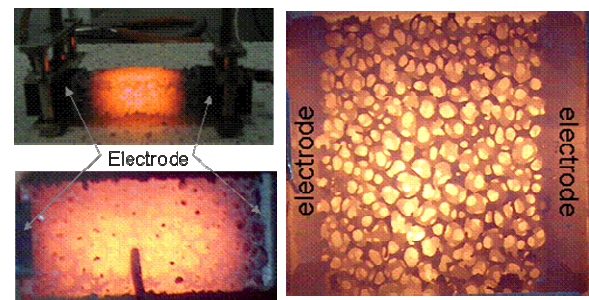
Figure 16: direct electrical heating of SiC-Reactor ($T_{PM}\sim1200K$) (U=12V)

3. Application of Porous medium technology to mixture formation and combustion in engines

Four different concepts concerning applications of PM-technology to mixture formation and combustion in IC engines are considered in this chapter:

1. New combustion system with mixture formation and homogeneous combustion in PM-volume, so-called *"PM-engine concept"* [4,5,6].

Table 3: Thermal properties of ceramic porous materials

Material	Specification	Mean linear thermal coefficient		Heat conductivity	Melting point	Application temperature
		$30 - 100°C$ $10^{-6}K^{-1}$	$30 - 600°C$ $10^{-6}K^{-1}$	$Wm^{-1}K^{-1}$	$°C$	$°C$
PSZ	partly stabilized zirconoxide		$9 - 13$	1,2 - 3	2700	900 - 2400
ATI	aluminiumtitanat		5,0	1,5 - 3		900 - 1600
Al₂O₃	aluminiumoxide 80 %	$5 - 7$	$6 - 8$	10 - 16	2050	1400 - 1500
Al₂O₃	aluminiumoxide 86 %	5,5 - 7,5	$6 - 8$	14 - 24		1400 - 1500
Al₂O₃	aluminiumoxide 95 %	$5 - 7$	$6 - 8$	16 - 28		1400 - 1500
Al₂O₃	aluminiumoxide >99 %	$5 - 7$	$7 - 8$	19 - 30		1400 - 1700
SSN	sintered siliconnitrid		$2,5 - 3,5)^4$	15 - 45		1750
RBSN	reactionbound siliconnitrid		$2,1 - 3)^4$	4 - 15		1100
HPSN	hot forced Siliciumnitrid		$3,0 - 3,4)^4$	15 - 40		1400
AIN	Aluminiumnitrid	$2,5 - 4$	$4,5 - 5$	100 - 180		1750
SSIC	pressureless sintered siliconcarbid		4 - 4,8	40 - 120	2800 [1]	1400 - 1750
SISIC	silicon infiltrated siliconcarbid		4,3 - 4,8	110 - 160		1380
HPSIC	hot forced siliconcarbid		3,9 - 4,8	80 - 145		1700
RSIC	recrystallized siliconcarbid	4,2	4,8	20		1600
NSIC	nitridbound siliconcarbid	4,2	4,8	$14 - 15$		1450
PS 1	Iron-chromium-aluminum-alloy			13	1500	1400

[1] dissociation starts at temperatures over 2000° C

2. New mixture formation system, with heat recuperation, vaporization and chemical recombination in PM-volume, so-called *"MDI-concept"* [1,7,8].

3. *"Intelligent engine concept"* based on the MDI-system permitting homogeneous combustion conditions (in a free cylinder volume) in a wide range of engine operational conditions [1,8].

4. Phased combustion system for conventional DI Diesel, with temporal and spatial control of mixture composition by utilization of interaction between Diesel jet and PM-structure, so-called *"Two-stage combustion"*.

Before describing new engine concepts with porous medium technology (as applied to combustion process), it is necessary to mention that there is a number of concepts already reported in the literature which describe application of PM technology (see also Table 4). Another group of systems that use a PM in engines concerns internal heat recuperation, but not combustion process itself. The main goal of such PM application to internal combustion engines is to influence the thermal efficiency of engine by internal heat recuperation.

The author goes a step forward and utilizes the PM-technology for direct influence of engine combustion process, especially for reducing the engine emissions.

There are also concepts combining the heat regeneration and catalytic reduction of toxic components, e.g. gaseous and particulates [9,10]. Heat flux and energy recirculation in such an engine has in detail been described in [11]. In this case the heat recuperator is attached to a rod and moves inside the cylinder, synchronized to the piston movement (Figure 17). For most of the cycle the porous regenerator is located close either to the cylinder head or to the piston surfaces. During the regenerative heating stroke, the porous insert moves down, and during the regenerative cooling stroke, the porous regenerator moves up toward the engine head.

Table 4: Overview of most important applications and patents in area
PM application to engines

H.F. Leissner: "Internal-Combustion Engine" US Patent No. 1,260,408 (1918)	J.C. Firey: "Porous burner Diesel engine" US Patent No. 4,381,745 (1983)
Device for mixture formation of heavy oil for internal combustion engine) German Patent No. 481754 (1929)	R.M. Siewert: "Catalytic late direct injection spark ignition engine" US Patent No.4,480,613 (1984)
Method and device for fuel preparation for a spark ignition engine Patent DE 2 306 362 (1973)	F. Durst, M. Weclas: "Method and device for converting heat into work" German Patent No.197 53 407 (1997)
W. Müller:Piston engine) Patent DT 24 16 804 (1974)	E. Pott: "Verbrennungsmotor" DE 198 57 071 A1 (1998)
W.C. Pfefferie: "Catalytic engine" US Patent No. 3,923,011 (1975)	M. Weclas: "Method of mixture formation for application to internal combustion engine" DE 198 13 891 (1998)
G. Bernecker: "Carburetor" US Patent No. 4,103,658 (1978)	M. Weclas: "Method for combustion of fuel and combustion chamber" German Patent Application No. 101 35 062.7 (2001)
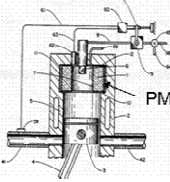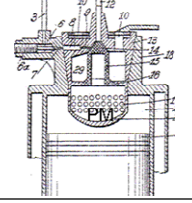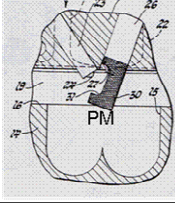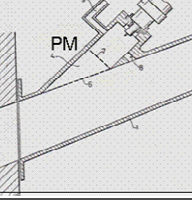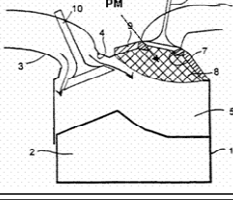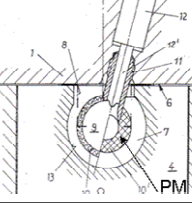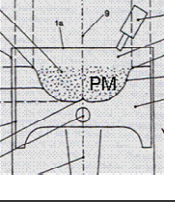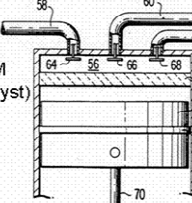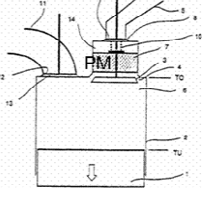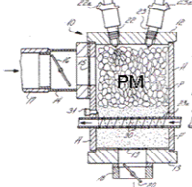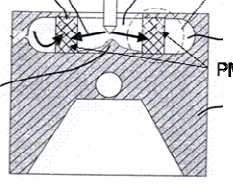
In the latter stroke, the burned gases enthalpy in the cylinder will partly transfer to the heat regenerator, and in the former stroke the accumulated heat will transfer to the cold air flowing through the porous regenerator increasing air enthalpy.

The main advantage of such internal (in-cylinder) heat recuperation between burned gases and fresh air is high volumetric efficiency of the cylinder necessary for a high power density of the engine.
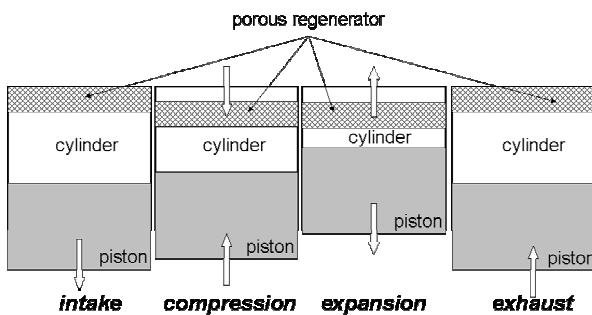
Figure 17: Principle of porous heat regenerator moving in the cylinder as synchronized with the piston movement

This kind of application of the porous medium to internal combustion engine deals with energy balance of the cycle but not directly with controlling of mixture formation or combustion processes occurring in engine.

The engine with heat recuperation could realize much higher combustion temperatures resulting in much higher NO_x emissions. The presented engine concept could also be extended by application of catalytic porous insert offering afterburning of combustion products, e.g. particles. Similar concept has recently been analysed by Hanamura and Nishio [9]. Also in this engine the maximal combustion temperature is higher than adiabatic one owing to the heat recuperation in a porous medium.

Another application of porous medium technology to internal combustion engines concerns exhaust after-treatment systems, especially catalytic converters and particle filters. This topic, however, will not be discussed in this chapter. More information on application of porous medium technology especially to diesel particle filters may be found in the literature [12-15].

3.1. Concept of the PM-engine: internal combustion engine with mixture formation and homogeneous combustion in porous reactor

PM-engine is here defined as an internal combustion engine with a homogeneous combustion process realized in a porous medium volume. The following individual processes of PM-engine are realized in porous medium volume: internal heat recuperation, fuel injection, fuel vaporization, mixing with air, homogenization of charge, 3D-thermal self-ignition, and a homogeneous combustion. The TDC (Top Dead

Centre) compression volume is equal to the PM-volume which creates the engine combustion chamber. Outside the PM-volume there is no combustion present in the cylinder. PM-engine may be classified with respect to the timing of heat recuperation in engine as:

- Engine with periodic contact between PM and cylinder (so-called closed PM-chamber).
- Engine with permanent contact between PM and cylinder (so-called open PM-chamber).

Another classification criterion concerns the positioning of the PM-reactor in engine. Here, three possible localizations may be selected: engine head, cylinder, and piston (Figure 18).

Interesting feature of PM-engine is its ability to operate with different liquid- and gaseous fuels. Independently of the fuel used, this engine is a 3D-PM-thermal self-ignition engine. Finally, the PM-engine concept may be applied to both two- and four-stroke cycle engines.
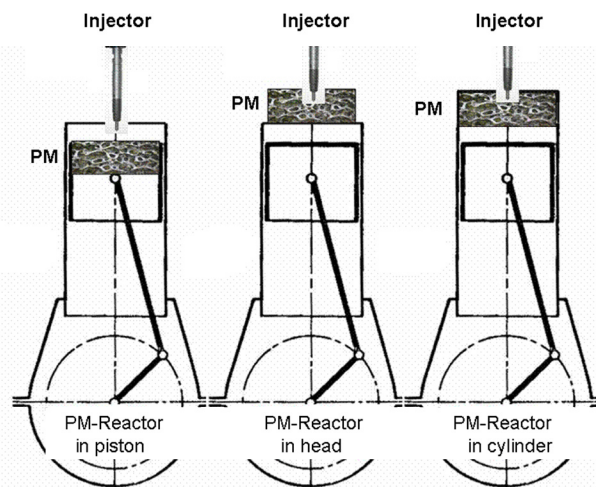
Figure18: Possible locations of PM-reactor in PM-engine concept

3.1.1. Concept of the PM-engine with a closed PM-chamber

Let us start this analysis with a case of closed PM chamber, i.e. engine with a periodic contact between working gas and PM-heat recuperator (Figure 19). At the end of the expansion stroke (Figure 19e) the valve controlling timing of the PM-chamber closes and fuel may be injected in the PM volume. This chamber is a low pressure chamber and a long time is available for fuel supply and its
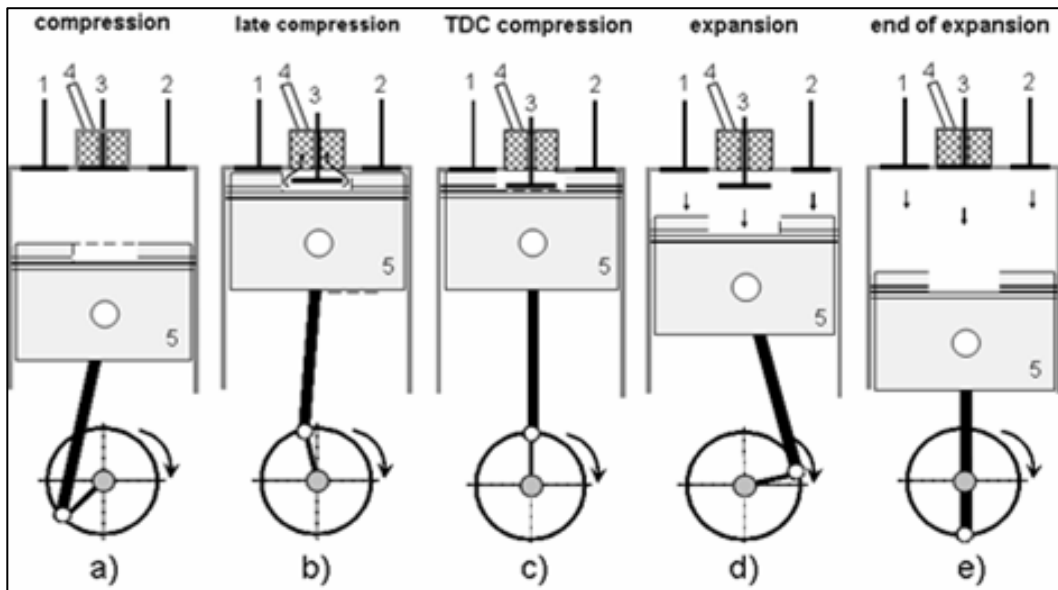
Figure 19: Principle of the PM-engine operation with a closed chamber; 1-intake valve, 2-exhaust valve, 3-PM-chamber valve, 4-fuel injector, 5-piston

vaporization in the PM-volume. Simultaneously, other processes may perform in the cylinder volume. These processes may be continued through exhaust, intake and compression strokes (Figure 19a).

Near the TDC of compression (Figure 19b) the valve in PM-chamber opens and the compressed air flows from the cylinder to the hot PM containing fuel vapours. Very fast mixing of both gases occurs before mixture igniting in the whole PM-volume (Figure 19c). The resulting heat release process performs simultaneously in the whole PM volume. Three necessary conditions for a homogeneous combustion are here fulfilled: homogenization of charge in PM-volume, 3D-thermal self-ignition in PM-volume and a volumetric combustion with a homogeneous temperature field in PM-volume.

Additionally, the PM deals as a heat capacitor and controls the combustion temperature level

3.1.2. Concept of the PM-engine with an open PM-chamber

Another possible realization of the PM-engine is a combustion system characterized by a permanent contact between working gas and PM-reactor. In this case it is assumed that the PM-combustion chamber is mounted in the engine head, as shown in Figure 20. During the intake stroke it is weak

influence of the PM-heat capacitor on the in-cylinder air thermodynamic conditions (Fig.20a). Also during early compression stroke, only small amount of air contact the hot PM. This heat exchange process (non-adiabatic compression) increases with continuing compression timing (Figure 20b), and at the TDC the whole combustion air is closed in the PM volume. Near the TDC of compression the fuel is injected into PM volume (Figure 20c) and very fast fuel vaporization and mixing with air occur in 3D-structure of PM.
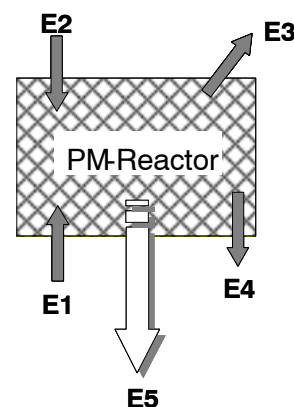
Figure 21: Energy balance of PM-reactor in PM-engine with open chamber: E1=energy supplied from compression; E2=energy supplied with fuel; E3=energy losses; E4=energy supplied from PM to the air; E5=energy transported with burned gases
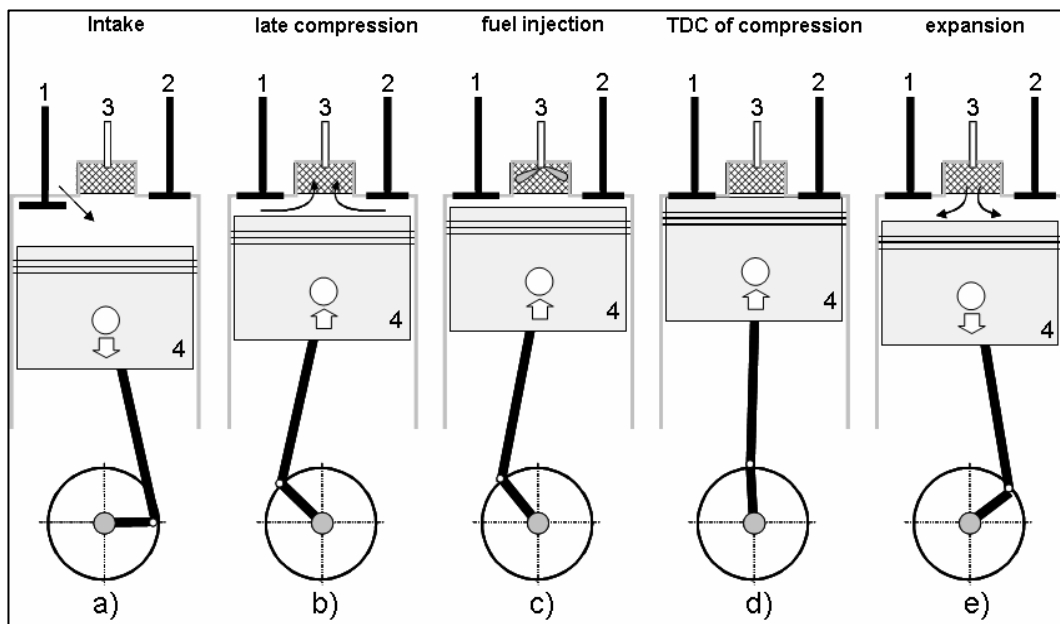
Figure 20: Principle of the PM-engine operation with an open chamber; 1-intake valve, 2-exhaust valve, 3-fuel injector, 4-piston

A 3D-thermal self-ignition of resulting mixture follows in PM-volume together with a volumetric combustion characterized by a homogeneous temperature distribution in PM-combustion zone. Here, the energy balance in the PM reactor defines thermodynamic conditions of the engine cycle (Fig. 21). During following expansion stroke the heat is transferring into mechanical work (Figure 21e). Again, all necessary conditions for homogeneous combustion are fulfilled in the PM-combustion volume. An example of the PM-engine head with open chamber and PM reactor mounted in the engine head is shown in Figure 22.

These first experimental investigations on the real PM-engine indicated its potential for (near) zero-emission operation in a very wide range of charge compositions (λ) and engine rates [4].

Especially noticeable is that no soot emissions were observed together with close-to zero NO_x emissions (~100mg/kWh), even for nearly stoichiometric charges. Noticeable was also extremely low combustion noise of the engine with combustion in porous reactor.

However, there were two technical problems limiting obtained results:
Material problem: for this first engine realization a SiC ceramic reactors have been chosen.
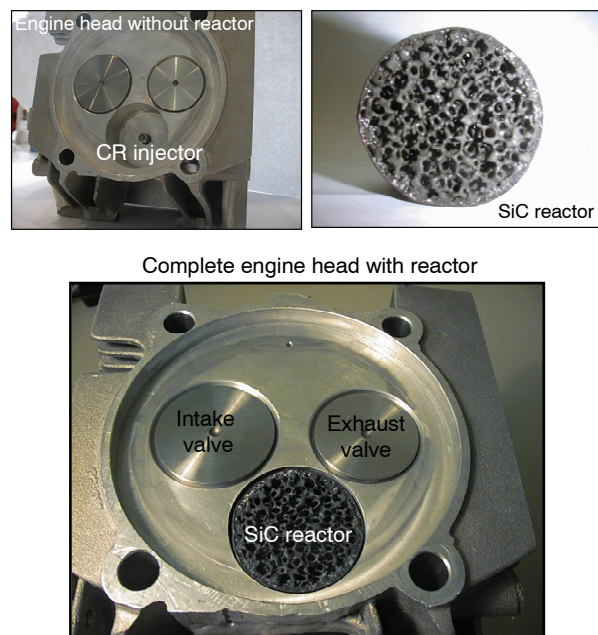
Figure 22: View of the PM-engine head with open chamber built on the basis of a single-cylinder DI-Diesel engine

One problem was to mount this ceramic reactor in engine, and on the other hand side the available reactor (material) quality was not very high (at least for this application).

Control of reactor temperature: the experiments have shown that the engine operation according to the PM-engine principle was only possible if required PM temperature has been achieved at the beginning of engine operation.

If PM-reactor temperature was too low, a low temperature oxidation performed in the PM-volume, and free volume afterburning late in the expansion phase has been observed in the cylinder. Of course, in this case the system could not work according to the PM-engine principle, despite of PM reactor built in the engine. A strong after-burning in the cylinder was then observed in part of the experimental investigations. The author wants to indicate that further development of the PM-engine concept requires, besides material development, basic research on low- and high-temperature oxidation processes in PM-reactor under pressure and on the transition between both reactions. It will be necessary to recognize the proper operational conditions for combustion in PM-reactor as suggested in Fig. 23. For this reason the author proposes to use a constant volume high pressure chamber simulating TDC of compression in PM-engine concept. In this case an electrically heating reactor allows setting the chamber (reactor) pressure independently of its temperature for different charge compositions.

vaporization, its chemical recombination (low temperature oxidation processes, e.g. cool- and blue-flames) and energy recirculation in a porous medium chamber. The enthalpy of the burned gases is partly transferred to the porous medium and can later be supplied back to the cylinder. This energy is utilized for both vaporization of liquid fuel and for its chemical recombination in the PM-volume [1,8].

A practical realization of the MDI system requires a porous medium chamber to be mounted in proximity to the cylinder and equipped with a valve (in this paper a poppet valve is considered – see Fig. 24) permitting contact between PM-chamber and the cylinder volume. The engine cycle described below, models the real engine cycle, and other than presented timings for PM-chamber may be used. MDI concept may be combined with conventional combustion modes, such as GDI (Gasoline Direct Injection), HCCI (Homogeneous Charge Compression Ignition) [16-19] and with radical combustion, and only control of the PM-chamber timing is necessary to select a combustion mode used in the engine [8]. By applying the variable timing of the PM-chamber, a MDI concept offers combination of individual combustion modes in one engine, as described

Figure 23: Sill not well recognized combustion modes in porous reactor under pressure
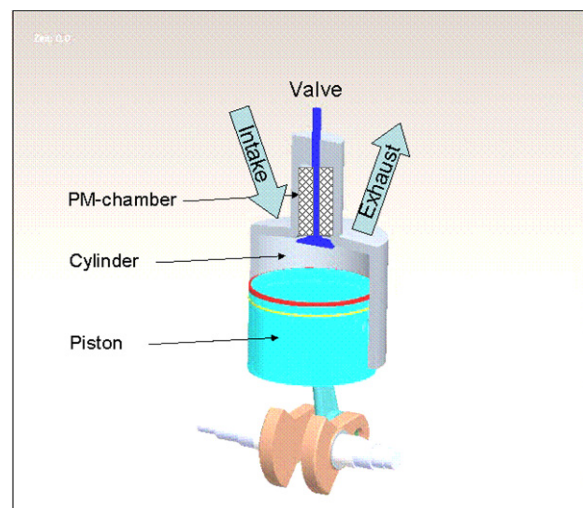
Figure 24: Principle of MDI system design and intelligent engine

3.2. Concept of MDI-engine: intelligent engine concept with application of PM-chamber for mixture formation

MDI (Mixture Direct Injection) concept describes mixture formation and heat recuperation system. This concept offers homogenization of the combustion process by performing fuel

below. Characteristic phases of the cycle with MDI mixture preparation are as follows:

Phase I: PM-chamber is charged with a burned gases containing energy (Figure 25).

Phase II: Liquid fuel is injected to PM chamber and fuel vaporization performs.
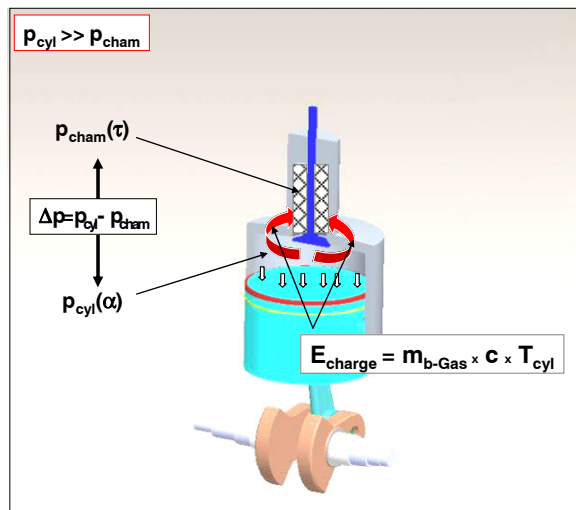
Figure 25: PM-chamber charging with burned gases (in this case expansion stroke)

Phase III: Gaseous charge containing evaporated fuel, energy, and active radicals discharges from PM-chamber to the cylinder (non-combustible mixture) − Fig.26.

Phase IV: Mixing with air in the cylinder and ignition of combustible mixture is realized
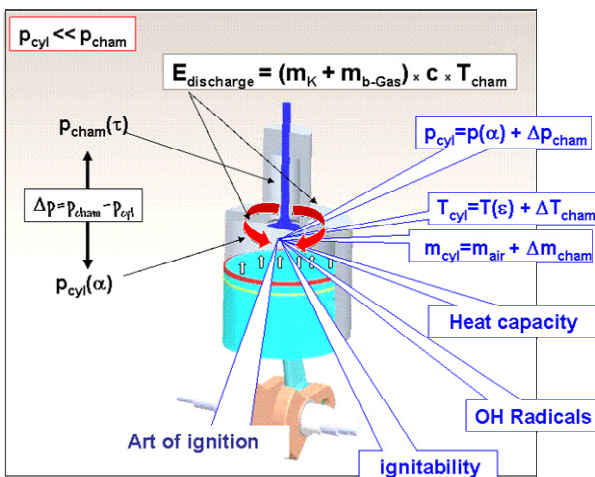
Figure 26: Gas discharge from PM-chamber to the engine cylinder (in this case compression stroke**)**

The chamber charging pre-defines possible timing for gas discharge to the cylinder. This discharge process is performing under such conditions that the chamber pressure is much higher than the cylinder pressure. Combining (pairing) of both

chamber timings defines an individual combustion mode in intelligent engine concept.

This variability of the chamber timing allow to control a v*ariable amount of energy supplied to the chamber* resulting in variable temperature of the cylinder charge, and variable end of compression cylinder temperature (using constant compression ratio). A v*ariable hot EGR realized in the chamber* together with variable mass of fuel results in variable heat capacity of the cylinder content.

A Variable timing of the chamber results in variable temperature history in the cylinder during intake and/or compression strokes, and influences the ignition conditions in the cylinder. *Variable engine load* means variable mass of fuel supplied to the chamber but still long time is available for fuel supply and complete vaporization, what is very important for generation of homogeneous gaseous charge in the cylinder.

Variable engine speed results in variable timing of the cycle in the cylinder, but in the chamber the same crank angle period is available for fuel supply, its vaporization, and chemical recombination. Additionally, a v*ariable temperature of the gas supplied to the chamber* and then to the cylinder charge temperature results in variable chemical activity of the charge. If the chamber gas has a proper temperature, there is possible to perform a low-temperature oxidation processes resulting in higher chemical activity and higher radicals concentration. *Different timings are available for gas supply* from the chamber to the cylinder, however, only one requirement is given that $p_{chb} >> p_{cyl}$.

MDI system offers the following abilities for variable engine load and speed:

- *Variable amount of energy supplied to the chamber (E_{suppl})* results in variable temperature of the cylinder charge, and variable compression temperature.
- *Variable hot EGR realized in PM-chamber (m_{b-gas})* together with variable mass of fuel results in variable heat capacity of the cylinder content.
- *Variable timing of the PM-chamber (τ)* results in variable temperature history in the cylinder during intake and/or compression strokes.
- *Variable engine load* means variable mass of fuel (m_{fuel}) supplied to the PM-chamber but still with long time available for fuel supply and complete vaporization.

- *Variable temperature of the gas supplied to the chamber* and then to the cylinder results in variable chemical activity of the charge.
- *Variable engine speed results* in variable timing of the cycle in the cylinder, but in PM-chamber the same period of crankangle is available for fuel supply and vaporization.
- *Different timings are available for gas supply* from the PM-chamber to the cylinder, however only one requirement is given: $p_{PM} >> p_{cyl}$ *Despite of variable speed and load*, in the engine cylinder mix two gases under strongly turbulized conditions resulting in pretty well premixed gaseous charge prior ignition.

For homogeneous combustion under variable engine load and speed it is required that ignition conditions and charge reactivity are also variable [8]. This variability means variable ignition and combustion mode (see intelligent engine concept). The combination of these variable conditions allows not only realization of homogeneous combustion conditions (see definition) but also permits control of ignition timing and of heat release rate. Both aspects define practicability of the combustion system operating under homogeneous combustion conditions. Thus, the variable timing of MDI concept permits control of the cylinder charge parameters, which are necessary for realization of homogenous combustion process: TDC compression temperature; temperature history during the compression stroke; reactivity (chemical activity) of the charge; homogeneity of the charge (with completely vaporized fuel); heat capacity of the charge.

3.3. Concept of two-stage combustion system for DI Diesel engine

Another application of porous medium technology to mixture formation and combustion in DI Diesel engine represents *"two-stage combustion"* concept [1]. This concept offers control of mixture formation and combustion conditions in direct injection Diesel engines by spatial splitting of the combustion process into three zones and two time phases (Figure 27):

Zone 1: Volume of the inner part of the PM-ring
Zone 2: PM-ring volume
Zone 3: Free volume between outer part of PM-ring and piston bowl.

Analysis of engine operating with a two-stage combustion principle has to be selected in to two operational ranges: part and full load conditions. The analysis presented below explains the principle of operation and the geometry shown is used as an example for describing the engine cycle, only.
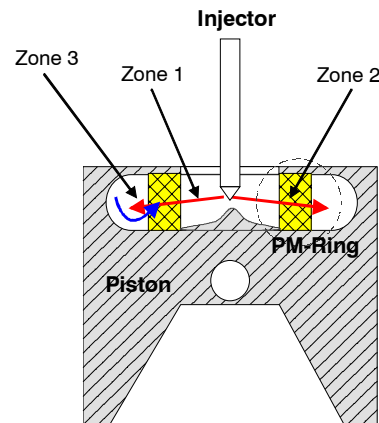
Figure 27: Principle of PM-ring in piston bowl of Diesel engine for two-stage combustion system

Part load operational conditions
Under part load operational conditions the fuel is injected in to the combustion chamber with a relatively low impulse, in practice under lower injection pressure for smaller amounts of fuel. The combustion chamber geometry, PM geometry and injection conditions are chosen in such a way that the fuel penetrates throughout zone (1) until reaching the PM-ring and distributes inside its volume (Figure 28). Depending on the PM structure and its geometry (PM thickness) and on the injection parameters, the zone (3) is filled with air or with very lean mixture. All this happens during the upward motion of the piston toward the TDC of compression.
The mixture formation conditions in PM are very advantageous for very effective fuel vaporization under intense mixing with air (pre- and -ignition conditions). The ignition process of the mixture is *at least partly* stimulated by the hot PM. The mixture is spatially ignited and burns (mostly) in zones (1) and (2).

Part of the energy is accumulated in PM reducing the local temperatures. During the second stage of combustion, a strong gas flow from zone (3) through PM to zone (1) occurs during the downward motion of the piston (early expansion phase). During this flow through PM the charge is heated, and a strong turbulization of the gas occurs during this part of the cycle. This mixture with a high O_2 concentration improves second stage of combustion in zone (1). Again the combustion

conditions in zone (1) permit low NO_x emissions and excellent conditions for oxidizing of such components as CO, HC and soot.

the mixture is *at least partly* stimulated by the hot PM. The mixture is spatially ignited and burns (mostly) in zones (3) and PM. Part of the energy is accumulated in PM reducing the local temperature.
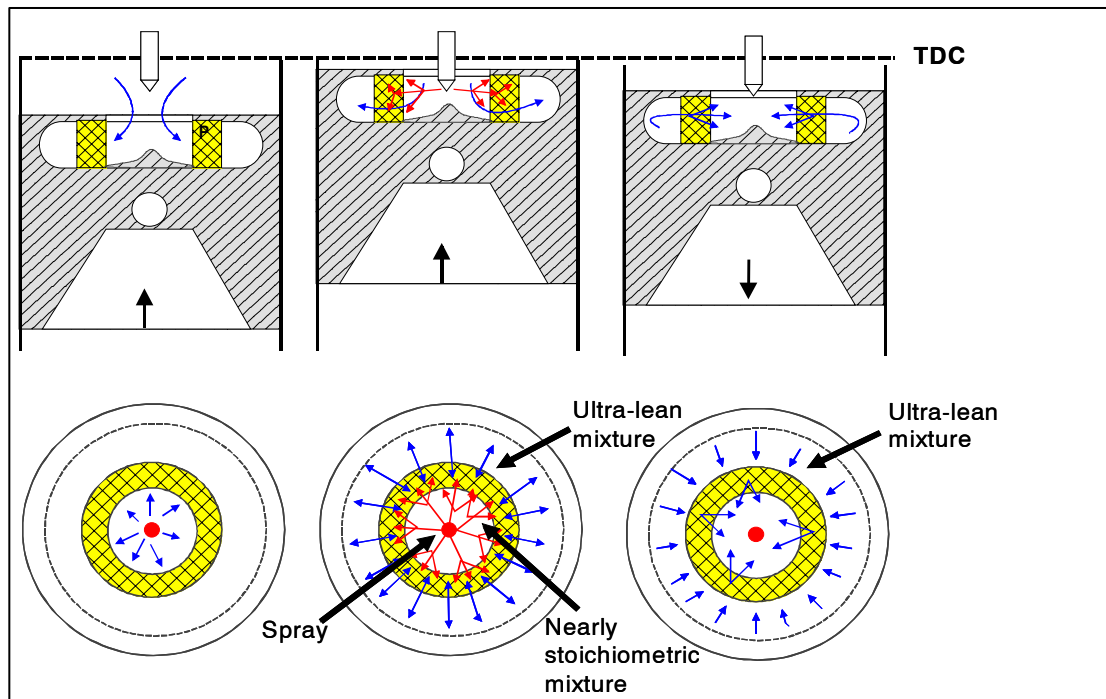
Figure 28: Two-stage combustion under part load operation

High (full) load operational conditions
Under high load this operational conditions the fuel is injected in to the combustion chamber with high impulse, in practice under high injection pressure for a large amount of fuel injected per cycle (Figure 29). The combustion chamber geometry, PM geometry and injection conditions are chosen in such a way that the fuel penetrates throughout zone (1), throughout PM-ring (zone 2) until reaching the volume (3). Depending on the PM structure and its geometry (thickness) and on the injection parameters, the zone (3) is filled with relatively rich mixture. All this happens during the upward motion of the piston.The mixture formation conditions in PM are very advantageous for very effective fuel vaporization under intense mixing with air (pre- to –ignition conditions).
The fuel passing the PM is spatially distributed in PM, (at least) partly evaporated and partly premixed with air. It results in nearly homogeneous rich charge present in zone (3) and PM volume. It is expected that no wall film is present on the combustion chamber (zone 3) significantly reducing the soot formation. The ignition process of

During the second stage of combustion, a strong (mostly burned) gas flow from zone (3) through PM to zone (1) occurs during the downward motion of the piston. During this flow through PM the charge is strongly turbulent. A second stage of combustion occurs in zone (1). Here the mixture consists of relatively high O_2 concentration improving the second-stage combustion quality. Again the combustion conditions in zone (1) permit low NO_x emissions and excellent conditions for oxidizing of such components as CO, HC and soot.

Main features of the *two-stage combustion* system are the following:

1. The system operates under two characteristic conditions related to the part and full load (i.e. small amount of fuel injected under low pressure, and large amount of fuel injected under high pressure).

2. PM divides the combustion chamber in three parts (zones 1 to 3) and significantly influences the fuel distribution, fuel vaporization, mixing
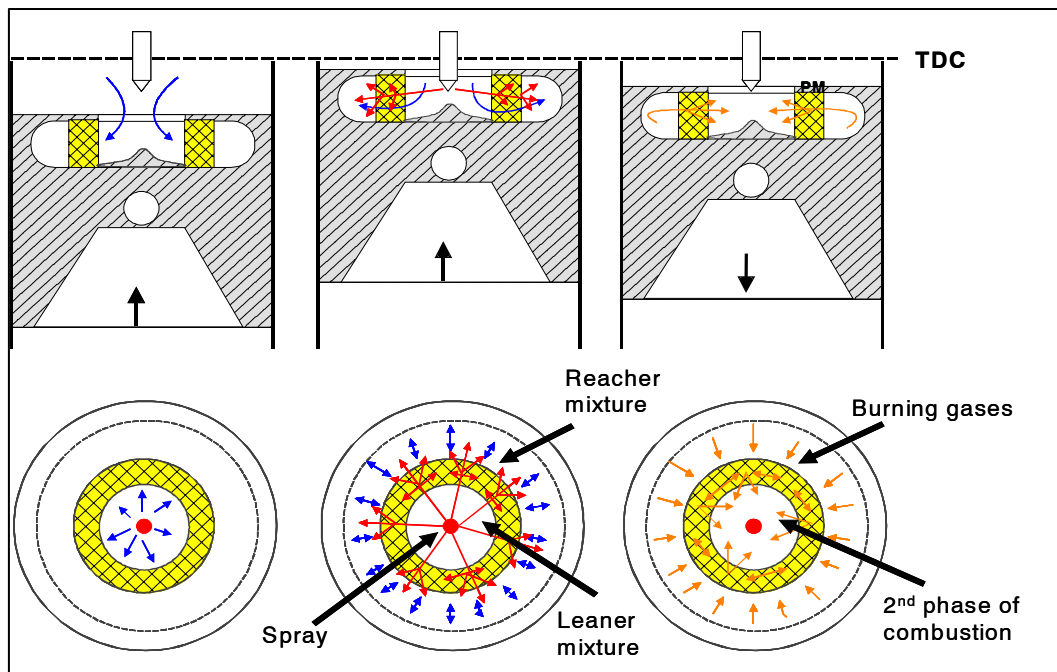
Figure 29: Two-stage combustion under full load operation

with air and generates turbulence during the gas flow through PM-ring.

3. in the combustion process, but significantly influences the temperature of the zone by accumulating part of the energy released, and improves self ignition from the hot-PM-walls.

4. Generally the system operates in such a way that the following mixture conditions are achievable: reach mixture (in a free volume), lean mixture (in a free volume) and any mixture composition in PM. Combustion of such a mixture permits low NO_x level and low soot emissions.

5. Generally two-stages of the combustion process may be selected, independently of the operational conditions: early stage: from late compression until TDC (upwards piston motion); late stage: from TDC until completion of combustion (downwards piston motion).

Transition between both stages of combustion is connected with a strong gas flow through the PM generating turbulence and significantly improving the mixing of gases. In both stages of combustion the porous medium (partly) control the ignition and combustion process.

4. Potential of PM-technology as applied to mixture formation and homogeneous combustion in IC engines

Two different criteria are considered in this chapter for predicting the potential of emissions reduction for a given combustion system:

•   Potential for homogenization of combustion process.
•   Potential for operating under variable operational conditions (part and full loads, stoichiometric and very lean charges, ignition timing, heat release etc).

Main goal is to achieve a homogeneous combustion for a (near−) zero emission engine. Required engine operational conditions (keeping homogeneous combustion process) are from idle, through part to full load operation.
Potential of porous medium technology as applied to combustion in engine will be analysed based on four fundamental processes realized in IC engine: gas flow, liquid fuel injection, mixture formation and ignition with combustion. Three characteristic systems are used for this comparison: a conventional DI system, PM-engine system, and MDI system
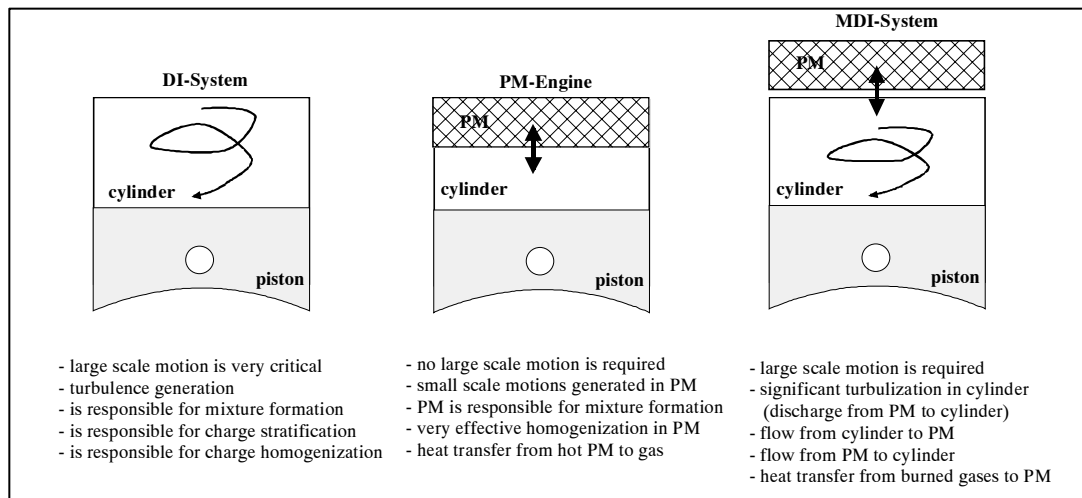
Figure 30: Flow processes in DI system, PM-engine and MDI

In gas flow processes, a large-scale in-cylinder flow structures (e.g. swirl, tumble) in the DI-system are responsible for mixture formation being dependent on the engine speed and load (see Figure 30). Not less important is the turbulence generated in the cylinder, especially during the intake stroke. Generation of a large-scale flow structures reduces the flow efficiency through the intake port-valve assembly. Additionally, flow separations define the discharge conditions in to the cylinder and formation of a recirculation zone under the valve [20,21].

These problems do not exist in PM-engine concept, where no large-scale flow structure is required in the cylinder. Here, the system optimization with respect to maximization of the volumetric efficiency (mass of air) may be performed. Also the intake generated turbulence is not important, while a small scale motions are generated during the gas flow in a porous medium.

If the gas is pushed in to the PM-volume a strong heat transfer from a solid phase of PM and gas is observed together with a spatial homogenization of the gas in the PM-volume. In this case it is assumed that the temperature is homogeneous throughout the PM-volume.

Different role plays a porous medium in MDI system. Here a large-scale flow structure in cylinder volume may play important role in mixing process. Very important are processes of gas flow between cylinder and PM-chamber, and corresponding heat transfer from burned gases to

PM solid phase. Advantageous is a strong charge turbulization during gas discharging from PM to the cylinder volume supporting the mixing process in the cylinder.

One of most critical aspects in conventional combustion systems is liquid fuel injection. Three main injection parameters may be selected for DI system: injection timing characterized by injection beginning and duration, spray atomization and spray geometry (Figure 31). Especially the last two parameters are very difficult to be controlled under variable engine operational conditions, e.g. see [22]. The fuel injection in DI system is responsible for mixture formation, charge stratification or charge homogenization, depending on the combustion system to be analysed.
Additionally, a low vaporization rate of liquid fuel limits the rate of mixture formation and its homogenization in the cylinder.

Quite different situation is observed in two other systems that use a porous medium technology. In the PM-engine the liquid fuel is injected directly in to PM-volume and fuel atomization and spray geometry are not critical. A self-homogenization process in PM-volume is observed permitting spatial distribution of the liquid fuel throughout the PM-volume (Fig. 32). There are four characteristic phases of the jet interaction with the porous medium [3]:

- Phase A represents outlet from the nozzle and free jet formation.
- Phase B represents jet interaction with PM-interface.
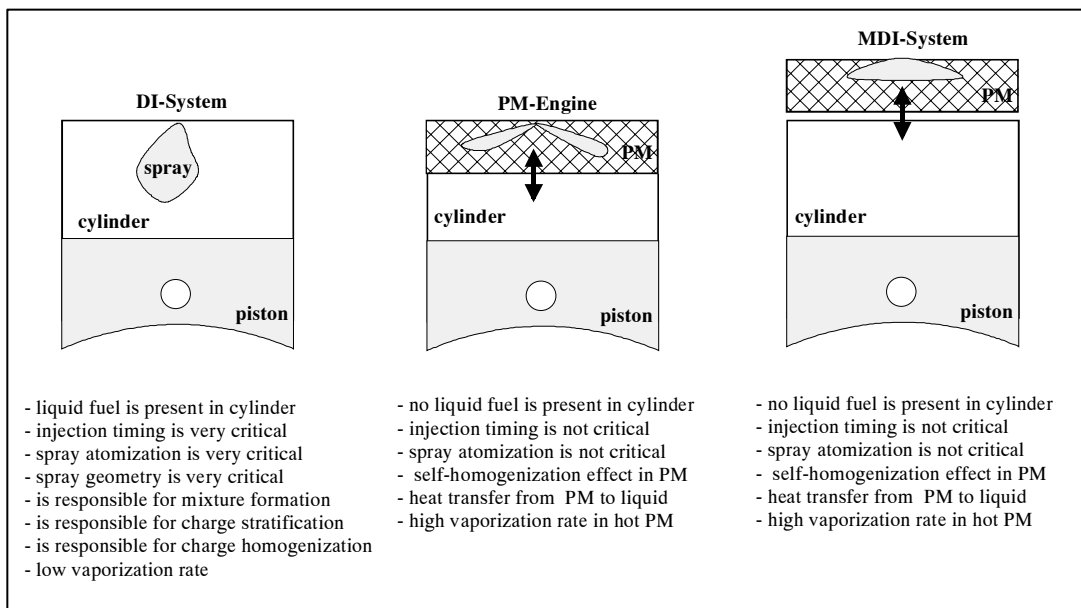
Figure 31: Fuel injection in DI-system, PM-engine and MDI

- Phase C represents liquid distribution throughout the PM-volume.
- Phase D represents liquid leaving the PM-volume.

Figure 32: Model describing basic phases of Diesel jet interaction with a porous medium [3]

In a free space between nozzle outlet and porous medium (defined by the distance between nozzle and PM) a free jet may penetrate throughout available space until impinging on to PM surface (phase A). The jet impingement on to PM-surface may be divided in two parts: jet reflection from the interface (phase B) and jet penetration into PM followed by liquid propagation throughout the PM-volume (phase C) − see Fig.33. This impingement and division between phases B and C depend not only on the injection parameters (e.g. injection pressure) and nozzle geometry but also on the distance from the nozzle outlet, as well as on the pore size and its density.

In Phase C the jet distributes throughout the PM-volume and this process is characterized by a wide jet spreading ("self-homogenization") as an effect of a multi jet splitting (Figure 34 und 35). The multi-
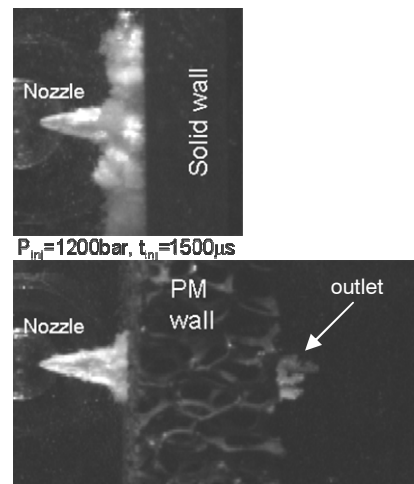
Figure 33: Comparison of Diesel jet impingement on to solid and porous wall

jet splitting is a result of jet interaction with a large number of pore junctions present in the PM-volume. Depending on the jet impulse, PM geometry, pore size and density, part of the liquid may leave the PM-volume (phase D).

A strong heat transfer from hot PM-surface to liquid fuel permits fast and complete fuel vaporization. No

DI-System

mixture formation and homogenization

cylinder

piston

PM-Engine

PM

cylinder

piston

MDI-System

PM

cylinder

piston

- two-phase charge in cylinder
- mixture formation significantly depends on the engine load
- mixture formation significantly depends on the engine rate
- spray atomization is very critical
- problems with controlled stratification
- problems with controlled homogenization
- slow diffusion processes

- only gas in cylinder
- mixture formation conditions are almost independent of engine operational conditions
- spray atomization is not critical
- self-homogenization effect in PM
- processes are performed under high temperature conditions

- only gas in cylinder
- mixture formation conditions are almost independent of engine operational conditions
- spray atomization is not critical
- homogenization effect in cylinder via strong turbulization from PM
- two-stage mixture formation:
  1.non-combustioble mixture in PM
  2.combustible mixture in cylinder

Figure 36: Mixture formation in DI-system, PM-motor and MDI

liquid or gaseous form of the fuel are present in a free volume of the cylinder (fuel is present in PM-volume, only). Injection timing, spray atomization or
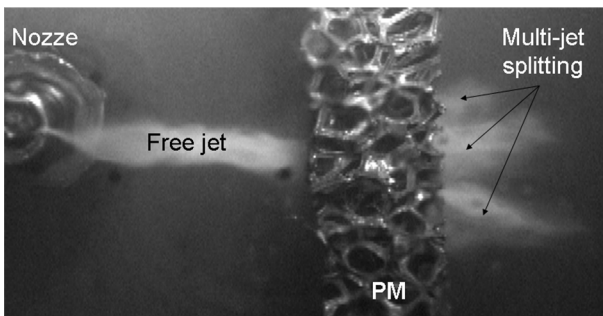
Figure 34: Multi-jet splitting effect in a porous medium

P_{rail}=135PMa, t_{inj}=4ms
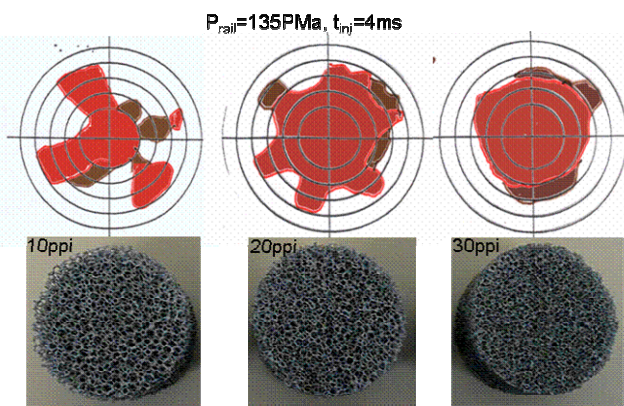
Figure 35: Spatial homogenization of Diesel injection in PM volume

spray geometry are not critical in this system. In MDI system a liquid fuel is directly injected in to PM-volume, while this volume has no connection with the engine cylinder at this time. A strong heat transfer from got gases and PM to the liquid fuel occurs under very low oxidant concentration conditions. Complete fuel vaporization is permitted in the PM-volume, and only gaseous form of the fuel is supplied back to the cylinder.

Mixture formation and charge homogenization conditions in DI system are very complex and difficult to be controlled (Figure 36). Generally, there is a two-phase charge present in the cylinder and mixture formation significantly depends on the engine load. In this case, in-cylinder flow structure and spray atomization are very critical for this process. On one hand side, there is a problem with controlled charge homogenization in DI system, on the other hand side, controlled charge stratification is required in GDI system.

Significantly different mixture formation conditions occur in PM-engine. Here, a 3D-PM structure controls the charge homogenization and fuel distribution in the PM-volume. In this case, the mixture formation conditions are almost independent of the engine operational conditions. The spray atomization and in-cylinder flow structure are not critical for the quality of the mixture formation. Again, self-homogenization effect in PM-volume permits pretty well homogenization of the charge to be exposed to a high temperature conditions.
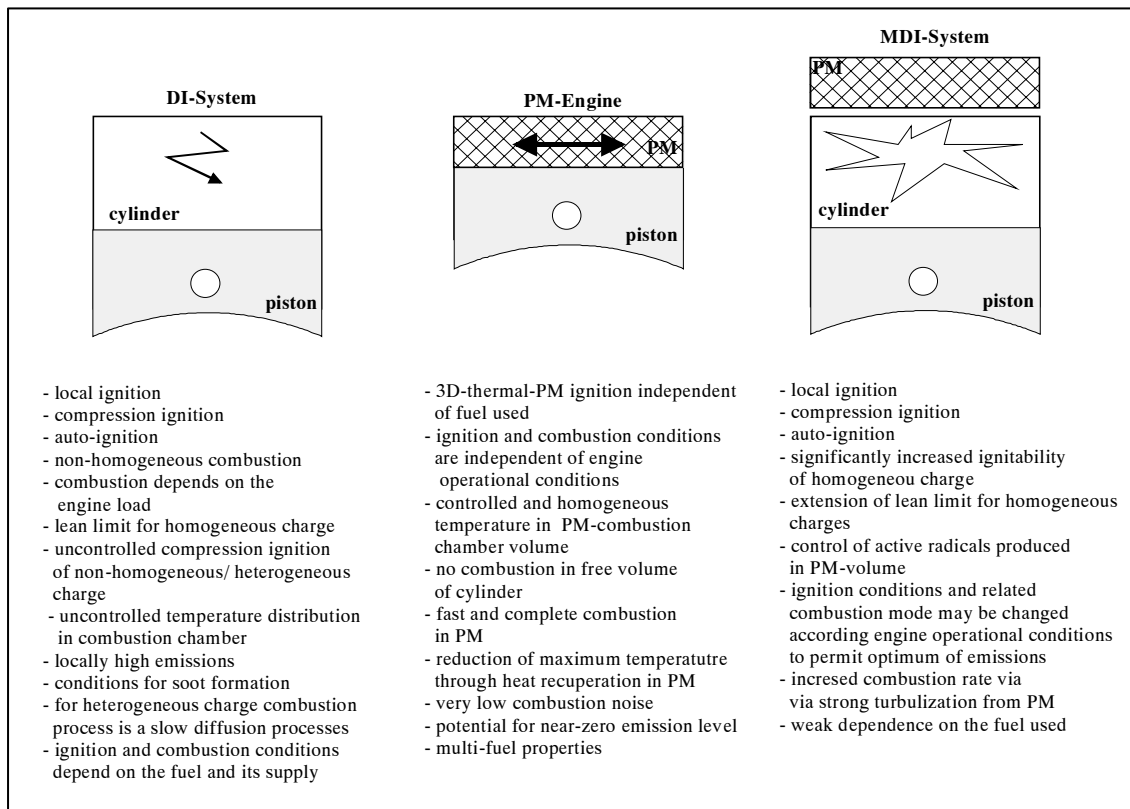
Figure 37: Ignition and combustion in DI-system, PM-engine and MDI

Also in MDI system no liquid fuel is present in the cylinder, however, formation of combustible mixture does not occur in PM-volume but in a free space of the cylinder. Mixture formation conditions are weakly dependent of the engine operational conditions, whereas the fuel is completely vaporized and the cylinder content is highly turbulent. Two-stage mixture formation is realized in MDI system. In the first stage, a non-combustible mixture is formed in the PM-volume containing burned gases and fuel vapours. In the second stage, a combustible mixture is formed in the cylinder as a result of mixing between air and gaseous content of the PM-chamber.

There are three possible modes of the ignition in a conventional DI system: local ignition, compression ignition and auto-ignition (see Fig. 37). Generally, the resulting combustion is a non-homogeneous process with uncontrolled temperature distribution in the combustion chamber. Ignition and combustion of homogeneous charges is limited to nearly stoichiometric mixture compositions, whereas the effective lean limit defines the possible conditions under engine part load operation. The art of ignition and resulting combustion process depends on the fuel used in the engine and on the fuel injection conditions.

Quite different conditions are observed in the PM-engine system. Here, independently of the engine operational conditions a 3D-thermal-PM-self ignition of the homogeneous charge is realized in the PM-volume. The combustion process is characterized by a homogeneous and controlled temperature in the whole PM-chamber volume, and no combustion occurs in the free volume of the cylinder. The maximum temperature is reduced by heat accumulation in the porous medium giving rise to very low NO_x emissions independently of the engine operational conditions [23]. Owing to the reduced temperature and pressure peaks, this combustion system is characterized by a very low combustion noise. Generally, this is only one known system fulfilling all necessary conditions for a homogeneous combustion process with controlled temperature, offering a near-zero emission level. This is a mono-mode adaptive combustion system.

Also MDI system offers significant advantageous in combustion process. This system may adaptively operate with all three modes of ignition having potential for a multi-mode intelligent combustion

system. MDI concept significantly increases ignitability and extends the lean effective limit for homogeneous charges. The combustion conditions are weakly dependent on the fuel used in the engine.

5. Concluding remarks

A porous medium technology has been defined as an utilization of large specific surface area, large heat capacity, high porosity etc. of open cell structures for supporting different processes realized in engine. Especially important is the application of this materials to mixture formation and combustion in engines.

In this paper novel concepts for combustion engines based on the application of porous medium technology are presented and discussed. The main attention is focused on the engine concepts having potential for homogeneous combustion process under variable engine operational conditions: intelligent engine and engine with combustion in a porous reactor.

It was shown that porous media, can be used for a great variety of improvements in the combustion process, especially for ellimination of soot emissions and significant reduction of thermal NOx. Combustion process in poorus reactor is homogeneous, flamless and uses a new art of volumetric thermal ignition in the porous medium volume.

All these processes (e.g. gas flow, fuel injection and its spatial distribution, vaporization, homogenization, ignition and combustion) can be controlled or positively influenced with the help of porous media/ceramic foams or other structures.

References

[1] Weclas, M., Porous media in internal combustion engines, [in:] Cellular Ceramics-Structure, Manufacturing, Properties and Applications, Scheffler, M., Colombo, P. (eds), Wiley-VCH-Publ.2005.

[2] Weclas, M., New strategies for homogeneous combustion in I.C. engines based on the porous medium (PM)-technology, ILASS Europe, June 2001.

[3] Weclas, M., Ates, B., and Vlachovic, V., Basic aspects of interaction between a high velocity Diesel jet and a highly porous medium (PM), 9th Int. Conference on Liquid Atomization and Spray Systems ICLASS, 2003.

[4] Durst, F., Weclas, M., A new type of internal combustion engine based on the porous-medium combustion technique, J. Automobile Engineering, IMechE, part D, 2001, Vol. 215, pp. 63-81.

[5] Durst, F., Weclas, M., A new concept of IC engine with homogeneous combustion in porous medium (PM), 5th International Symposium on Diagnostics and Modelling of Combustion in Internal Combustion Engines, COMODIA, 2001, Nagoya, Japan.

[6] Durst, F., Weclas, M., Method and device for converting heat into work, Patent Application, German Pat. No. 197 53 407, US Pat. No. 6,125,815, 1997.

[7] Weclas, M., Verfahren zur Erzeugung eines Flüssigbrennstoff-/Luftgemisches zum Betrieb einer Wärmekraftmaschine, German Pat. Appl. No. 198 13 891, 1998.

[8] Weclas, M., Strategy for intelligent Internal Combustion engine with homogeneous combustion in cylinder, Sonderdruck Schriftenreihe University of Applied Sciences in Nuernberg, 2004, No. 26, pp.1-14.

[9] Hanamura, K., Nishio, S., A feasibility study of reciprocating-flow super-adiabatic combustion engine, The 6th ASME-JSME Thermal Engineering Joint Conference, 2003, Paper No. TED-AJ03-547.

[10] Particulate traps for heavy duty vehicles, Report of Swiss Agency for the Environment, Forests and Landscape (SAEFL), 2000, Environmental Documentation No. 130.

[11] Park, C-W., Koviany, M., Evaporation-Combustion affected by in-cylinder, reciprocating porous regenerator, Trans. of ASME, 2002, Vol. 124, pp. 184-194.

[12] Mayer, A., Definition, Measurement and Filtration of ultrafine solid Particles emitted by Diesel engines, ATW-EMPA-Symposium 19th of April 2002.

[13] Schäfer-Sindlinger, A., Vogt, C.D., Hashimoto, S. Hamanaka, T., Matsubara, R., New Materials for Particulate Filters in Passenger Cars, Auto Technology, 2003, No. 5.

[14] Weclas, M., Diesel soot (PM) emissions and DPF technologies: state of the art, Internal Report, 2004, Institute of Vehicle Technology, University of Applied Sciences in Nuernberg

[15] Bovonsombat,P., Kang,B-S., Spurk,P., Klein, H., Ostgathe, K., Development of Current and Future Diesel After Treatment Systems, MECA/AECC Meeting, 2001, Bangkok, February 1.

[16] Kusaka, J., Yamamato, T., Daisho, Y., Simulating the homogeneous charge compression ignition process using a detailed kinetic model for n-heptane mixtures, Int. J. Engine Research, 2000, Vol.1, 3, pp. 281-289.

[17] Urushihara, T., Hiraya, K., Kakuhou, A., Itoh, T., Parametric study of gasoline HCCI with various compression ratios, intake pressures and temperatures, Proc. A New Generation of Engine Combustion Processes for the Future?, Ed. P. Duret, 2001, pp.77-84.

[18] Haßler, S., Homogene Verbrennung in Motoren als Lösung zur Emissions- und Verbrauchsreduzierung: Ansätze und Perspektiven, Diplomarbeit at University of Applied Sciences in Nuernberg, Suppervisor: M. Weclas, August 2004.

[19] Coma, G., Gastaldi, P., Hardy, J.P., Maroteaux, D., HCCI combustion: dream or reality? Proc. of 13th Aachen Colloquium on Vehicle and Engine Technology, 2004, Aachen, pp. 513-524.

[20] Weclas, M., Melling, A., Durst, F., Unsteady intake valve gap flows, SAE Technical Paper, No. 952477, 1995.

[21] Weclas, M., Melling, A., Durst, F., Flow separation in the inlet valve gap of piston engines, Progress in Energy and Combustion Science, 1998, vol. 24 (3), pp.165-195.

[22] Brenn, G., Durst, F., Trimis, D., Weclas, M., Methos and tools for advanced fuel spray production and investigation, Atomization and Sprays, 1997, vol. 7, pp. 43-75.

[23] Durst, F., Weclas, M., Mößbauer, S., A New Concept of Porous Medium Combustion in I.C. Engines, International Symposium on Recent Trends in Heat and Mass Transfer, 2002, Guwahati, India.

.

Heat transfer model for the simulation of spindle heating and expansion inside a multiphase screw pump

Dipl.-Ing. (FH) Klaus Räbiger
Prof. Dr. T.M.A. Maksoud
Prof. Dr. John Ward

University of Glamorgan
School of Technology
Wales, UK

Prof. Dr. G. Hausmann

Georg-Simon-Ohm Fachhochschule Nürnberg
Fachbereich Maschinenbau und
Versorgungstechnik

Abstract

The multiphase application of screw pumps, especially at high pressures and gas volume fractions implicates thermal loads for the solid components of the pump. For the evaluation of these loads and their consequences, a finite volume heat transfer model for the screws, as the main parts of a screw pump, was developed to describe and simulate the transient and 3-dimensional heat transfer process. The time-dependent heat transfer is mainly influenced by convection and thus by the rotational speed of the screws and by the temperature distribution of the multiphase fluid along the screw surface.

Key words :   screw pump - heat transfer -
              finite volume - convection -
              heat conduction

1. Introduction

The type of pump, whose main component will be theoretically investigated in this paper, is a twin screw pump, which can be used for multiphase operations. A screw pump is a particular type of rotary displacement pump, in which a number of screws rotate inside a cylindrical housing. The geometry and rotation of the screws generate a series of closed chambers, which transport the fluid from the low pressure inlet to the high pressure outlet, see figure 1.1.

Low pressure area

High pressure area

Direction of conveyance
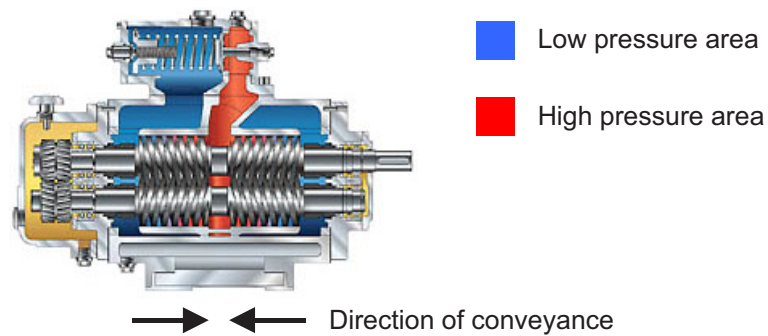
Figure 1.1 : Multiphase screw pump

Previous investigations of multiphase screw pumps have largely been concerned with the general pumping behaviour of these systems [1]. Moreover these studies have been restricted to medium sized pumps, in which the driving power and gas concentrations are relatively modest. In these situations the heat capacity and density of the gas-liquid mixture is dominated by the liquid phase so that the pumping process is essentially isothermal and thermodynamic effects can be neglected [2] and [3]. In the case of pumping multiphase mixtures with high gas volume fractions in combination with high pressure differences over a longer period, the remaining amount of liquid is not able to absorb the compression heat of the compressible gas phase. Also at medium mean gas volume fractions, it could be possible that the pump have to convey a mixture with a much higher gas content for a certain time, so that the above mentioned disregard cannot be justified for this extended range of multiphase application. The leakage flows through the different gaps at a gas volume fraction of 100 % were investigated numerically [4], to determine the compressibility and acceleration effects of the gas phase inside the gaps.

There are existing two new models [5] and [6], which include the thermodynamic effects by establishing mass and energy balance equations for the fluid flow through each chamber. Also the heat transfer effects inside the screw and the housing were investigated, [5]. But, no heat transfer model for the screws can be found in literature, which deals with the heat transfer including the tangential temperature gradient concerning the whole screw package including the shafts, see figure 1.2. There is a need for a model that can predict the resulting thermal expansion of the screw and the influence on the flow inside the perimeter and the radial gap by the changing of the gap-defining surfaces.
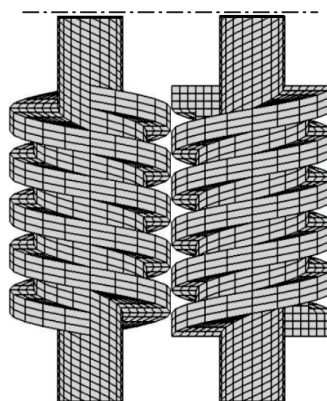
Figure 1.2 : A pair of meshing screws (taken apart)

Heat transfer model for the simulation of spindle heating and expansion inside a multiphase screw pump

Due to the lack of such a model and to prevent the ill effect of a conveyance break off due to a screw blockage inside the housing as a result of severe thermal effects, it is necessary to develop a new transient numerical heat transfer model for the whole screw.

2. Fundamentals of heat transfer

Heat conduction problems of several kinds are described by the following partial differential equation

$$\frac{\partial T}{\partial t} = a \cdot \left(\frac{\partial^2 T}{\partial x^2} + \frac{\partial^2 T}{\partial y^2} + \frac{\partial^2 T}{\partial z^2} \right) \pm \frac{\dot{q}}{\rho \cdot c_p} \qquad \text{(parabolic PDE)} \qquad (2.1)$$

For steady-state calculations without any heat sources and sinks the expression can be reduced to

$$\frac{\partial^2 T}{\partial x^2} + \frac{\partial^2 T}{\partial y^2} + \frac{\partial^2 T}{\partial z^2} = 0 \qquad \text{(elliptic PDE)} \qquad (2.2)$$

By introducing, besides the pure heat conduction and the consideration of heat sources and sinks, also the convection on the outer surface of a body, an energy balance equation can be introduced.

$$\frac{\partial Q_{cell}}{\partial t} = \sum_{n=1}^{6} \left(\pm \dot{q}_{conduction} \cdot A \right) + \sum_{n=1}^{6} \left(\pm \dot{q}_{convection} \cdot A \right) \pm \dot{Q}_{sink/source} \qquad (2.3)$$

$$\text{with} \qquad Q_{cell} = c_{cell} \cdot \rho_{cell} \cdot V_{cell} \cdot T_{cell} \qquad (2.4)$$

$$\dot{q}_{conduction} = -k \cdot \frac{\partial T}{\partial x_i} \qquad \text{(Fourier's law of heat conduction)} \qquad (2.5)$$

$$\dot{q}_{convection} = -h \cdot \left(T_\infty - T_{surface} \right) \qquad (2.6)$$

As a consequence of this, the temporal change of energy of a certain control volume is dependent on the heat fluxes in or out of this volume and possible heat sources and sinks inside this volume. Whereas the thermal conductivity is a property of the material, the convective heat transfer coefficient is a function of the flow and fluid condition around the surface of the body. In the case of the screw of a multiphase pump, it is assumed as a homogeneous equilibrium gas-liquid mixture, which is enclosed by the still-standing housing and three moving walls - two chamber flanks and one chamber ground. The calculation procedure, [7] [8] and [9], for determining the corresponding Nusselt number or the convective heat transfer coefficient, will be explained sequentially below.

Important non-dimensional parameters

$$\text{Reynolds number} \qquad Re = \frac{u_\varphi \cdot d_h \cdot \rho_H}{\mu_H} \qquad (2.7)$$

$$\text{Prandtl number} \qquad Pr = \frac{\mu_H \cdot c_{p,H}}{k_H} \qquad (2.8)$$

$$\text{Nusselt number} \qquad Nu = \frac{h \cdot d_h}{k_H} \qquad (2.9)$$

with $\quad d_h = \pi \cdot 2 \cdot r_{cell\,position}$ (2.10)   and $u_\varphi = \dfrac{2 \cdot \pi \cdot n}{60} \cdot r_{cell\,position}$ (2.11)

Mixture fluid properties (homogeneous equilibrium formulation)

mass fraction

$$x = \frac{\alpha \cdot \rho_G}{(1-\alpha) \cdot \rho_L + \alpha \cdot \rho_G}$$ (2.12)

homogeneous density

$$\rho_H = (1-\alpha) \cdot \rho_L + \alpha \cdot \rho_G$$ (2.13)

homogeneous dynamic viscosity

$$\mu_H = (1-\alpha) \cdot \mu_L + \alpha \cdot \mu_G$$ (2.14)

homogeneous thermal conductivity

$$k_H = (1-\alpha) \cdot k_L + \alpha \cdot k_G$$ (2.15)

homogeneous specific heat capacity

$$c_{p,H} = (1-x) \cdot c_L + x \cdot c_{p,G}$$ (2.16)

Nusselt numbers for a flat plate in parallel flow

for laminar flows $Re < 6 \cdot 10^4$ and $0.6 < Pr < 10$

$$Nu = 0.332 \cdot Re^{1/2} \cdot Pr^{1/3}$$ (2.17)

for turbulent flows $5 \cdot 10^5 < Re < 10^7$ and $0.6 < Pr < 60$

$$Nu = 0.0296 \cdot Re^{4/5} \cdot Pr^{1/3} \qquad (\text{Chilton \& Colburn})$$ (2.18)

3. Finite volume method

The governing partial differential equation for the transient temperature field without any heat sources and sinks follows to

$$\frac{\partial T}{\partial t} = \frac{k_S}{c_S \cdot \rho_S} \cdot \left[\frac{\partial}{\partial x}\left(\frac{\partial T}{\partial x}\right) + \frac{\partial}{\partial y}\left(\frac{\partial T}{\partial y}\right) + \frac{\partial}{\partial z}\left(\frac{\partial T}{\partial z}\right) \right]$$ (3.1)

The finite volume method is a very efficient calculation method in the field of numerical heat transfer and computational fluid dynamics and is characterised as having a high accuracy compared to finite element method (FEM) and by a higher flexibility compared to the finite difference method (FDM).

The finite volume approach, [10] [11] and [12], is to integrate the derivative terms in the heat conduction equation with respect to the three space coordinates over the whole finite volume and then transform the results with the divergence theorem by Gauss.

Integration of the heat transfer equation

$$c_S \cdot \rho_S \cdot \oiiint_V \left(\frac{\partial}{\partial t} I\right) dV + \oiiint_V \left(\frac{\partial}{\partial x} J\right) dV + \oiiint_V \left(\frac{\partial}{\partial y} K\right) dV + \oiiint_V \left(\frac{\partial}{\partial z} L\right) dV = 0$$ (3.2)

with the transient parameter $I = T$ (3.3)

and the heat flux densities

$$J = -k_S \cdot \frac{\partial T}{\partial x} \quad (3.4) \qquad K = -k_S \cdot \frac{\partial T}{\partial y} \quad (3.5) \qquad L = -k_S \cdot \frac{\partial T}{\partial z} \quad (3.6)$$

Notice : The equations 3.4 to 3.6 are only valid in the case of heat conduction, for example in the interior of the body. If the cell belongs to the surface of the screw, were convection can occur, other formulations for the heat flux densities must be used.

$$J, K, L = -h \cdot \left(T_{fluid} - T_{surface} \right) \tag{3.7}$$

Further details can be found below in the section of the applied boundary conditions.

Divergence theorem by Gauss

$$\oiiint_V divF \, dV = \oiint_A F \, d\boldsymbol{A} = \oiint_A (F \cdot \boldsymbol{n}) dA \tag{3.8}$$

$$\boldsymbol{A}_l = \boldsymbol{n}_l \cdot A_l \tag{3.9}$$

Resulting equation (formulation for each cell of the whole domain)

$$c_S \cdot \rho_S \cdot \frac{d}{dt} I_{i,j,k} \cdot V_{i,j,k} + \sum_{m=1}^{3} \sum_{l=1}^{6} \left(F_{m,l} \cdot A_{m,l} \right)_{i,j,k} = 0 \tag{3.10}$$

with   m = 1 ... 3   for each derivative in the three coordinate directions
           l = 1 ... 6   for each face of the cell, here with a cuboid's shape

The resulting equation 3.10 is already formulated for 3-dimensional finite volume cells, which will be generated by a structured discretisation of the whole solid domain. As an example, a single cell with all notations can be seen below in figure 3.1.
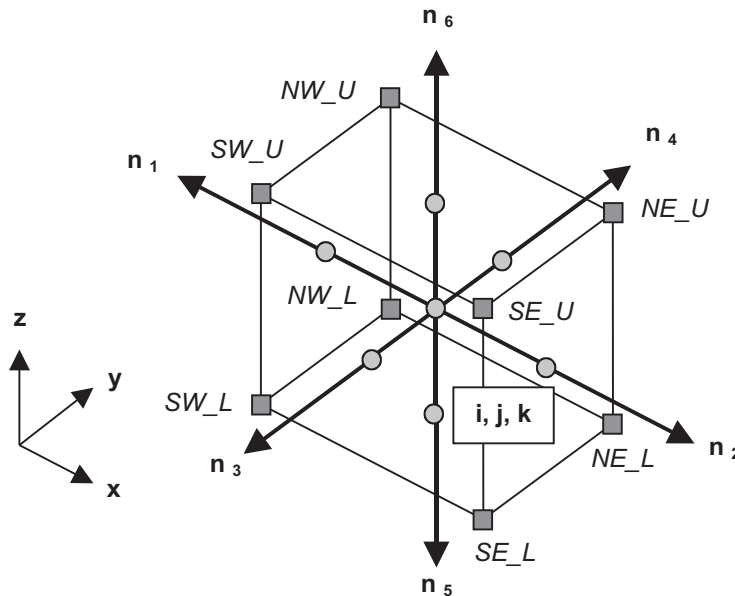
Figure 3.1 : 3-dimensional finite volume cell

The following form of equation 3.10 allows their direct use for the numerical calculation.

$$\frac{d}{dt} I_{i,j,k} = -\frac{1}{c_S \cdot \rho_S \cdot V_{i,j,k}} \cdot \begin{bmatrix} (J_1 \cdot A_{11}) + (J_2 \cdot A_{12}) + (J_3 \cdot A_{13}) + \\ (J_4 \cdot A_{14}) + (J_5 \cdot A_{15}) + (J_6 \cdot A_{16}) + \\ (K_1 \cdot A_{21}) + (K_2 \cdot A_{22}) + (K_3 \cdot A_{23}) + \\ (K_4 \cdot A_{24}) + (K_5 \cdot A_{25}) + (K_6 \cdot A_{26}) + \\ (L_1 \cdot A_{31}) + (L_2 \cdot A_{32}) + (L_3 \cdot A_{33}) + \\ (L_4 \cdot A_{34}) + (L_5 \cdot A_{35}) + (L_6 \cdot A_{36}) \end{bmatrix} \qquad (3.11)$$

In the above expression 3.11, the parameter I is defined by the heat condition in the centre of the cell (cell-centred formulation). The parameters J, K and L are calculated against it in the middle of the six cell faces A_1 to A_6 by averaged state values of two neighbouring cells in the case of heat conduction or will be replaced by definite heat flux densities.

4. Time-stepping method

The time stepping method, which was chosen for this transient finite volume heat transfer model is a fourth-order Runge-Kutta scheme, [12], (fourth-order accuracy in time).

$$I_{i,j,k}^{(0)} = I_{i,j,k}^{(n)} \qquad (4.1)$$

$$I_{i,j,k}^{(1)} = I_{i,j,k}^{(0)} - \alpha_1 \cdot \frac{\Delta t}{c_S \cdot \rho_S \cdot V_{i,j,k}} \cdot R^{(0)} \qquad (4.2)$$

$$I_{i,j,k}^{(2)} = I_{i,j,k}^{(0)} - \alpha_2 \cdot \frac{\Delta t}{c_S \cdot \rho_S \cdot V_{i,j,k}} \cdot R^{(1)} \qquad (4.3)$$

$$I_{i,j,k}^{(3)} = I_{i,j,k}^{(0)} - \alpha_3 \cdot \frac{\Delta t}{c_S \cdot \rho_S \cdot V_{i,j,k}} \cdot R^{(2)} \qquad (4.4)$$

$$I_{i,j,k}^{(4)} = I_{i,j,k}^{(0)} - \alpha_4 \cdot \frac{\Delta t}{c_S \cdot \rho_S \cdot V_{i,j,k}} \cdot \left(\frac{R^{(0)} + 2 \cdot R^{(1)} + 2 \cdot R^{(2)} + R^{(3)}}{6} \right) \qquad (4.5)$$

$$I_{i,j,k}^{(n+1)} = I_{i,j,k}^{(4)} \qquad (4.6)$$

with $\alpha_1 = 1/2$, $\alpha_2 = 1/2$, $\alpha_3 = 1$ and $\alpha_4 = 1$

The time-step duration Δt must be chosen very carefully. Large time-steps are preferable, but in the case of an explicit solution scheme, excessive large time-steps will result in numerical instabilities. The smaller the finite volume cells, the smaller the time-steps have to be, because of the decreasing time, which an information signal needs to pass through a smaller single cell.

5. Definition of the screw geometry as a solid domain

The screw, which will be investigated in this paper, has two threads, which means that there are existing twice as much chambers per a definite length comparing to a screw with only one thread. As a consequence of this, two opening chambers can be observed per screw rotation. The main parameter values of the geometry, which can be seen below in figure 5.1, are listed in table 5.1.

Description	Symbol	Value	Unit
Outer screw diameter	d_{outer}	0.100	m
Shaft diameter	d_{shaft}	0.040	m
Number of threads	N	2	---
Number of chambers	noc	5 [*)]	---
Thread pitch	h_{screw}	0.050	m
Depth of the perimeter gap	b_{PG}	0.0125	m
Width of the chambers	b_{cha}	0.0125	m
Depth of the chambers	t_{cha}	0.015	m

Table 5.1 : Main geometry parameter of the screw

[*)] 1 chamber with connection to the inlet / 3 closed chambers / 1 chamber with connection to the outlet
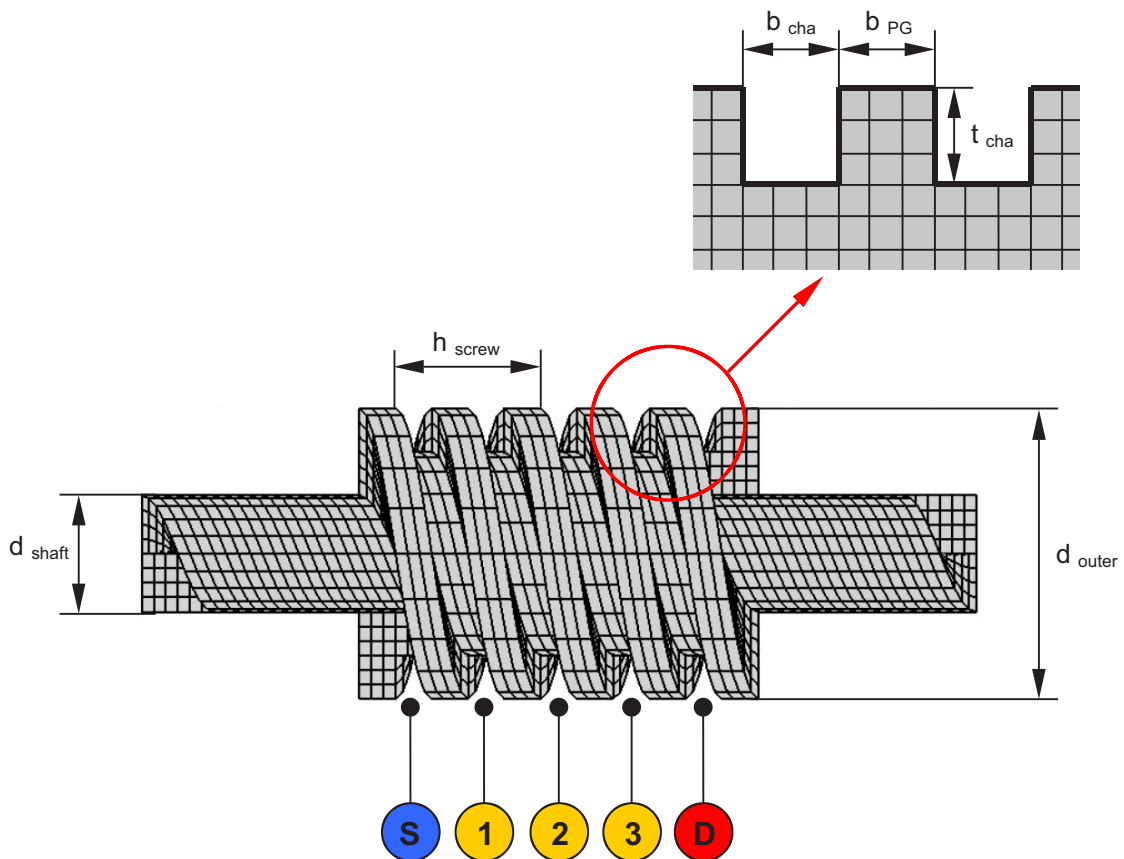
Figure 5.1 : Single screw with geometry definitions

6. Boundary conditions

To define all heat fluxes through the six cell faces everywhere inside the domain, the node temperatures of all surrounding neighbour cells have to be known. For the cells, which are describing the surface of the screw, either the temperature gradient normal to the surface or a heat flux has to be defined. This is done by the application of boundary conditions around the screw surface.

As an example, figure 6.1 shows the right end surface in the positive x-direction, two real or body cells, which are lying inside the screw and one virtual or dummy cell for the application of the boundary conditions.
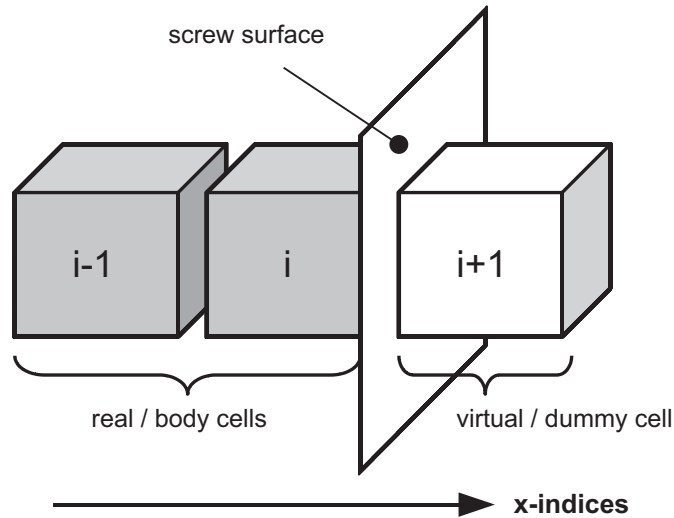
Figure 6.1 : Screw surface with adjacent cells

For the rotating screw, two kinds of thermal boundary conditions have to be distinguished. This is firstly the adiabatic wall and secondly the surface with forced convection. The correct extrapolation of the interior node temperatures to the virtual cells is explained in the figure 6.2.
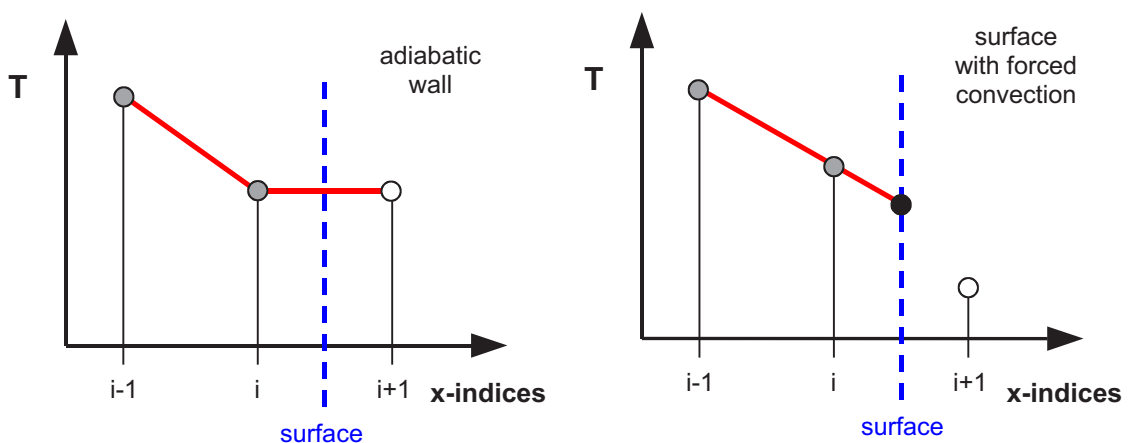
Figure 6.2 : Two kinds of thermal boundary conditions

Equation for the corresponding heat flux density of the adiabatic wall:

$$T_{i+1} = T_i \tag{6.1}$$

$$\dot{q}_{conduction} = -k \cdot \frac{\partial T}{\partial x} \tag{6.2}$$

$$\dot{q}_{conduction} = -k \cdot \frac{T_{i+1} - T_i}{x_{i+1} - x_i} = 0 \tag{6.3}$$

Equation for the corresponding heat flux density of the surface with forced convection:

$$T_{i+1} = T_\infty = T_{fluid} \tag{6.4}$$

$$T_{surface} = T_i + \frac{T_i - T_{i-1}}{x_i - x_{i-1}} \cdot \tfrac{1}{2} \cdot (x_{i+1} - x_i) \tag{6.5}$$

$$\dot{q}_{convection} = -h \cdot (T_{i+1} - T_{surface}) \tag{6.6}$$

The faces of all cells were forced convection is assumed are illustrated in figure 6.3, whereas the different colours stand for the three coordinate directions.
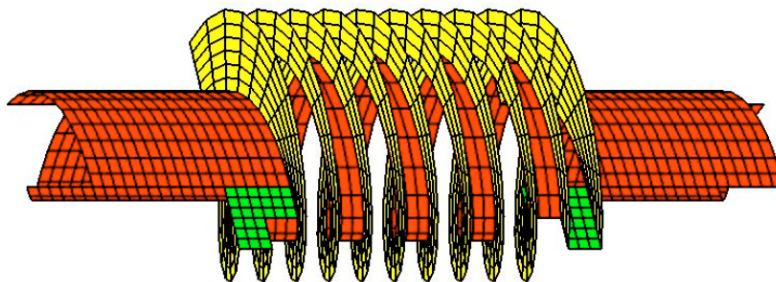
Figure 6.3 : Convective heat transfer surfaces

The most important task during the application of the different boundary condition is the correct determination of the convective heat transfer coefficients as a function of the positions of the corresponding cell faces relative to the axis of rotation. These heat transfer coefficients can be calculated by the procedure, which was explained in section 2, if the fluid conditions and properties, see table 6.1 and 6.2 around the screw are known. The results for a rotational speed of the screws of 3000 rpm are presented in table 6.3.

Position	---	S	1	2	3	4	5	D	---
Temperature	T	300	300	325	350	375	400	400	K
Pressure	p	1.0	1.0	11.0	21.0	31.0	41.0	41.0	bar
GVF	α	0.98	0.98	0.97	0.96	0.95	0.94	0.94	---

Table 6.1 : Fluid condition in the inlet, the chambers and the outlet (showcase values)

	Description	Symbol	Value	Unit
Liquid	Density	ρ_L	1000	kg / m^3
	Dynamic viscosity	μ_L	$1000 \cdot 10^{-6}$	Pa s
	Thermal conductivity	k_L	$600 \cdot 10^{-3}$	W / (m K)
	Specific heat capacity	c_L	4200	J / (kg K)
Gas	Dynamic viscosity	μ_G	$20 \cdot 10^{-6}$	Pa s
	Thermal conductivity	k_G	$25 \cdot 10^{-3}$	W / (m K)
	Isobar specific heat capacity	c_{pG}	1004	J / (kg K)
	Individual gas constant	R	287	J / (kg K)
Solid	Density	ρ_S	7850	kg / m^3
	Thermal conductivity	k_S	55	W / (m K)
	Specific heat capacity	c_S	465	J / (kg K)
	Thermal expansion coefficient	α	$12 \cdot 10^{-6}$	1 / K

Table 6.2 : Properties of the liquid / gaseous phase and the solid body

Convective heat transfer coefficients							
Position	---	1	2	3	4	5	---
Chamber flanks - min	$h_{CF\,min}$	643.2	1027.2	1357.1	1656.9	1937.0	W / (m^2 K)
Chamber flanks - max	$h_{CF\,max}$	741.1	1183.6	1563.6	1909.1	2231.8	W / (m^2 K)
Chamber grounds	h_{CG}	617.1	985.7	1302.1	1589.8	1858.5	W / (m^2 K)
Shaft surface - inlet	$h_{shaft\,in}$	441.4					W / (m^2 K)
Shaft surface - outlet	$h_{shaft\,out}$	1329.3					W / (m^2 K)

Table 6.3 : Convective heat transfer coefficients inside the chambers and on the shafts

7. Thermal expansions and their influence on the gap shapes

As a consequence of the convective heat fluxes from the surrounding fluid into the solid domain, the screw will expand accordingly to the temperature distribution inside. The perimeter gaps between the screws and the housing and the radial and flank gaps between the counter-rotating screws are rather small with a mean gap height from approximately 50 to 200 micrometers. Depending on the outer radius of the screws, a temperature increase of 100 K will already result in an unacceptable thermal expansion with an impending solid body contact between the screws or between the screws and the housing, which is assumed as stiff in this case.

The thermal expansion will be formulated here as a 2-dimensional problem in the radial and the peripheral direction, to evaluate the influence of the changing screw shape on the most important perimeter and radial gaps. In the case of the flank gap, mainly the expansions of the screw flights in the screw length direction have to be determined. The successive calculation of the 2-dimensional thermal expansion of each cell from the axis of rotation back to the screw surface follows for the lower North-West node as an example to:

For the first cell close to the axis of rotation

$$NW_{new\,i,j,k} = \begin{bmatrix} NW_{1,i,j,k} + \alpha \cdot \left(NW_{1,i,j,k} - NE_{1,i,j,k} \right) \cdot \left(T_{i,j,k} - T_{IC} \right) \\ NW_{2,i,j,k} + \alpha \cdot \left(NW_{2,i,j,k} - NE_{2,i,j,k} \right) \cdot \left(T_{i,j,k} - T_{IC} \right) \\ NW_{3,i,j,k} \end{bmatrix} \tag{7.1}$$

For each following cell

$$NW_{new\,i,j,k} = \begin{bmatrix} NW_{new\,1,i+1,j,k} + \left(NW_{1,i,j,k} - NE_{1,i,j,k} \right) + \alpha \cdot \left(NW_{1,i,j,k} - NE_{1,i,j,k} \right) \cdot \left(T_{i,j,k} - T_{IC} \right) \\ NW_{new\,2,i+1,j,k} + \left(NW_{2,i,j,k} - NE_{2,i,j,k} \right) + \alpha \cdot \left(NW_{2,i,j,k} - NE_{2,i,j,k} \right) \cdot \left(T_{i,j,k} - T_{IC} \right) \\ NW_{3,i,j,k} \end{bmatrix} \tag{7.2}$$

After determining the thermal expansions, the gap height reductions or respectively the new shapes of the several gaps can be calculated. Due to the fact, that the main proportion of the leakage flows through the perimeter and the radial gap, these both types of clearances are explained in more detail.

The perimeter gap at norm conditions equals due to the large ratio between outer screw radius and the gap height to a 2-dimensional rectangular channel, whereas the radial gap can be treated as a convergent-divergent nozzle with two different radii at the lower and the upper side, corresponding to the outer radius of the screw flight and the radius of the chamber ground. The thermal expansions of the screw and so the gap height reductions increase towards the pump discharge. From a qualitative point of view, the thermal expansions inside these two kind of gaps are presented by figure 7.1.
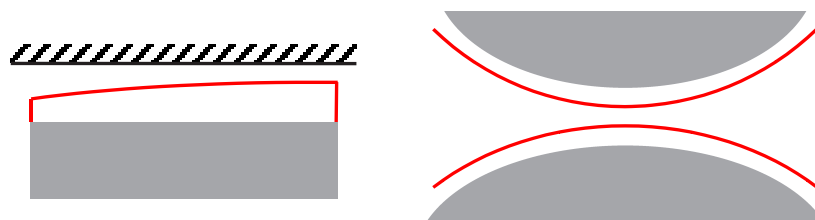
Figure 7.1 : Shape of the perimeter (left) and the radial gap (right), before (grey) and after (red) thermal expansion

Concerning the radial gap, there are two expansions in two different planes - firstly in the cross section, which can be seen in figure 7.1 and secondly perpendicular to the latter section in the screw length direction, like in the case of the perimeter gap. After the determination of the new gap shape, every gap has to be treated with a varying boundary wall to calculate the leakage flow more accurately by an additional leakage flow model.

8. Simulation results

The test case for this heat transfer model was the heat build-up of the screw with the boundary conditions explained above in section 6 and the overall initial temperature of 300 K. The simulation was accomplished with time-step duration of 0.03 seconds and was stopped after 6000 iterations or 180 seconds. The computational grid was defined by 10 cells in radial (x) direction, 20 cells in peripheral (y) direction and 69 cells in screw length (z) direction, whereas the parameter control point for example for the time history plot has the coordinates (6 / 11 / 36) in the x-y-z cell-index notation.

The time history and the residual of the temperature can be seen in figure 8.1. The simulation shows a good convergence behaviour, because of the continuous decreasing residual. In the ideal case it becomes zero, whereas the temperature time history will result in a steady state condition.

The figures 8.2 and 8.3 present two sets of temperature contour plots, which are equal to 8 cuts from the center of the screw to the outer radius over the whole screw length with an increasing peripheral angle from 9° to 171° and from 189° to 351°. The chambers with the numbers 1 to 4 (figure 8.2) and 2 to 5 (figure 8.3) can be seen as small rectangular pockets with constant temperature values at the left side of a single contour plot. The inlet and outlet region with the corresponding temperature are defined by the lower and upper large rectangular fields, which are lying also at the left side in these plots.

The next set of temperature contour plots, see figure 8.4, shows the temperature distributions in the z-y and in the y-x plane, which contain both the parameter control point. The first plot is the winding off in the peripheral direction with the constant x-value of the parameter control point. The second contour plot, represents the temperature inside the middle chamber No. 3 (see also table 6.1) and the solid material below this chamber from the chamber ground to the screw axis.

Figure 8.5 shows the temperature distribution in the cross section, which include the axis of rotation in the middle of the plot. The right subplot combines the actual temperature plot with the screw shape after the thermal expansion, but for a better visualisation with a 200-times magnified value of expansion. The colour of contours has no specified correlation with fixed temperatures, but they define a step-wise transition from the maximum possible temperature (red colour faces) to the minimum possible temperature (blue coloured faces) in the whole solid domain, which are mostly equal to the discharge and suction fluid temperature in the steady state case for example.

The figure 8.6 is similar to the previous plot, but presents the 3-dimensional screw and the temperature distribution on the screw surface. Looking at a single subplot, it can be seen, that there are existing in each case 4 chambers left and right from the screw axis. The lowest chamber of the left side is still connected with the inlet, whereas the highest chamber of the right side is already connected with the outlet. The remaining 3 chambers on each side represent the closed chambers, whereas a chamber part for example of the right side belongs to the next but one on the left side and so on. The reasons for this are on the one side the 2 screw threads and on the other side the fact, that the counter-rotating screw meshes into the visible screw from the side of observation and disconnect the apparently continuous chambers.

For a more convenient comparison between the initial screw shape and the expanded screw, figure 8.7 shows both situations in two single subplots. This was shown firstly in the cross section and secondly in the view of the 3-dimensional screw surface.

Finally it has to be said, that due to the rotation of the screw, the presented temperature distribution is just a snapshot of an exclusive screw position. To include the rotational effect, the boundary conditions or the thermodynamic and fluid dynamic chamber values have to be applied around the whole screw in peripheral direction as a function of time with the rotational speed as the main parameter.
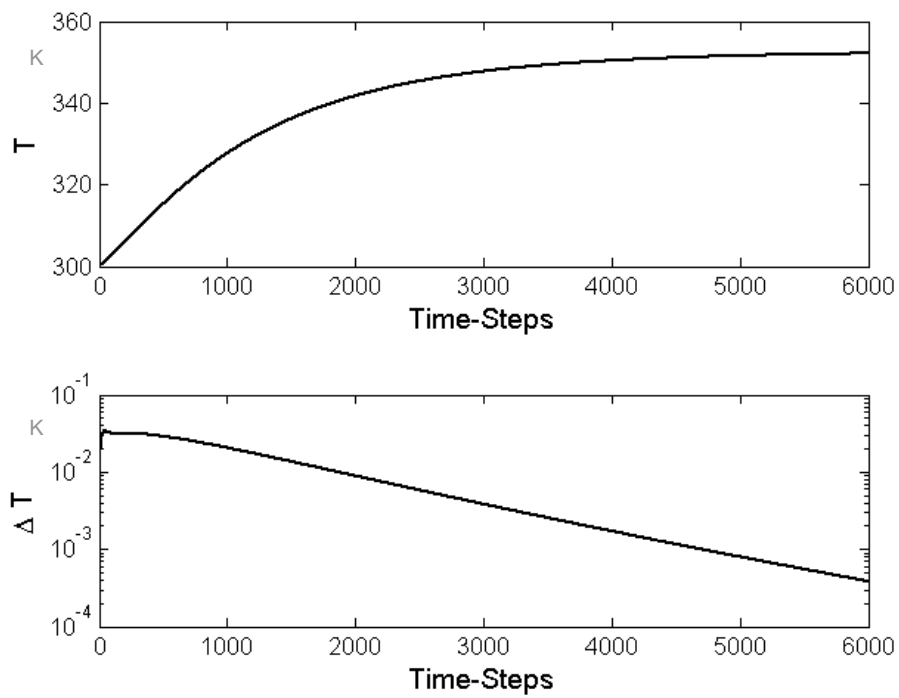
Figure 8.1 : Temperature time history and the residual as a function of time-steps
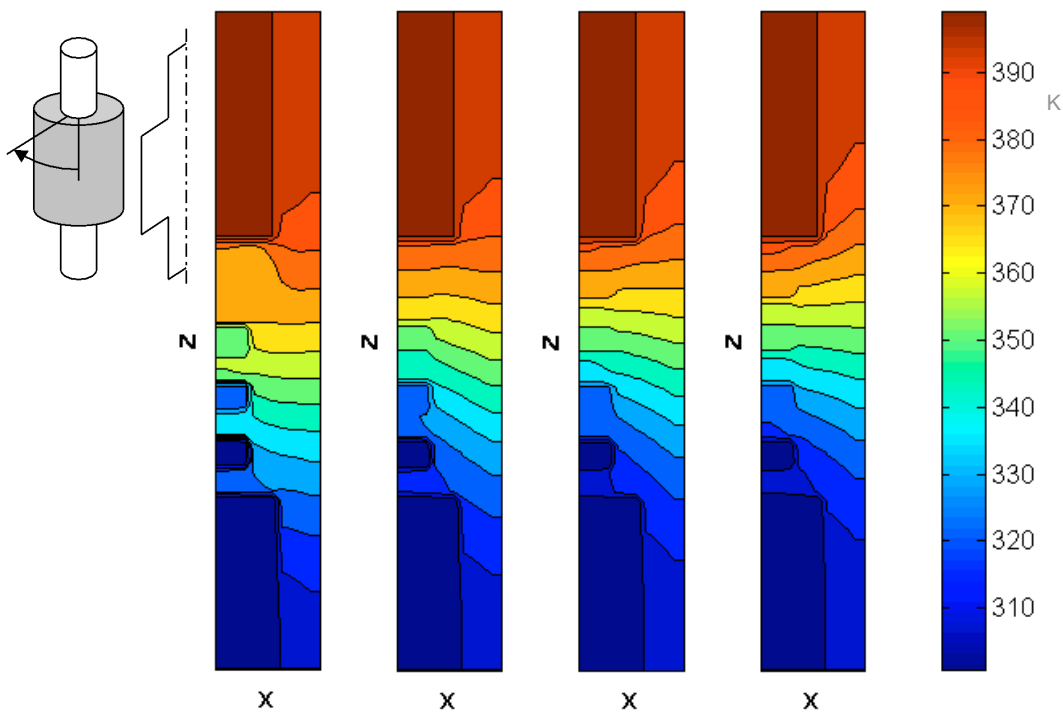
Figure 8.2 : Set of temperature contour plots (from 9° to 171° , x : radial direction , z : screw length direction)
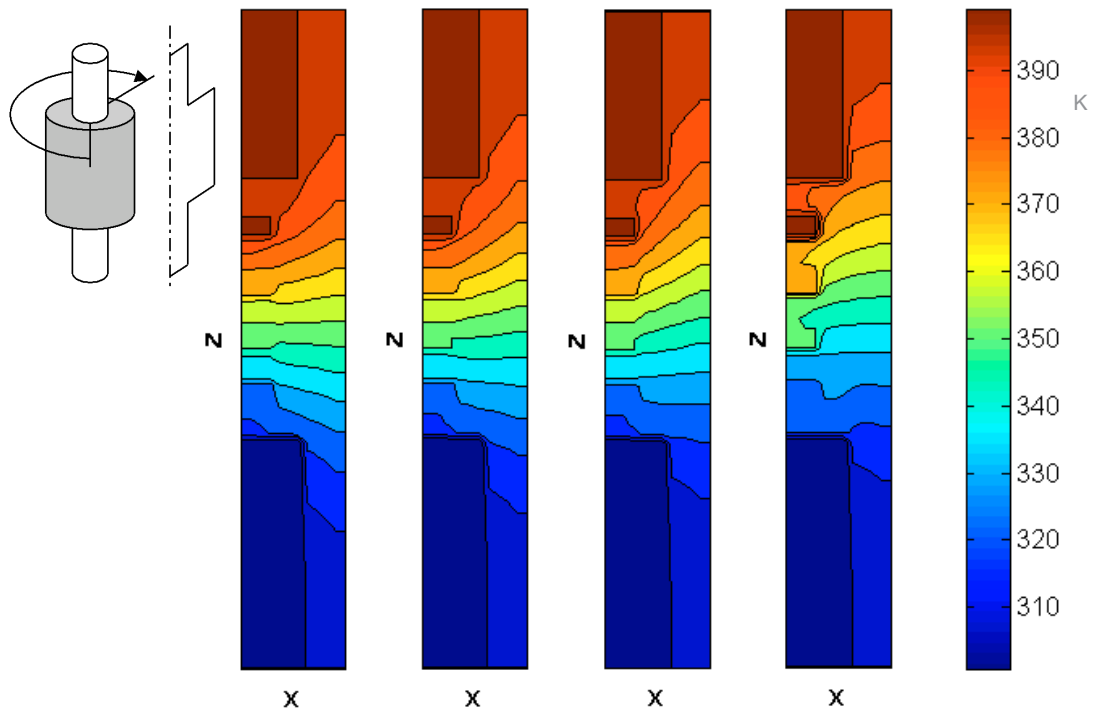
Figure 8.3 : Set of temperature contour plots (from 189° to 351° , x : radial direction , z : screw length direction)
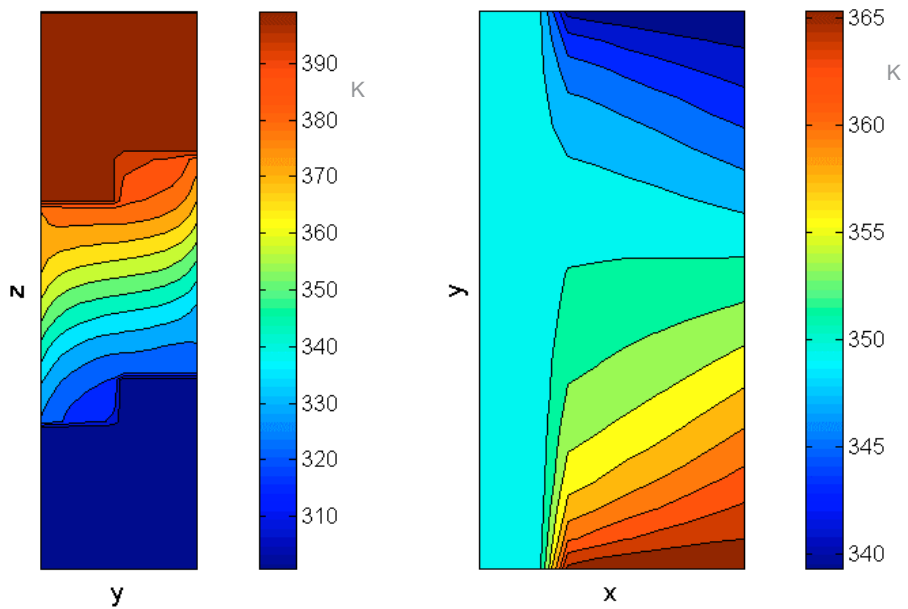
Figure 8.4 : Set of temperature contour plots (x : radial direction , y : peripheral direction , z : screw length direction)

Heat transfer model for the simulation of spindle heating and expansion inside a multiphase screw pump
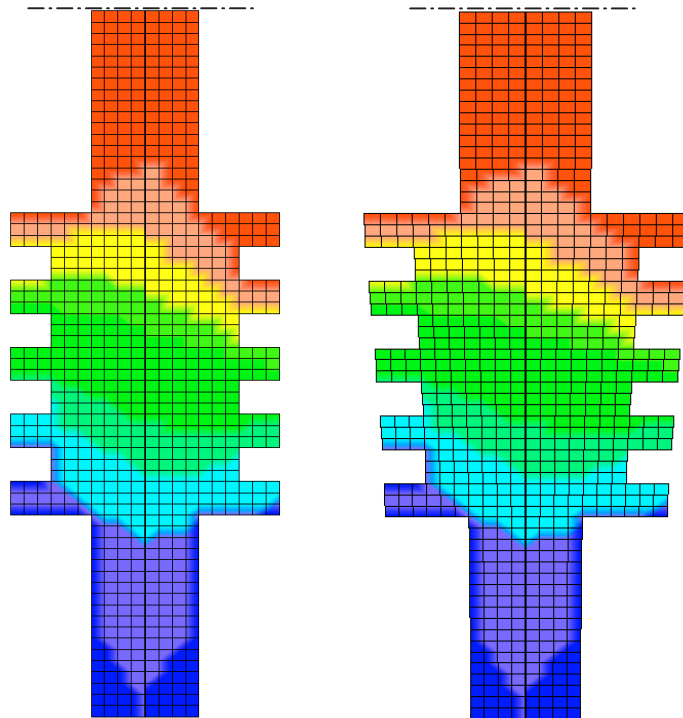
Figure 8.5 : Temperature distribution inside the screw (without and with thermal expansion)
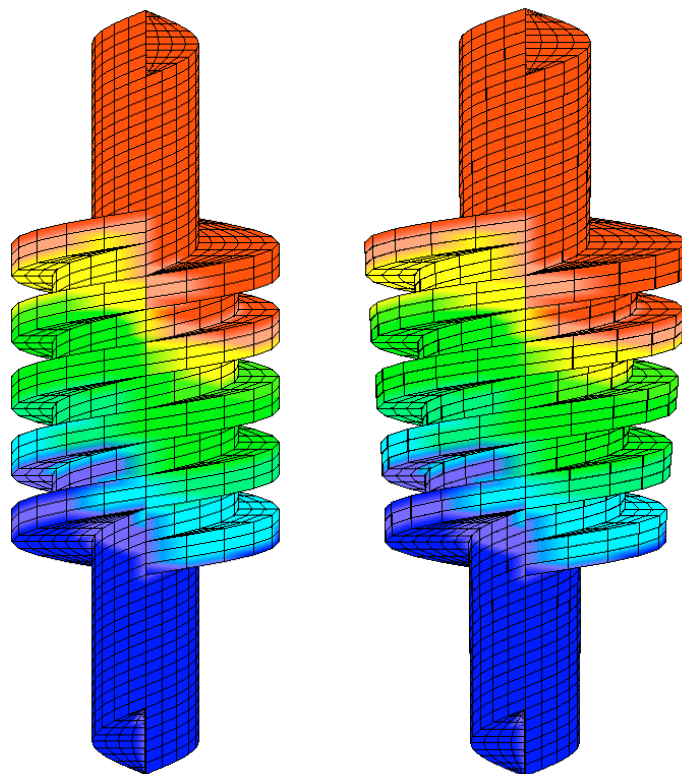
Figure 8.6 : Temperature distribution on the screw surface (without and with thermal expansion)
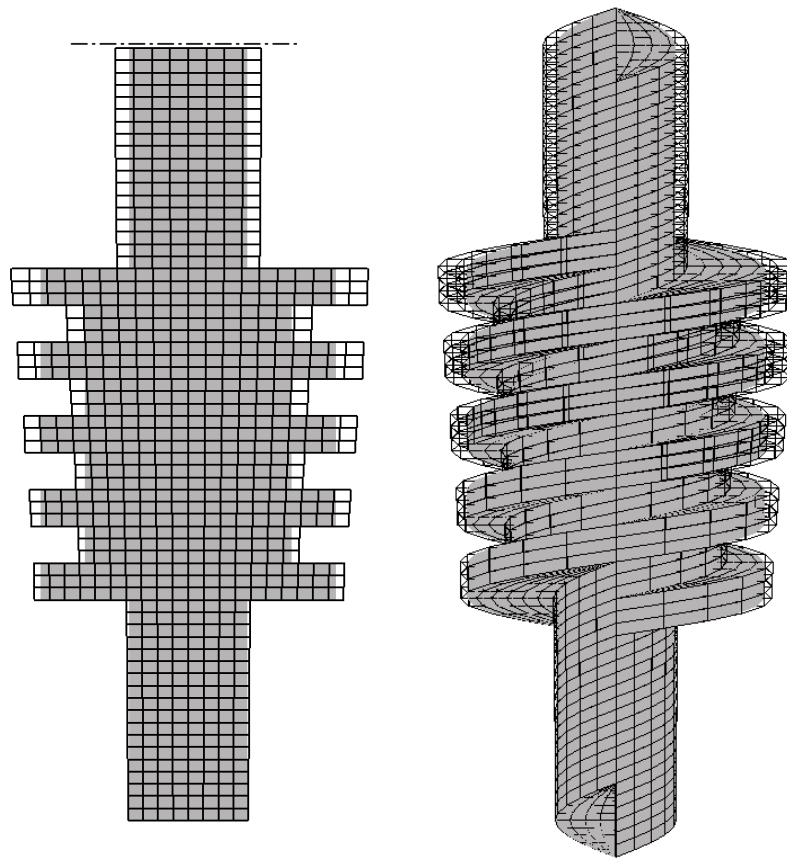
Figure 8.7 : Screw shape shifting as a result of thermal expansions

9. Conclusion

The finite volume heat transfer model, which was described in this paper, is capable of calculating the 3-dimensional heat conduction inside the screw and the convection inside the chambers and on the shaft surfaces at the suction and the discharge side of the pump. Due to the time-dependency of the calculation method, it is possible to simulate the thermal steady state and the corresponding solid expansion with the current fluid and flow condition around the screw and to determine the maximum acceptable time-span of pumping, at a point of operation, where a long-time run is not possible as a result of critical high temperature values in the chambers and the outlet. The model also gives information about the variation of the gap heights as a function of the gap length direction, which can be used in a leakage flow model to predict the mass flow more accurately. But for this step, the discretisation of the flight has to be refined, to avoid sharp discontinuities in the gap height derivative. Furthermore, the position of the first contact between the screw and the housing, which is assumed as stiff compared to the screw, and the region of a increased amount of wear can be also determined. As such the heat transfer model used in this investigation can be beneficial in the development and operation diagnostics of multiphase screw pumps.

Acknowledgements

Nomenclature

General symbols

a	thermal diffusivity
A	area (general)
b	depth, width
c	specific heat capacity
d	diameter
D	discharge
E, N, S, W	cardinal points : east, north, south and west (node)
h	convection heat transfer coefficient; thread pitch
I	transient term, which is differentiated with respect to t
J, K, L	heat flux densities, which are differentiated with respect to x, y and z
k	thermal conductivity
L	length
m	mass
n	rotational speed
N	number of threads
p	static pressure
q	specific heat energy
Q	heat energy
r	radius
R	gas constant; term of variable changes in the Runge-Kutta scheme
S	suction
t	time; depth
T	temperature (general)
u	velocity
V	volume (general)
x	mass fraction
x, y, z	coordinates

Vectors / Matrices

A	normal vector * cell face area
n	normal vector

Greek Letters

α	gas volume fraction; Runge-Kutta factor; thermal expansion coefficient
Δ	difference
μ	dynamic viscosity
ρ	density
φ	peripheral angle
ω	angular velocity

Subscripts

CF	chamber flank
CG	chamber ground
cha	chamber
G	gaseous
h	hydraulic
H	homogeneous
i, j, k	cell indicators
in	inlet
l	cell face area index
IC	initial condition
L	liquid; lower
m,n	coordinate direction index
out	outlet
p	constant pressure
PG	perimeter gap
S	solid
U	upper
∞	condition in the infinity

Superscripts

n	current time step
n+1	following time step

Abbreviations

GVF	gas volume fraction
noc	number of cells
Nu	Nusselt number
PDE	partial differential equation
Pr	Prandtl number
Re	Reynolds number
rpm	revolutions per minute

References

[1]   WINCEK, M.:
        Zur Berechnung des Förderverhaltens von Schraubenspindelpumpen bei der Förderung von
        Flüssigkeits / Gas-Gemischen, Dissertation,
        Universität Erlangen-Nürnberg, 1992
        (*The calculation of the conveyance behaviour of screw pumps at the conveyance of liquid/gas-
        mixtures, Ph.D. thesis, University of Erlangen-Nuremberg, 1992*)

[2]   KÖRNER, H.:
        Zum Förderverhalten von Schraubenspindelpumpen für Zweiphasengemische
        hohen Gasgehalts, Dissertation,
        Universität Erlangen-Nürnberg, 1998
        (*The conveyance behaviour of screw pumps for two-phase mixtures with high
        gas-volume-fractions, Ph.D. thesis, University of Erlangen-Nuremberg, 1998*)

[3]   ETZOLD, S.:
        Verlustanalyse von Schraubenspindelpumpen bei Mehrphasenförderung,
        Dissertation, Universität Hannover, 1993
        (*Leakage analysis of screw pumps during multiphase conveyance,
        Ph.D. thesis, University of Hanover, 1993*)

[4]   RÄBIGER, K. / MAKSOUD, T.M.A. / WARD, J. / HAUSMANN, G.:
        Development of a finite volume model for the compressible gap flow inside a screw pump, Series of
        the University of Applied Sciences Nuremberg, No. 30, 2005

[5]   NAKASHIMA, C.Y. / OLIVEIRA, S. / CAETANO, E.F.:
        Thermo-hydraulic model of a twin-screw multiphase pump, ASME IMECE 04, Anaheim, USA, 2004

[6]   RAUSCH, T. / VAUTH, T. / BRANDT, J.U. / MEWES, D.:
        A model for the delivering characteristic of multiphase pumps, 4th North American Conference on
        Multiphase Technology, Banff, Canada, 2004

[7]   BAEHR, H. D. / STEPHAN, K.:
        Wärme- und Stoffübertragung (*Heat and mass transfer*), Springer-Verlag,
        Berlin / Heidelberg, 1998

[8]   WAGNER, W.:
        Wärmeübertragung (*Heat transfer*),
        Vogel Verlag, Würzburg, 1998

[9]   INCROPERA, F.P. / DEWITT, D.P.:
        Fundamentals of Heat and Mass Transfer - 4th Edition,
        John Wiley & Sons, Inc., 1996

[10]   POLIFKE, W. / KOPITZ, J.:
        Wärmeübertragung - Grundlagen, analytische und numerische Methoden (*Heat transfer -
        Fundamentals, analytical and numerical methods*), Pearson Studium, München, 2005

[11]   OERTEL JR., H. / LAURIEN, E.:
        Numerische Strömungsmechanik (*Numerical fluid mechanics*), Springer-Verlag,
        Berlin / Heidelberg, 1995

[12]   WENDT, J.F.:
        Computational Fluid Dynamics, Springer-Verlag,
        Berlin / Heidelberg, 1996